

3895
775511
2123409

A DIRECTIONAL BOREHOLE RADAR SYSTEM
FOR
SUBSURFACE IMAGING

TR 3895





A DIRECTIONAL BOREHOLE RADAR SYSTEM FOR SUBSURFACE IMAGING

Proefschrift

ter verkrijging van de graad van doctor
aan de Technische Universiteit Delft,
op gezag van de Rector Magnificus prof.dr.ir. J.T. Fokkema,
voorzitter van het College van Promoties,
in het openbaar te verdedigen op woensdag 26 juni 2002 om 10:30 uur
door

Koen Willem Anton van DONGEN

doctorandus in de natuurkunde
geboren te Iloilo, Filippijnen.



Dit proefschrift is goedgekeurd door de promotoren:

Prof.dr.ir. P.M. van den Berg

Prof.dr.ir. J.T. Fokkema

Samenstelling promotiecommissie:

Rector Magnificus	voorzitter
Prof.dr.ir. P.M. van den Berg	Technische Universiteit Delft, promotor
Prof.dr.ir. J.T. Fokkema	Technische Universiteit Delft, promotor
Prof.dr. S.M. Luthi	Technische Universiteit Delft
Prof.dr.ir. C.P.A. Wapenaar	Technische Universiteit Delft
Prof.ir. P. van Genderen	Technische Universiteit Delft
Prof.dr.ir. A.P.M. Zwamborn	Technische Universiteit Eindhoven
Drs. R. van Ingen	T&A Survey, Amsterdam

Published and distributed by DUP Science

DUP Science is an imprint of

Delft University Press

PO Box 98

2600 MG Delft

The Netherlands

Telephone: + 31 15 2785678

Telefax: + 31 15 2785706

E-mail: info@Library.TUdelft.NL

keywords: ground penetrating radar, borehole, inversion

ISBN 90-407-2310-9

Copyright ©2002 by K.W.A. van Dongen

All rights reserved. No part of the material protected by this copyright notice may be reproduced or utilized in any form or by any means, electronic or mechanical, including photocopying, recording, or by any information storage and retrieval system, without written permission from the publisher: Delft University Press.

Printed in the Netherlands.

Financial support and patent

The research reported in this thesis is financed by T&A Survey, Amsterdam, the Netherlands, and Bedrijfs Technologische Samenwerking (BTS) of the Ministry of Economic Affairs. Some parts of this publication are patented by T&A Survey, Amsterdam, the Netherlands.

Preface

The work presented in this thesis is a continuation of research and remarkable incidents over the past centuries. One of the first incidents was in 900 BC, where Magnus, a Greek shepherd, walked across a field of black stones which pulled the iron nails out of his sandals and the iron tip from his shepherd's staff (authenticity not guaranteed). This region becomes known as Magnesia. Many centuries later, serious research took place and it was Charles Francois du Fay who discovered in 1733 that electricity comes in two kinds which he called resinous (-) and vitreous (+). Almost a century later, in 1820, Hans Christian Oersted discovered that electric current in a wire causes a compass needle to orient itself perpendicular to the wire. Faraday started to repeat these experiments in 1821, and many new experiments followed. This resulted in the introduction of field lines to describe the phenomena and in 1837 he discovered the idea of the dielectric constant. James Clerk Maxwell wrote in 1855 a memoir in which he combines Faraday's ideas of field lines with Thomson's mathematical analogies. In addition, Maxwell showed that light was an electromagnetic phenomenon and that the speed of light and the speed of electromagnetic waves electromagnetic waves are equal. His most well known publication is his Treatise on Electricity and Magnetism, published in 1873. This paper discusses everything which was known at that moment about electromagnetism, from the viewpoint of Faraday. Hertz was the first who demonstrated wireless electromagnetic systems in 1886. In addition, he showed that electromagnetic waves are reflected by metallic and dielectric objects. In 1903 the first "radar" system was developed by Hüllsmayer, who experimented with the detection of radiowaves reflected on ships. His work resulted in 1904 in the patent "*Hertzian-wave Projecting and Receiving Apparatus Adapted to Indicate or Give Warning of the Presence of a Metallic Body, Such as a Ship or a Train, in the Line of Projection of Such Waves*". Hülsenbeck started to determine the structure of buried objects with pulsed electromagnetic signals for which he obtained a patent in 1926.

Some people, like Olhoeft in 1996, mention Stern as the first person who used radar to map the subsurface. In 1929, Stern performed surveys with ground penetrating radar in Austria to probe the depth of a glacier. During the second world war, radar techniques evolved rapidly, and in the eighties ground penetrating radar was utilized increasingly for the detection of natural cavities, road pavement analysis, forensic science, etc.. In this period the first radar surveys out of a borehole were carried out for prospecting, as mentioned by Dyck in 1975, and for testing the integrity of rocks at nuclear waste disposal sites. Many borehole systems followed. However, none of these system made it possible to obtain three-dimensional images of the subsurface out of a borehole. The present thesis deals with the theoretical design of a borehole radar that enables us three-dimensional imaging of the surrounding environment ¹.

¹Obviously, this is just a selection out of the remarkable highlights on electromagnetic theory and ground penetrating radar in the past centuries. Many more are mentioned in the books from Whittaker published in 1960, or in the overviews given in 1985 by Dyck and Young, and in 2001 by Salazar-Palma et al. and Sarkar et al..

Contents

1	Introduction and survey	1
2	Basic electromagnetic equations	5
2.1	Electromagnetic wavefield	6
2.2	Boundary Conditions	8
2.3	Reciprocity relations	9
3	Design of directional borehole radar	15
3.1	Antenna configuration	16
3.2	Formulation of integral equation	18
3.3	Discretization of integral equation	20
3.4	Conjugate gradient solution scheme	25
3.5	Numerical results for parabolically curved cylindrical reflector	28
3.6	Numerical results for circularly curved cylindrical reflector	32
3.7	Experimental verification	37
3.8	Conclusion	38
4	Imaging	41
4.1	Change in impedance due to scattering objects	41
4.2	Measuring in bistatic mode	47
4.3	Discretization of the spatial domain	50
4.4	The effective sensitivity function	53
4.5	Exploring the effective sensitivity function	55

4.6	A single step inversion via back-propagation	61
4.7	Synthetic and experimental results back-propagation method . .	62
4.8	Conjugate gradient inversion method	70
4.9	Synthetic and experimental results conjugate gradient method . .	72
4.10	Maximum angular resolution	77
4.11	Conclusion	80
5	Conclusions	83
A	Orthogonal curvilinear coordinate system	87
A.1	Cylindrical coordinate system	89
A.2	Parabolical coordinate system	91
	Bibliography	93
	Samenvatting	97
	Curriculum Vitae	101

Chapter 1

Introduction and survey

This thesis concerns the development of a directional borehole radar system. We first discuss a modeling method for the design of the antenna. Subsequently, we develop algorithms to obtain three-dimensional images of the subsurface.

In the twenties Hülßenbeck started to determine the structure of buried objects with pulsed electromagnetic signals. Other people, like Stern in 1929, started to use radar for mapping the subsurface, and performed surveys with ground penetrating radar (GPR) in Austria to probe the depth of a glacier. This was the beginning of a long trajectory where radar was used to probe the subsurface from the surface. The technique is based on the reflection of waves at the intersection between two media with different electromagnetic properties, like an object in the subsurface or two layers. In the past decades, other electromagnetic techniques have been developed as well. For instance induction techniques, where electromagnetic waves in the low frequency range are used to detect layers and objects which are highly conductive. However, problems arise if the electromagnetic waves can not reach the domain of interest, because it is either simply too deep (oil industry) or behind an electrically impenetrable layer. This can be for instance a highly conductive claylayer, or a concrete floor with metal objects. The solution to this problem is choosing a location that is closer to the domain of interest. In practise it means that we have to drill a borehole and perform the measurements out of it. This resulted in the development of new methods in the seventies and eighties, of which an overview is given, among others, by Dyck and Young in 1985. During the last decades improvements have been made concerning penetration depth and resolution, resulting in two classes of systems. One class has a large penetrating

depth, but is not directional. Consequently, it is not known where the received reflected signal comes from and therefore, it is not possible to obtain a three-dimensional image of the subsurface. The other class of systems is directional, but has hardly any penetrating power. These systems are mainly used for measuring the orientation of layers in the subsurface. Note that an overview of resistivity logging tools is recently given by B.I. Anderson (2001). It is obvious that there is a great demand for a system which has both a directional radiation pattern and a large penetration depth. In order to meet this demand we started in 1998 with the development of a borehole radar system which has a directional radiation pattern, a large penetration depth, and sensitive receiving properties. With such a tool, a three-dimensional image of the subsurface can be obtained.

To discuss the design of the system, we start at the basis of electromagnetic theory using Maxwell's equations. In chapter 2 we express them in a differential form in the time domain. Since the aim of this project is the design of an antenna system which operates optimally for one specific frequency, we introduce the Laplace transformation. With this transformation, we describe phenomena in the frequency domain instead of the time domain. We apply this transformation on Maxwell's equations. The electromagnetic waves, we are dealing with, are generated by an electric dipole antenna, i.e. an electric-current-carrying wire. A directional radiation pattern is obtained through the presence of a metallic reflector next to the dipole. Hence, we need additional expressions to describe the influence of the reflector on the wavefield. Those are given by the electromagnetic boundary conditions. Finally, we introduce a theorem, the reciprocity theorem, to describe the complete system, containing a dipole antenna, a perfectly conducting reflector for the focussing effect, and a scattering object. The basis for this reciprocity theorem has been made by Lord Rayleigh in 1894. The resulting equation serves as a starting point for the design of the reflector and the development of a scheme to compute an image of the subsurface. In this equation an integral over unknown quantities occur, hence we refer to it as an integral equation.

In chapter 3 we discuss the design of the bistatic antenna system of the directional borehole radar. We show that a directional radiation pattern is obtained by positioning a perfectly conducting reflector next to an electric dipole. Therefore, we start with the integral equation derived in chapter 2, but in the absence of scattering objects. Since the reflector is curved in the direction perpendicular to the dipole, we formulate the problem in a curvilinear coordinate system. We end up with an integral equation which combines the known incident electric wavefield from the dipole antenna with the unknown electric-surface-current density at the reflector. This integral equation is solved with a conjugate gradient method. This method is independently developed by Stiefel (1951) and Hestenes (1951,1973). In 1952 they published together an article, which is generally acknowledged to be the first report of the mod-

ern conjugate gradient method. Many books and articles have been written on this subject. The present implementation is based on the work done by Kleinman and Van den Berg (1991), and Van den Berg (2002). To increase the computational speed, we use a fast Fourier transform for the computation of the convolution present in one direction. We show various numerical results for several configurations, as obtained in our search for the optimal configuration. Based on the design presented in this chapter, a prototype antenna system is built. Measuring the radiation pattern of this prototype enables us to verify our numerical results.

After the development of this new directional borehole antenna system, we concentrate on the development of an imaging algorithm which uses the radiation characteristics of the antenna in an optimal manner. This is discussed in chapter 4. Again we start with reciprocity, where we formulate two distinctive states in which the system can operate. Hence, we have in each state a domain containing the same antenna configuration. Since this domain is inaccessible, the antenna system is described by the state as observed at the end ports of the system. To describe this state, we use an impedance formulation. The absence or presence of scattering objects in the remaining spatial domain determines in which state the complete system is. Differences in states are notified by changes in impedance. We combine these formulations with the results from chapter 3. Consequently, we end up with an integral equation. After "simplifying" (linearizing) the integral equation, we obtain an equation which contains a known sensitivity function representing the transmitting and receiving properties of the antenna system, a known (measured) impedance function and an unknown function describing the changes of the medium parameters. Since the sensitivity function plays such an essential role, we explore this function. We show that the function can be approximated by an effective one, resulting in a reduction of computational time and the need of computer memory. Three imaging algorithms are derived, enabling us to obtain a three-dimensional image of the subsurface. Two are based on a one-step inversion scheme minimizing an error functional, and are called standard and minimized back-propagation. The other one is a conjugate gradient method that attempts to improve the image iteratively. The algorithms are tested on both synthetic and measured data. The chapter ends with a short discussion on the maximum angular resolution achievable.

In the concluding chapter (5) we briefly discuss the essential steps in the development of the directional borehole system. We outline some aspects which need more attention and further research, hopefully, resulting in an improvement of the current system. In addition we make some remarks on possible applications of the system. Some of them are easy to realize, others are challenging.

Chapter 2

Basic electromagnetic equations

The directional borehole radar system we discuss throughout this thesis contains an electric dipole and a perfectly conducting curved reflector. In figure 2.1 the antenna system is shown schematically. Here we consider the dipole as a electric-current-carrying thin wire, creating an electric wavefield. This wavefield reflects at the surface of the perfectly conducting reflector. The reflected wavefield together with the “dipole” wavefield, forms the incident wavefield from the antenna system into the subsurface. It is obvious that the curvature and the position of the reflector have a great influence on the directionality of the radiation pattern of the antenna system.

In this chapter we start with stating the Maxwell equations as a set of differential equations and their constitutive relations, since they form the basis in describing the electromagnetic phenomena. However, at the surface of our reflector the Maxwell equations are no longer continuously differentiable. Therefore, additional conditions are required, valid at the surface of the reflector. These differential equations, constitutive relations, and boundary conditions are used in the reciprocity theorem. This theorem interrelates in a specific manner two admissible states that could occur in one and the same time-invariant spatial domain. We use this reciprocity theorem to describe the interaction between the dipole, the reflector, and a scattering object. One state is taken as the probing state while the other one is taken as the physical or actual state. This results in an integral equation, which is used as starting point in the remaining chapters.

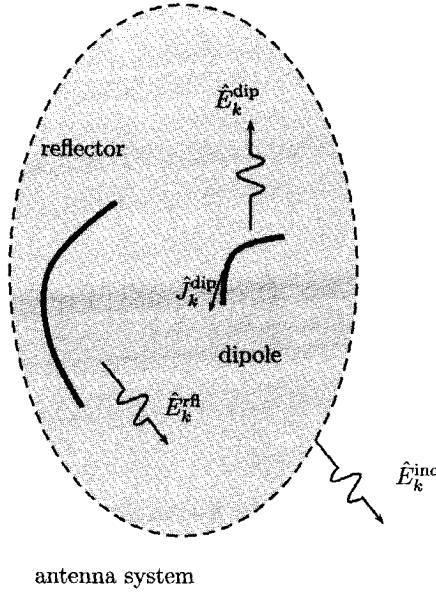


Figure 2.1: The antenna system, where a perfectly conducting curved reflector is positioned next to an electric-current-carrying thin wire.

2.1 Electromagnetic wavefield

The Maxwell equations, based on the equations formulated by Maxwell in 1873, form the basis for describing electromagnetic phenomena. Let the vector $\vec{x} = x_i$ for $i = \{1, 2, 3\}$ denotes the spatial position in \mathbb{R}^3 in the Cartesian coordinate system and let t denotes the temporal parameter, then Maxwell's equations in differential form in matter read

$$-\epsilon_{k,m,p} \partial_m H_p(\vec{x}, t) + J_k(\vec{x}, t) + \partial_t D_k(\vec{x}, t) = -J_k^{\text{ext}}(\vec{x}, t), \quad (2.1)$$

$$\epsilon_{j,n,r} \partial_n E_r(\vec{x}, t) + \partial_t B_j(\vec{x}, t) = -K_j^{\text{ext}}(\vec{x}, t), \quad (2.2)$$

where $\epsilon_{k,m,p}$ is the Levi-Civita tensor of rank three, ∂_t the temporal derivative, and ∂_m and ∂_n the spatial derivatives in the x_m - and x_n -directions. The meanings of the electromagnetic field quantities are given in table 2.1. We use the Einstein convention such that summation takes place over quantities with repeated lower-case subscripts. Since there are more unknowns than known parameters, we have an incomplete set of equations, even if the right-hand sides are known, which express the actions of external forces. Supplementing

Table 2.1: The electromagnetic field quantities

$E_k(\vec{x}, t)$	electric wavefield	[V/m]
$H_j(\vec{x}, t)$	magnetic wavefield	[A/m]
$D_k(\vec{x}, t)$	electric displacement wavefield	[C/m ²]
$B_j(\vec{x}, t)$	magnetic induction wavefield	[T]
$J_k(\vec{x}, t)$	volume density of electric current	[A/m ²]
$J_k^{\text{ext}}(\vec{x}, t)$	volume density of electric-source (external) current	[A/m ²]
$K_j^{\text{ext}}(\vec{x}, t)$	volume density of magnetic-source (external) current	[V/m ²]

Table 2.2: The electromagnetic medium parameters

$\sigma(\vec{x})$	electric conductivity	[S/m]
ε_0	(absolute) electric permittivity of vacuum	[F/m]
$\varepsilon_r(\vec{x})$	relative electric permittivity	[-]
μ_0	(absolute) magnetic permeability of vacuum	[H/m]
$\mu_r(\vec{x})$	relative magnetic permeability	[-]

equations are furnished by the constitutive relations, which read

$$J_k(\vec{x}, t) = \sigma(\vec{x})E_k(\vec{x}, t) , \quad (2.3)$$

$$D_k(\vec{x}, t) = \varepsilon_0 \varepsilon_r(\vec{x})E_k(\vec{x}, t) , \quad (2.4)$$

$$B_j(\vec{x}, t) = \mu_0 H_j(\vec{x}, t) , \quad (2.5)$$

where the meanings of the medium parameters are given in table 2.2. Throughout this thesis we only work with nonmagnetic susceptible materials, consequently, we take the relative permeability μ_r equal to one. In addition, we assume the medium to be linear, time invariant, locally and instantaneously reacting and isotropic in its electromagnetic behavior. Combining equations (2.1)-(2.5) results in a set of differential equations with two unknowns for known medium parameters and external sources, viz.

$$-\varepsilon_{k,m,p} \partial_m H_p(\vec{x}, t) + \sigma(\vec{x})E_k(\vec{x}, t) + \varepsilon_0 \varepsilon_r(\vec{x}) \partial_t E_k(\vec{x}, t) = -J_k^{\text{ext}}(\vec{x}, t) , \quad (2.6)$$

$$\varepsilon_{j,n,r} \partial_n E_r(\vec{x}, t) + \mu_0 \partial_t H_j(\vec{x}, t) = -K_j^{\text{ext}}(\vec{x}, t) . \quad (2.7)$$

This set of differential equations is transformed to the frequency domain, using the temporal Fourier transform. Switching on the sources at instant $t = t_0$, the temporal domain \mathcal{T} is defined as

$$\mathcal{T} = \{t \in \mathbb{R} | t > t_0\} . \quad (2.8)$$

The complement of the temporal domain $\{t_0 \cup \mathcal{T}\}$ is denoted as \mathcal{T}' and hence

$$\mathcal{T}' = \{t \in \mathbb{R} | t < t_0\} . \quad (2.9)$$

The one-sided Laplace transform of a function $f(\vec{x}, t)$ in space-time, defined for $t \in \{t_0 \cup \mathcal{T}\}$, is defined as

$$\hat{f}(\vec{x}, s) = \int_{t=t_0}^{\infty} \exp(-st) f(\vec{x}, t) dt , \quad (2.10)$$

where s is the Laplace transform parameter. In physics all quantities have bounded values, so s must satisfy

$$\text{Re}\{s\} > 0 . \quad (2.11)$$

Now the temporal Fourier transform with time factor $\exp(-i\omega t)$ is obtained by taking the limit

$$s \rightarrow -i\omega , \quad (2.12)$$

where ω is the real and positive temporal angular frequency, and where $i^2 = -1$. Note that we use the symbol $\hat{}$ to indicate that a quantity or a parameter is defined in the temporal Laplace domain. Applying the temporal Fourier transformation on equations (2.6) and (2.7), we obtain

$$-\epsilon_{k,m,p} \partial_m \hat{H}_p(\vec{x}, s) + s \hat{\epsilon}(\vec{x}, s) \hat{E}_k(\vec{x}, s) = -\hat{J}_k^{\text{ext}}(\vec{x}, s) , \quad (2.13)$$

$$\epsilon_{j,n,r} \partial_n \hat{E}_r(\vec{x}, s) + s \mu_0 \hat{H}_j(\vec{x}, s) = -\hat{K}_j^{\text{ext}}(\vec{x}, s) , \quad (2.14)$$

where $\hat{\epsilon}(\vec{x}, s)$ denotes the complex permittivity of the medium, viz.

$$\hat{\epsilon}(\vec{x}, s) = \epsilon_0 \epsilon_r(\vec{x}) + \frac{\sigma(\vec{x})}{s} , \quad (2.15)$$

which describes the electromagnetic properties of the medium.

2.2 Boundary Conditions

Let there be two adjacent volume domains \mathbb{M}_1 and \mathbb{M}_2 with different electromagnetic media properties $\hat{\epsilon}_1(\vec{x}, s)$ and $\hat{\epsilon}_2(\vec{x}, s)$, and separated by a source-free surface \mathbb{S} as shown in figure 2.2. Let ν_i denote the vector normal to the surface \mathbb{S} , pointing into the domain \mathbb{M}_2 . At this surface, the electromagnetic boundary conditions require that the tangential components of the magnetic, $\hat{H}_p(\vec{x}, s)$, and the electric, $\hat{E}_r(\vec{x}, s)$, wavefield are continuous across this surface, hence

$$\epsilon_{k,m,p} \nu_m \hat{H}_p(\vec{x}, s) \quad \text{is continuous across } \mathbb{S} , \quad (2.16)$$

$$\epsilon_{j,n,r} \nu_n \hat{E}_r(\vec{x}, s) \quad \text{is continuous across } \mathbb{S} . \quad (2.17)$$

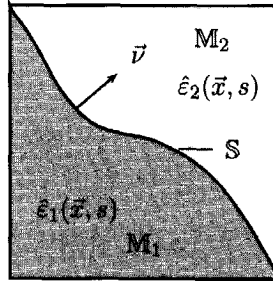


Figure 2.2: Two spatial domains M_1 and M_2 with media properties $\hat{\epsilon}_1(\vec{x}, s)$ and $\hat{\epsilon}_2(\vec{x}, s)$, separated by the source-free surface S with normal \vec{n} .

Whereas the components of the magnetic induction wavefield, $\hat{B}_j(\vec{x}, s)$, and the electric displacement wavefield, $\hat{D}_k(\vec{x}, s)$, normal to the surface are continuous across S , thus

$$\nu_j \hat{B}_j(\vec{x}, s) \quad \text{is continuous across } S, \quad (2.18)$$

$$\nu_k \hat{D}_k(\vec{x}, s) \quad \text{is continuous across } S. \quad (2.19)$$

However, in case the domain M_1 is electrically impenetrable, the tangential components of the electric wavefield must vanish at the surface S and satisfy the relation

$$\lim_{h \rightarrow 0} \epsilon_{j,n,r} \nu_n \hat{E}_r(\vec{x} + h\vec{n}) = 0, \quad \forall \vec{x} \in S. \quad (2.20)$$

This is in general true for the case where the relative permittivity $\epsilon_r(\vec{x})$ or the conductivity σ goes to infinity. In the special case when an infinitely thin reflector is present at S , the tangential components of the magnetic wavefield, exhibit a discontinuity across the surface equal to an electric-surface-current density present at the surface of the reflector, viz.

$$\hat{J}_k^{\text{rf}}(\vec{x}, s) = \lim_{h \rightarrow 0} \epsilon_{k,m,p} \nu_m \left[\hat{H}_p(\vec{x} + h\vec{n}, s) - \hat{H}_p(\vec{x} - h\vec{n}, s) \right], \quad \forall \vec{x} \in S, \quad (2.21)$$

where $\hat{J}_k^{\text{rf}}(\vec{x}, s)$ is the tangential electric-surface-current density in $[\frac{\text{A}}{\text{m}}]$.

2.3 Reciprocity relations

Reciprocity is used to interrelate the electromagnetic wavefield quantities from two different states A and B , that could occur in one and the same space-time domain. Each of the two states is characterized by its own set of source distributions and medium parameters. State A represents the computational or probing state. In this state an electric-probing-source current $\hat{J}_k^{\text{prb}}(s)\delta(\vec{x} - \vec{x}^{\text{prb}})$ is

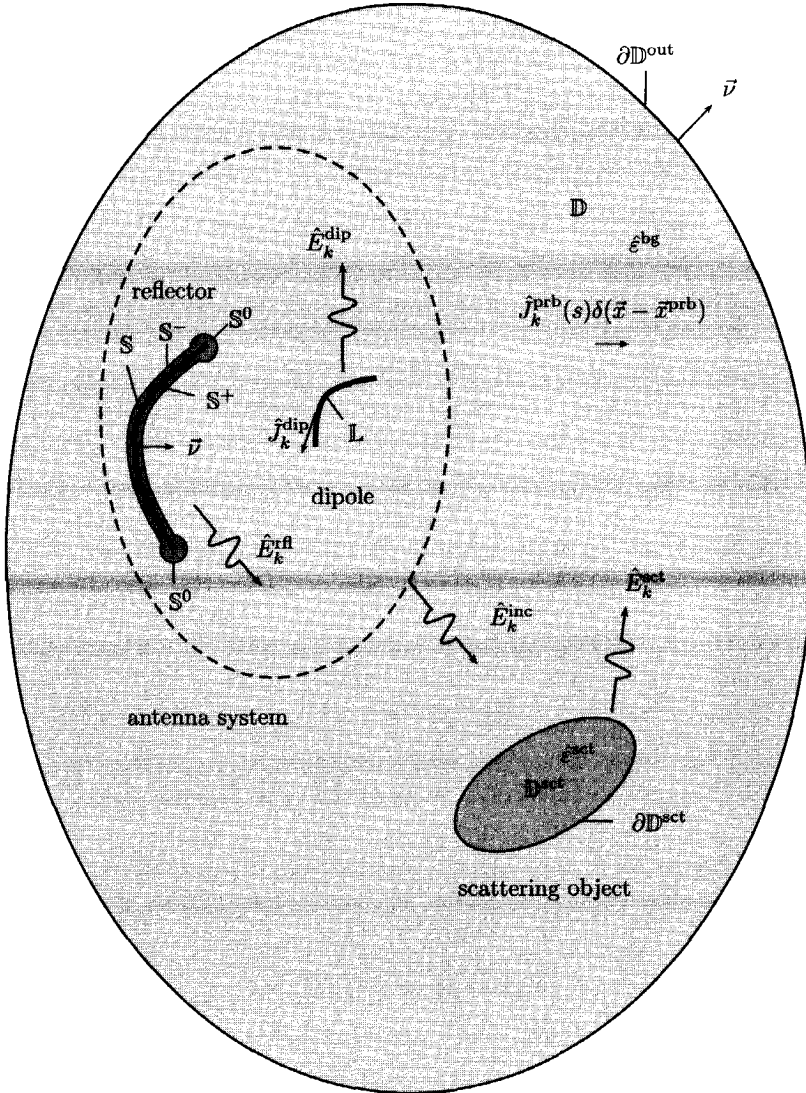


Figure 2.3: The two states of the spatial domain \mathbb{D} . State A describes the probing state where an electric-point-source current \hat{j}_k^{prb} is present. State B represents the actual state containing a thin wire in the domain L carrying an electric current, a metal reflector in the inaccessible volume domain enclosed by the surfaces S^+ , S^- and S^0 , and an accessible scattering object with complex permittivity $\hat{\epsilon}^{\text{sct}}$ in the domain \mathbb{D}^{sct} .

Table 2.3: Description of the two states of the spatial domain \mathbb{D}

state A		state B	
$\hat{E}_k^A = \hat{E}_k^{\text{prb}}(\vec{x}, s)$	$\forall \vec{x} \in \mathbb{D}$	$\hat{E}_k^B = \hat{E}_k^{\text{tot}}(\vec{x}, s)$	$\forall \vec{x} \in \mathbb{D}$
$\hat{H}_j^A = \hat{H}_j^{\text{prb}}(\vec{x}, s)$	$\forall \vec{x} \in \mathbb{D}$	$\hat{H}_j^B = \hat{H}_j^{\text{tot}}(\vec{x}, s)$	$\forall \vec{x} \in \mathbb{D}$
$\hat{j}_k^{\text{ext};A} = \hat{j}_k^{\text{prb}}(s)\delta(\vec{x} - \vec{x}^{\text{prb}})$	$\forall \vec{x} \in \mathbb{D}$	$\hat{j}_k^{\text{ext};B} = \hat{j}_k^{\text{dip}}(\vec{x}, s)$	$\forall \vec{x} \in \mathbb{L}$
$\hat{K}_j^{\text{ext};A} = 0$	$\forall \vec{x} \in \mathbb{D}$	$\hat{K}_j^{\text{ext};B} = 0$	$\forall \vec{x} \in \mathbb{D}$
$\hat{\varepsilon}^A = \hat{\varepsilon}^{\text{bg}}(s)$	$\forall \vec{x} \in \mathbb{D}$	$\hat{\varepsilon}^B = \begin{cases} \hat{\varepsilon}^{\text{bg}}(s) & \forall \vec{x} \in \mathbb{D}' \\ \hat{\varepsilon}^{\text{sct}}(\vec{x}, s) & \forall \vec{x} \in \mathbb{D}^{\text{sct}} \end{cases}$	
$\hat{\mu}^A = \mu_0$	$\forall \vec{x} \in \mathbb{D}$	$\hat{\mu}^B = \mu_0$	$\forall \vec{x} \in \mathbb{D}$
$\mathbb{S} = \emptyset$			
$\mathbb{D}^{\text{sct}} = \emptyset$		$\mathbb{D}' = \mathbb{D} \setminus \{\mathbb{S} \cup \mathbb{D}^{\text{sct}}\}$	

present in a homogeneous background medium with medium parameter $\hat{\varepsilon}^{\text{bg}}(s)$. Therefore, the field quantities are denoted as $\{\hat{E}_k^{\text{prb}}(\vec{x}, s), \hat{H}_j^{\text{prb}}(\vec{x}, s)\}$. State B however, represents the actual or physical state. Here we position an antenna system and an inhomogeneous scattering object with medium parameter $\hat{\varepsilon}^{\text{sct}}(\vec{x}, s)$ in the same background medium as in state A . The antenna system contains a thin electric-current-carrying wire as electric-current source and a perfectly conducting metal reflector. In this state the field quantities are denoted as $\{\hat{E}_k^{\text{tot}}(\vec{x}, s), \hat{H}_j^{\text{tot}}(\vec{x}, s)\}$.

A domain \mathbb{D} with boundary $\partial\mathbb{D}$ encloses a volume, which does not contain external magnetic currents and where the medium has a permeability μ_0 . For such a domain, the frequency-domain reciprocity theorem of the convolution type reads,

$$\begin{aligned}
\epsilon_{m,k,j} \int_{\vec{x} \in \partial\mathbb{D}} \nu_m \left(\hat{E}_k^A(\vec{x}, s) \hat{H}_j^B(\vec{x}, s) - \hat{E}_k^B(\vec{x}, s) \hat{H}_j^A(\vec{x}, s) \right) dA(\vec{x}) \\
= - \int_{\vec{x} \in \mathbb{D}} s \left(\hat{\varepsilon}^B(\vec{x}, s) - \hat{\varepsilon}^A(\vec{x}, s) \right) \hat{E}_k^A(\vec{x}, s) \hat{E}_k^B(\vec{x}, s) dV(\vec{x}) \\
+ \int_{\vec{x} \in \mathbb{D}} \left(\hat{j}_k^{\text{ext};A}(\vec{x}, s) \hat{E}_k^B(\vec{x}, s) - \hat{j}_k^{\text{ext};B}(\vec{x}, s) \hat{E}_k^A(\vec{x}, s) \right) dV(\vec{x}), \quad (2.22)
\end{aligned}$$

see for instance De Hoop (1995). Using this reciprocity relation, in combination with the two state descriptions from table 2.3 and as visualized in figure 2.3,

we obtain

$$\begin{aligned}
0 = & \epsilon_{m,k,j} \int_{\vec{x} \in \partial \mathbb{D}^{\text{out}}} \nu_m \left(\hat{E}_k^{\text{prb}}(\vec{x}, s) \hat{H}_j^{\text{tot}}(\vec{x}, s) - \hat{E}_k^{\text{tot}}(\vec{x}, s) \hat{H}_j^{\text{prb}}(\vec{x}, s) \right) dA(\vec{x}) \\
& - \epsilon_{m,k,j} \int_{\vec{x} \in \mathbb{S}^+} \nu_m \left(\hat{E}_k^{\text{prb}}(\vec{x}, s) \hat{H}_j^{\text{tot}}(\vec{x}, s) - \hat{E}_k^{\text{tot}}(\vec{x}, s) \hat{H}_j^{\text{prb}}(\vec{x}, s) \right) dA(\vec{x}) \\
& - \epsilon_{m,k,j} \int_{\vec{x} \in \mathbb{S}^-} \nu_m \left(\hat{E}_k^{\text{prb}}(\vec{x}, s) \hat{H}_j^{\text{tot}}(\vec{x}, s) - \hat{E}_k^{\text{tot}}(\vec{x}, s) \hat{H}_j^{\text{prb}}(\vec{x}, s) \right) dA(\vec{x}) \\
& - \epsilon_{m,k,j} \int_{\vec{x} \in \mathbb{S}^0} \nu_m \left(\hat{E}_k^{\text{prb}}(\vec{x}, s) \hat{H}_j^{\text{tot}}(\vec{x}, s) - \hat{E}_k^{\text{tot}}(\vec{x}, s) \hat{H}_j^{\text{prb}}(\vec{x}, s) \right) dA(\vec{x}) \\
& - \int_{\vec{x} \in \mathbb{D}^{\text{sct}}} s \left(\hat{\epsilon}^{\text{sct}}(\vec{x}, s) - \hat{\epsilon}^{\text{bg}}(s) \right) \hat{E}_k^{\text{prb}}(\vec{x}, s) \hat{E}_k^{\text{tot}}(\vec{x}, s) dV(\vec{x}) \\
& + \int_{\vec{x} \in \mathbb{D}} \hat{J}_k^{\text{prb}}(s) \delta(\vec{x} - \vec{x}^{\text{prb}}) \hat{E}_k^{\text{tot}}(\vec{x}, s) dV(\vec{x}) \\
& - \int_{\vec{x} \in \mathbb{L}} \hat{I}_k^{\text{dip}}(\vec{x}, s) \hat{E}_k^{\text{prb}}(\vec{x}, s) dL(\vec{x}) , \tag{2.23}
\end{aligned}$$

where we have used the thin wire approximation such that $\hat{J}_k^{\text{dip}}(\vec{x}, s) dV(\vec{x}) = \hat{I}_k^{\text{dip}}(\vec{x}, s) dL(\vec{x})$, with $\hat{I}_k^{\text{dip}}(\vec{x}, s)$ the electric current oriented along the tangent to \mathbb{L} . Note that the boundary integral consists of a contribution from $\mathbb{S}_0 \cup \mathbb{S}^+ \cup \mathbb{S}^-$, with normal pointed into \mathbb{D} , and a contribution from $\partial \mathbb{D}^{\text{out}}$ surrounding the contrast and the antenna system, with normal pointed out of \mathbb{D} .

The electric wavefield $\hat{E}_k^{\text{prb}}(\vec{x}, s)$ is caused by the probing electric-source-current density $\hat{J}_k^{\text{prb}}(s) \delta(\vec{x} - \vec{x}^{\text{prb}})$. Consequently, $\hat{E}_k^{\text{prb}}(\vec{x}, s)$ satisfies

$$\hat{E}_k^{\text{prb}}(\vec{x}, s) = \hat{\mathcal{G}}_{k,l}^{E,J}(\vec{x}|\vec{x}^{\text{prb}}, s) \hat{J}_l^{\text{prb}}(s) , \tag{2.24}$$

where $\hat{\mathcal{G}}_{k,l}^{E,J}(\vec{x}|\vec{x}^{\text{prb}}, s)$ is the electric-field/electric-current Green tensor, hence

$$\hat{\mathcal{G}}_{k,l}^{E,J}(\vec{x}|\vec{x}^{\text{prb}}, s) = \frac{1}{s\hat{\epsilon}} \left(-\hat{\gamma}^2 I_{k,l} + \partial_k \partial_l \right) \hat{G}(\vec{x}|\vec{x}^{\text{prb}}, s) , \tag{2.25}$$

where $\hat{G}(\vec{x}|\vec{x}', s)$ is the scalar Green function, viz.

$$\hat{G}(\vec{x}|\vec{x}', s) = \frac{\exp(-\hat{\gamma} |\vec{x} - \vec{x}'|)}{4\pi |\vec{x} - \vec{x}'|} , \tag{2.26}$$

in which $\hat{\gamma}$ satisfies

$$\hat{\gamma}^2 = s^2 \hat{\epsilon} \mu_0 , \tag{2.27}$$

and where the symmetric unit tensor $I_{k,l} = 1$ for $k = l$ and $I_{k,l} = 0$ for $k \neq l$.

Assuming that in both states the media at infinity are homogeneous and source-free, the first term on the right-hand side of equation (2.23) vanishes when one let $\partial\mathbb{D}^{\text{out}}$ tend to infinity.

The next three surface integrals are over the complete surface of the inaccessible volume domain containing the reflector. We let \mathbb{S}^+ and \mathbb{S}^- tend to \mathbb{S} , and in addition we let \mathbb{S}^0 around the edge of the reflector tend to the edge. Then in view of the edge conditions as formulated by Jones in 1964, the integral contribution over \mathbb{S}^0 vanishes, while we take the contribution from \mathbb{S}^+ and \mathbb{S}^- together as

$$\begin{aligned}
 & \epsilon_{m,k,j} \int_{\vec{x} \in \mathbb{S}^+} \nu_m \left(\hat{E}_k^{\text{prb}}(\vec{x}, s) \hat{H}_j^{\text{tot}}(\vec{x}, s) - \hat{E}_k^{\text{tot}}(\vec{x}, s) \hat{H}_j^{\text{prb}}(\vec{x}, s) \right) dA(\vec{x}) \\
 & + \epsilon_{m,k,j} \int_{\vec{x} \in \mathbb{S}^-} \nu_m \left(\hat{E}_k^{\text{prb}}(\vec{x}, s) \hat{H}_j^{\text{tot}}(\vec{x}, s) - \hat{E}_k^{\text{tot}}(\vec{x}, s) \hat{H}_j^{\text{prb}}(\vec{x}, s) \right) dA(\vec{x}) \\
 & = \int_{\vec{x} \in \mathbb{S}} \epsilon_{m,k,j} \nu_m \hat{E}_k^{\text{prb}}(\vec{x}, s) \left(\hat{H}_j^{\text{tot}}(\vec{x} + h\vec{\nu}, s) - \hat{H}_j^{\text{tot}}(\vec{x} - h\vec{\nu}, s) \right) dA(\vec{x}) \\
 & - \int_{\vec{x} \in \mathbb{S}} \epsilon_{m,k,j} \nu_m \hat{E}_k^{\text{tot}}(\vec{x}, s) \left(\hat{H}_j^{\text{prb}}(\vec{x} + h\vec{\nu}, s) - \hat{H}_j^{\text{prb}}(\vec{x} - h\vec{\nu}, s) \right) dA(\vec{x}) .
 \end{aligned} \tag{2.28}$$

Applying the boundary conditions for the perfectly conducting reflector at the right-hand side of equation (2.28), see equations (2.20) and (2.21), results in

$$\begin{aligned}
 \lim_{h \rightarrow 0} \int_{\vec{x} \in \mathbb{S}} \epsilon_{m,k,j} \nu_m \hat{E}_k^{\text{prb}}(\vec{x}, s) \left(\hat{H}_j^{\text{tot}}(\vec{x} + h\vec{\nu}, s) - \hat{H}_j^{\text{tot}}(\vec{x} - h\vec{\nu}, s) \right) dA(\vec{x}) \\
 = \int_{\vec{x} \in \mathbb{S}} \hat{E}_k^{\text{prb}}(\vec{x}, s) \hat{J}_k^{\text{rf}}(\vec{x}, s) dA(\vec{x}) , \tag{2.29}
 \end{aligned}$$

where \hat{J}_k^{rf} is the tangential electric-surface-current density from equation (2.21).

When we apply the results from above in equation (2.23), we obtain

$$\begin{aligned}
 0 = & - \int_{\vec{x} \in \mathbb{S}} \hat{\mathcal{G}}_{k,l}^{E,J}(\vec{x} | \vec{x}^{\text{prb}}, s) \hat{J}_l^{\text{prb}}(s) \hat{J}_k^{\text{rf}}(\vec{x}, s) dA(\vec{x}) \\
 & - \int_{\vec{x} \in \mathbb{D}^{\text{sct}}} s \left(\hat{\epsilon}^{\text{sct}}(\vec{x}, s) - \hat{\epsilon}^{\text{bg}}(s) \right) \hat{\mathcal{G}}_{k,l}^{E,J}(\vec{x} | \vec{x}^{\text{prb}}, s) \hat{J}_l^{\text{prb}}(s) \hat{E}_k^{\text{tot}}(\vec{x}, s) dV(\vec{x}) \\
 & + \hat{J}_k^{\text{prb}}(s) \hat{E}_k^{\text{tot}}(\vec{x}^{\text{prb}}, s) \\
 & - \int_{\vec{x} \in \mathbb{L}} \hat{\mathcal{G}}_{k,l}^{E,J}(\vec{x} | \vec{x}^{\text{prb}}, s) \hat{J}_l^{\text{prb}}(s) \hat{J}_k^{\text{dip}}(\vec{x}, s) dL(\vec{x}) , \tag{2.30}
 \end{aligned}$$

and, in view of the arbitrariness of $\hat{J}_k^{\text{prb}}(s)$, it reduces to

$$\begin{aligned} \hat{E}_k^{\text{tot}}(\vec{x}^{\text{prb}}, s) = & \int_{\vec{x} \in \mathbb{S}} \hat{\mathcal{G}}_{k,l}^{E,J}(\vec{x}^{\text{prb}}|\vec{x}, s) \hat{J}_l^{\text{rf}}(\vec{x}, s) dA(\vec{x}) \\ & + \int_{\vec{x} \in \mathbb{D}^{\text{sct}}} s \left(\hat{\varepsilon}^{\text{sct}}(\vec{x}, s) - \hat{\varepsilon}^{\text{bg}}(s) \right) \hat{\mathcal{G}}_{k,l}^{E,J}(\vec{x}^{\text{prb}}|\vec{x}, s) \hat{E}_l^{\text{tot}}(\vec{x}, s) dV(\vec{x}) \\ & + \int_{\vec{x} \in \mathbb{L}} \hat{\mathcal{G}}_{k,l}^{E,J}(\vec{x}^{\text{prb}}|\vec{x}, s) \hat{I}_l^{\text{dip}}(\vec{x}, s) dL(\vec{x}) . \end{aligned} \quad (2.31)$$

The three terms on the right-hand side are denoted as follows. The third term describes the electric wavefield from the wire with electric current $\hat{I}_l^{\text{dip}}(\vec{x}, s)$. The first term describes the field due to the presence of the reflector at \mathbb{S} , while the second term describes the field due to the presence of the scatterer at \mathbb{D}^{sct} . Hence, we write the total field as a superposition of three contributions, viz.

$$\hat{E}_k^{\text{tot}}(\vec{x}, s) = \hat{E}_k^{\text{dip}}(\vec{x}, s) + \hat{E}_k^{\text{rf}}(\vec{x}, s) + \hat{E}_k^{\text{sct}}(\vec{x}, s) , \quad (2.32)$$

where the dipole and the reflected wavefields satisfy

$$\hat{E}_k^{\text{dip}}(\vec{x}, s) = \int_{\vec{x}' \in \mathbb{L}} \hat{\mathcal{G}}_{k,l}^{E,J}(\vec{x}|\vec{x}', s) \hat{I}_l^{\text{dip}}(\vec{x}', s) dL(\vec{x}') , \quad (2.33)$$

$$\hat{E}_k^{\text{rf}}(\vec{x}, s) = \int_{\vec{x}' \in \mathbb{S}} \hat{\mathcal{G}}_{k,l}^{E,J}(\vec{x}|\vec{x}', s) \hat{J}_l^{\text{rf}}(\vec{x}', s) dA(\vec{x}') , \quad (2.34)$$

and where the scattered electric wavefield reads

$$\hat{E}_k^{\text{sct}}(\vec{x}, s) = \int_{\vec{x}' \in \mathbb{D}^{\text{sct}}} s \left(\hat{\varepsilon}^{\text{sct}}(\vec{x}', s) - \hat{\varepsilon}^{\text{bg}}(s) \right) \hat{\mathcal{G}}_{k,l}^{E,J}(\vec{x}|\vec{x}', s) \hat{E}_l^{\text{tot}}(\vec{x}', s) dV(\vec{x}') . \quad (2.35)$$

Consequently, we can define an electric wavefield due to the antenna system itself, viz.

$$\hat{E}_k^{\text{inc}}(\vec{x}, s) = \hat{E}_k^{\text{dip}}(\vec{x}, s) + \hat{E}_k^{\text{rf}}(\vec{x}, s) . \quad (2.36)$$

Note that we have obtained a complete framework for both the antenna system and the interpretation of data to be obtained with the system. This framework serves as a basis for this thesis. Consequently, we discuss in the next chapter the computation of the incident wavefield from the antenna system.

Chapter 3

Design of directional borehole radar

In this chapter we compute the directional radiation patterns of various borehole antenna configurations, all based on the same principle. After the optimum configuration is obtained, a prototype is built. The radiation pattern of this prototype is measured and used for verification of the numerical model.

There are mainly two methods to emit a directional electromagnetic wave-field out of a borehole into the subsurface. One is via a magnetic dipole, while the other one uses an electric dipole where the omni-directional radiation pattern is disturbed by positioning a reflector next to the dipole. We have chosen the second option, see figure 3.1, since the radiation resistance of the electric dipole is much larger than the one of the magnetic dipole, as shown by Balanis in 1997. Therefore, more power is dissipated into the subsurface in the form of electromagnetic waves. Our choice is supported by experiments with magnetic loop antennas (Chignell *et al.*, 1988), where explicitly preference is given for electric dipoles in ground-probing methods. Parallel to the dipole we positioned as reflector a “perfectly” conducting plate. For microwave antennas, the parabolic reflector is one of the most widely used, see e.g. Skolnik (1981). In optics, such a parabolic curvature results in a parallel beam if the source is positioned in the focal point of the reflector. This would be the most preferable radiation pattern. In the microwave region this “focussing” effect is not feasible since the wavelength is of the same order of magnitude of the construction. However, we expect to arrive at some directional radiation pattern using a parabolically curved cylindrical reflector. In this chapter we also investigate the effect of a circularly curved cylindrical reflector. Therefore, we describe our antenna configuration in a curvilinear coordinate system so that we can deal

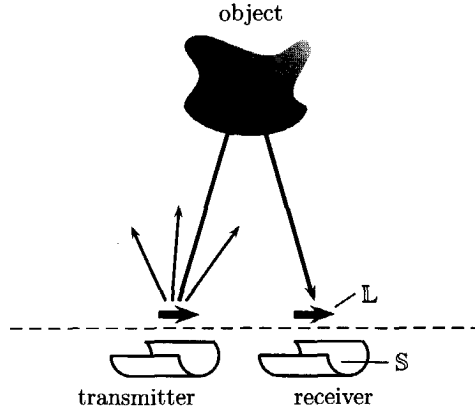


Figure 3.1: The bistatic antenna configuration.

with the parabolic and the circular reflector simultaneously.

Before we start computing the various radiation patterns, we need to discuss two aspects of the system. First of all, there is mainly one interesting frequency range, which is around 100 MHz. This is a compromise between spatial resolution and penetration. A higher frequency will result in more resolution but in less penetration and vice versa.

The second point considers the limitations on the spatial dimensions of the borehole radar system. Since the antenna system must fit in a single borehole, we have chosen for a bistatic setup where the diameter of the antenna system does not exceed 0.09 m. This is much smaller than the wavelength of a 100 MHz wave in free space. Consequently, the influence of the reflector on the radiation pattern will be very small. To increase this influence, the effective wavelength is shortened by embedding the system in water.

3.1 Antenna configuration

An electric dipole in a curvilinear coordinate system with position vector $\vec{v} = v_i$, see figure 3.2, is defined in the one-dimensional domain \mathbb{L} , having a length of $2l$ in the \vec{e}_{v_1} -direction and located at v_2^{dip} in the \vec{e}_{v_2} -direction and v_3^{dip} in the \vec{e}_{v_3} -direction, hence

$$\mathbb{L} = \{\vec{v} \in \mathbb{R}^3 \mid -l < v_1 < l, v_2 = v_2^{\text{dip}}, v_3 = v_3^{\text{dip}}\}. \quad (3.1)$$

In the dipole domain, a sinusoidal external electric current is present, which vanishes at the end points and has a maximum in the center (see e.g. Bal-

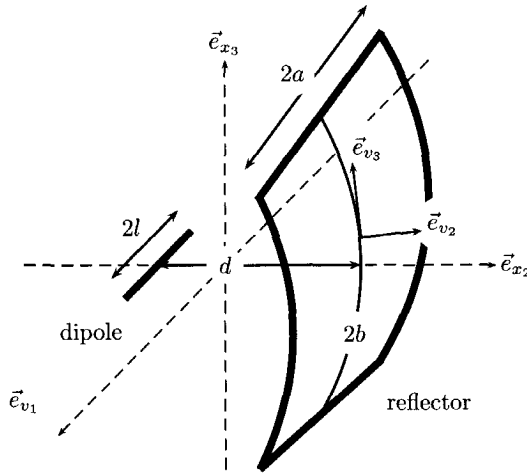


Figure 3.2: The antenna configuration in the curvilinear coordinate system. A reflector of length $2a$ in the \vec{e}_{v_1} -direction is positioned at a distance d in the \vec{e}_{v_2} -direction from the dipole and curved over $2b$ in the \vec{e}_{v_3} -direction. The dipole has a length of $2l$ in the \vec{e}_{v_1} -direction.

anis, 1997). Parallel to this dipole, a perfectly conducting reflector having a length of $2a$ in the \vec{e}_{v_1} -direction, is positioned at v_2^{rf} with a fixed distance d in the \vec{e}_{v_2} -direction from the dipole and is curved over $2b$ in the \vec{e}_{v_3} -direction. Consequently, the surface \mathbb{S} of this reflector is defined as

$$\mathbb{S} = \{\vec{v} \in \mathbb{R}^3 \mid -a < v_1 < a, v_2 = v_2^{\text{rf}}, -b < v_3 < b\}. \quad (3.2)$$

The antenna configuration is positioned in a homogeneous background medium with constant complex permittivity $\hat{\varepsilon}$, where $\hat{\varepsilon}$ reads

$$\hat{\varepsilon} = \varepsilon_0 \varepsilon_r + \frac{\sigma}{s}, \quad (3.3)$$

with ε_r the relative permittivity and σ the conductivity of the medium. Besides, the medium is assumed to be nonmagnetically susceptible, i.e. the relative permeability μ_r is equal to one. Furthermore, the symbol $\hat{\cdot}$ on top of a given quantity or parameter denotes that it is defined in the temporal Laplace domain with Laplace parameter s . Frequency domain results are obtained by taking the limit

$$s \rightarrow -i\omega, \quad (3.4)$$

where $\omega = 2\pi f$, in which f is the temporal frequency.

3.2 Formulation of integral equation

In chapter 2 it is derived that the wavefield from the antenna system into the surrounding medium may be decomposed as

$$\hat{E}_{v_l}^{\text{inc}}(\vec{v}) = \hat{E}_{v_l}^{\text{dip}}(\vec{v}) + \hat{E}_{v_l}^{\text{rf}}(\vec{v}) , \quad \forall \vec{v} \in \mathbb{R}^3 , \quad (3.5)$$

where $\hat{E}_{v_l}^{\text{inc}}(\vec{v})$ is the incident electric wavefield defined in the orthogonal curvilinear coordinate system with unit vector \vec{e}_{v_l} at the position \vec{v} , where $\hat{E}_{v_l}^{\text{dip}}(\vec{v})$ is the dipole wavefield, and where $\hat{E}_{v_l}^{\text{rf}}(\vec{v})$ is the reflected wavefield, see equation (2.36). In appendix A, more information on the orthogonal curvilinear coordinate system is given. In view of the electromagnetic boundary condition, the tangential components of the incident electric wavefield vanishes at the surface of the reflector, see equation (2.20), therefore

$$-\hat{E}_{v_\alpha}^{\text{dip}}(\vec{v}) = \hat{E}_{v_\alpha}^{\text{rf}}(\vec{v}) , \quad \forall \vec{v} \in \mathbb{S} , \quad \forall \alpha \in \{1, 3\} . \quad (3.6)$$

To emphasize the tangential character of the above quantities, we introduced Greek subscripts, like α or β . These can only be one or three from here on. For repeated Greek subscripts the Einstein summation convention is used as well. Consequently, it is obtained, in combination with equation (2.34), that the reflected wavefield satisfies

$$\hat{E}_{v_\alpha}^{\text{rf}}(\vec{v}) = \frac{1}{s\hat{\epsilon}} [-\hat{\gamma}^2 I_{\alpha,i} + \nabla_{v_\alpha} \nabla_{v_i}] T_{i,j}^{-1} \int_{\vec{v}' \in \mathbb{S}} \hat{G}(\vec{v}|\vec{v}') T_{j,\beta}(\vec{v}|\vec{v}') \hat{J}_{v_\beta}^{\text{rf}}(\vec{v}') dA(\vec{v}') , \quad (3.7)$$

where $\hat{J}_{v_\beta}^{\text{rf}}(\vec{v}')$ is the jump in electric-surface-current density over the plate domain \mathbb{S} of the reflector, $\nabla_{v_j} \nabla_{v_i}$ is the gradient divergence operator in the curvilinear orthogonal coordinate system, $I_{j,i}$ is the symmetric unit tensor, $T_{i,j}^{-1}$ and $T_{j,i}$ are the coordinate transformation matrices as defined in appendix A. Finally, the Green scalar function $\hat{G}(\vec{v}|\vec{v}')$ reads

$$\hat{G}(\vec{v}|\vec{v}') = \frac{\exp(-\hat{\gamma}\rho)}{4\pi\rho} , \quad (3.8)$$

in which the distance ρ is defined in the Cartesian coordinate, hence

$$\rho = \left\{ [x_1(\vec{v}) - x_1(\vec{v}')]^2 + [(x_2(\vec{v}) - x_2(\vec{v}')]^2 + [x_3(\vec{v}) - x_3(\vec{v}')]^2 \right\}^{\frac{1}{2}} , \quad (3.9)$$

and where $\hat{\gamma}$ satisfies

$$\hat{\gamma}^2 = s^2 \hat{\epsilon} \mu_0 , \quad (3.10)$$

see equations (2.24)-(2.27). The tangential components the gradient-divergence operator $\nabla_{v_\alpha} \nabla_{v_i}$ can be factorized into two terms, one containing only spatial

derivatives in the direction tangential to the reflector while the other one contains the remaining normal derivatives, viz.

$$\begin{aligned} \nabla_{v_\alpha} \nabla_{v_i} &= \begin{pmatrix} \frac{1}{h_1} \partial_1 \frac{1}{h_{1,2,3}} \partial_1 h_{2,3} & \frac{1}{h_1} \partial_1 \frac{1}{h_{1,2,3}} \partial_2 h_{1,3} & \frac{1}{h_1} \partial_1 \frac{1}{h_{1,2,3}} \partial_3 h_{1,2} \\ \frac{1}{h_3} \partial_3 \frac{1}{h_{1,2,3}} \partial_1 h_{2,3} & \frac{1}{h_3} \partial_3 \frac{1}{h_{1,2,3}} \partial_2 h_{1,3} & \frac{1}{h_3} \partial_3 \frac{1}{h_{1,2,3}} \partial_3 h_{1,2} \end{pmatrix} \\ &= D_{v_{\alpha,i'}}^T D_{v_{i',i}}^N, \end{aligned} \quad (3.11)$$

where

$$D_{v_{\alpha,i'}}^T = \begin{pmatrix} D_{v_{1,1}}^T & D_{v_{1,2}}^T & D_{v_{1,3}}^T \\ D_{v_{3,1}}^T & D_{v_{3,2}}^T & D_{v_{3,3}}^T \end{pmatrix}, \quad (3.12)$$

$$= \begin{pmatrix} \frac{1}{h_1} \partial_1 \frac{1}{h_{1,2,3}} \partial_1 h_{2,3} & \frac{1}{h_1} \partial_1 \frac{1}{h_{1,2,3}} \partial_2 h_{1,3} & \frac{1}{h_1} \partial_1 \frac{1}{h_{1,2,3}} \partial_3 h_{1,2} \\ \frac{1}{h_3} \partial_3 \frac{1}{h_{1,2,3}} \partial_1 h_{2,3} & \frac{1}{h_3} \partial_3 \frac{1}{h_{1,2,3}} \partial_2 h_{1,3} & \frac{1}{h_3} \partial_3 \frac{1}{h_{1,2,3}} \partial_3 h_{1,2} \end{pmatrix}, \quad (3.13)$$

and

$$D_{v_{i',i}}^N = \begin{pmatrix} 1 & 0 & 0 \\ 0 & \partial_2 h_{1,3} & 0 \\ 0 & 0 & 1 \end{pmatrix}, \quad (3.14)$$

with Lamé coefficients $h_{1,2,3} = h_{v_1} h_{v_2} h_{v_3}$, $h_{i,j} = h_{v_i} h_{v_j}$, $h_i = h_{v_i}$ and spatial derivatives $\partial_i = \partial_{v_i}$.

Combining equations (3.6)-(3.14) results in an integral equation in a curvilinear coordinate system. We write this integral equation as

$$-\hat{E}_{v_\alpha}^{\text{dip}}(\vec{v}) = \frac{1}{s\hat{\varepsilon}} \left[-\hat{\gamma}^2 I_{\alpha,i} \hat{A}_{v_i}^{\text{rf}}(\vec{v}) + D_{v_{\alpha,i'}}^T \hat{B}_{v_{i'}}^{\text{rf}}(\vec{v}) \right], \quad \forall \vec{v} \in \mathbb{S}, \quad (3.15)$$

where

$$\hat{B}_{v_{i'}}^{\text{rf}}(\vec{v}) = D_{v_{i',i}}^N \hat{A}_{v_i}^{\text{rf}}(\vec{v}), \quad (3.16)$$

and where

$$\hat{A}_{v_i}^{\text{rf}}(\vec{v}) = T_{i,j}^{-1} \mathcal{F}^{(-1)} \left[\int_{\vec{v}' \in \mathbb{S}} \mathcal{F} \left[\hat{G}(\vec{v}|\vec{v}') \right] T_{j,\beta} \mathcal{F} \left[\hat{J}_{v_\beta}^{\text{rf}}(\vec{v}') \right] dA(\vec{v}') \right], \quad (3.17)$$

where we use the spatial Fourier transform $\mathcal{F}[\cdot]$ to carry out the spatial convolution in the \vec{e}_{v_1} -direction. In order to obtain the incident electric wavefield, the integral equation has to be solved for the unknown electric-surface-current density $\hat{J}_{v_\beta}^{\text{rf}}(\vec{v}')$, while we know the electric dipole wavefield $\hat{E}_{v_\alpha}^{\text{dip}}(\vec{v})$ from the external electric current in the dipole domain.

If the reflector was defined as a surface in the (x_1, x_3) -plane in a Cartesian reference frame, the complete problem could have been solved in the Cartesian coordinate system. In this case the transformation matrices in equation (3.17) become the identity matrices and both the electric-surface-current density and vector potential have only values unequal to zero for their x_1 - and x_3 -components. Therefore, the partial derivative in the \vec{e}_{x_2} -direction, ∂_{x_2} , in the operator $D_{x_{i'},i}^N$ loses its significance and becomes zero. What remains is a simpler problem, where the integral equation from equations (3.6)-(3.14) would read

$$-\hat{E}_{x_\alpha}^{\text{dip}}(\vec{x}) = \frac{1}{s\hat{\epsilon}} [-\hat{\gamma}^2 I_{\alpha,i} + D_{x_{\alpha,i'}}^T D_{x_{i'},i}^N] \hat{A}_{x_\beta}^{\text{rf}}(\vec{x}), \quad (3.18)$$

where

$$\hat{A}_{x_\beta}^{\text{rf}}(\vec{x}) = \int_{\vec{x}' \in \mathbb{S}} \hat{G}(\vec{x}|\vec{x}') \hat{J}_{x_\beta}^{\text{rf}}(\vec{x}') dA(\vec{x}'), \quad \forall \vec{x} \in \mathbb{S}, \quad (3.19)$$

and where the operators $D_{x_{\alpha,i'}}^T$ and $D_{x_{i'},i}^N$ simplify to

$$D_{x_{\alpha,i'}}^T = \begin{pmatrix} D_{v_{1,1}}^T & D_{v_{1,2}}^T & D_{v_{1,3}}^T \\ D_{v_{3,1}}^T & D_{v_{3,2}}^T & D_{v_{3,3}}^T \end{pmatrix} = \begin{pmatrix} \partial_{x_1}^2 & 0 & \partial_{x_1} \partial_{x_3} \\ \partial_{x_3} \partial_{x_1} & 0 & \partial_{x_3}^2 \end{pmatrix}, \quad (3.20)$$

and

$$D_{x_{i'},i}^N = \begin{pmatrix} 1 & 0 & 0 \\ 0 & 0 & 0 \\ 0 & 0 & 1 \end{pmatrix}. \quad (3.21)$$

This plate problem is solved by Zwamborn and Van den Berg (1991).

3.3 Discretization of integral equation

To solve the integral equation of (3.15)-(3.17) numerically, we develop a discretized version. This version is analogous to the discretization procedure in the Cartesian coordinates system suggested by Zwamborn and Van den Berg

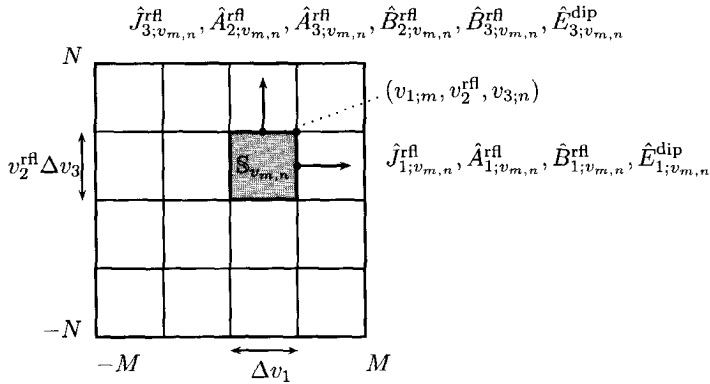


Figure 3.3: The discretization of the plate domain \mathbb{S} into $2M \times 2N$ cells in the v_1 - and v_3 -direction, respectively. Each cell represents a subdomain $\mathbb{S}_{v_{m,n}}$.

(1991). Consequently, the domain \mathbb{S} is discretized in $2M \times 2N$ subdomains $\mathbb{S}_{v_{m,n}}$, with

$$\mathbb{S}_{v_{m,n}} = \left\{ \vec{v} \in \mathbb{R}^3 \mid v_{1;m-1} < v_1 \leq v_{1;m}, v_2 = v_2^{\text{rfi}}, v_{3;n-1} < v_3 \leq v_{3;n} \right\}, \quad (3.22)$$

where

$$v_{1;m} = m\Delta v_1, \quad \forall m = -M, \dots, M, \quad (3.23)$$

$$v_{3;n} = n\Delta v_3, \quad \forall n = -N, \dots, N, \quad (3.24)$$

are the grid points positions of the subdomains, see figure 3.3. We furthermore need the normal derivative of the vector potential. We therefore introduce three discrete coordinate points in the normal direction, viz.

$$v_{2;p} = v_2^{\text{rfi}} + p\Delta v_1, \quad \forall p = -1, 0, 1. \quad (3.25)$$

This enables us to replace the normal derivative by a central finite-difference rule. We define the quantities of the continuous integral equation on a staggered grid as follows

$$\hat{E}_{\alpha;v_{m,n}}^{\text{dip}} = \begin{pmatrix} \hat{E}_{1;v_{m,n}}^{\text{dip}} \\ \hat{E}_{3;v_{m,n}}^{\text{dip}} \end{pmatrix} = \begin{pmatrix} \hat{E}_{v_1}^{\text{dip}}(m\Delta v_1, v_2^{\text{rfi}}, (n - \frac{1}{2})\Delta v_3) \\ \hat{E}_{v_3}^{\text{dip}}((m - \frac{1}{2})\Delta v_1, v_2^{\text{rfi}}, n\Delta v_3) \end{pmatrix}, \quad (3.26)$$

$$\hat{B}_{i;v_{m,n}}^{\text{rf}} = \begin{pmatrix} \hat{B}_{1;v_{m,n}}^{\text{rf}} \\ \hat{B}_{3;v_{m,n}}^{\text{rf}} \end{pmatrix} = \begin{pmatrix} \hat{B}_{v_1}^{\text{rf}}(m\Delta v_1, v_2^{\text{rf}}, (n - \frac{1}{2})\Delta v_3) \\ \hat{B}_{v_2}^{\text{rf}}((m - \frac{1}{2})\Delta v_1, v_2^{\text{rf}}, n\Delta v_3) \\ \hat{B}_{v_3}^{\text{rf}}((m - \frac{1}{2})\Delta v_1, v_2^{\text{rf}}, n\Delta v_3) \end{pmatrix}, \quad (3.27)$$

$$\hat{A}_{i;v_{m,p,n}}^{\text{rf}} = \begin{pmatrix} \hat{A}_{1;v_{m,p,n}}^{\text{rf}} \\ \hat{A}_{2;v_{m,p,n}}^{\text{rf}} \\ \hat{A}_{3;v_{m,p,n}}^{\text{rf}} \end{pmatrix} = \begin{pmatrix} \hat{A}_{v_1}^{\text{rf}}(m\Delta v_1, v_2^{\text{rf}} + p\Delta v_2, (n - \frac{1}{2})\Delta v_3) \\ \hat{A}_{v_2}^{\text{rf}}((m - \frac{1}{2})\Delta v_1, v_2^{\text{rf}} + p\Delta v_2, n\Delta v_3) \\ \hat{A}_{v_3}^{\text{rf}}((m - \frac{1}{2})\Delta v_1, v_2^{\text{rf}} + p\Delta v_2, n\Delta v_3) \end{pmatrix}, \quad (3.28)$$

$$\hat{J}_{\beta;v_{m,n}}^{\text{rf}} = \begin{pmatrix} \hat{J}_{1;v_{m,n}}^{\text{rf}} \\ \hat{J}_{3;v_{m,n}}^{\text{rf}} \end{pmatrix} = \begin{pmatrix} \hat{J}_{v_1}^{\text{rf}}(m\Delta v_1, v_2^{\text{rf}}, (n - \frac{1}{2})\Delta v_3) \\ \hat{J}_{v_3}^{\text{rf}}((m - \frac{1}{2})\Delta v_1, v_2^{\text{rf}}, n\Delta v_3) \end{pmatrix}, \quad (3.29)$$

where each component is defined for a range of indices values m , p and n , viz.

$$\begin{aligned} \hat{E}_{1;v_{m,n}}^{\text{dip}} &, \quad m = -M+1, \dots, M-1, \quad n = -N+1, \dots, N, \\ \hat{E}_{3;v_{m,n}}^{\text{dip}} &, \quad m = -M+1, \dots, M, \quad n = -N+1, \dots, N-1, \\ \hat{B}_{1;v_{m,n}}^{\text{rf}} &, \quad m = -M-1, \dots, M+1, \quad n = -N, \dots, N+1, \\ \hat{B}_{\{2,3\};v_{m,n}}^{\text{rf}} &, \quad m = -M, \dots, M+1, \quad n = -N-1, \dots, N+1, \\ \hat{A}_{1;v_{m,p,n}}^{\text{rf}} &, \quad m = -M-1, \dots, M+1, \quad n = -N, \dots, N+1, \quad p = -1, 0, 1, \\ \hat{A}_{\{2,3\};v_{m,p,n}}^{\text{rf}} &, \quad m = -M, \dots, M+1, \quad n = -N-1, \dots, N+1, \quad p = -1, 0, 1, \\ \hat{J}_{1;v_{m,n}}^{\text{rf}} &, \quad m = -M+1, \dots, M-1, \quad n = -N+1, \dots, N, \\ \hat{J}_{3;v_{m,n}}^{\text{rf}} &, \quad m = -M+1, \dots, M, \quad n = -N+1, \dots, N-1. \end{aligned}$$

Note the differences in subscript notation for a vector defined in the plate domain \mathbb{S} versus the domain \mathbb{R}^3 , i.e.

$$\{v_{m,n} = (v_{1;m}, v_2^{\text{rf}}, v_{3;n})\} \in \mathbb{S}, \quad (3.30)$$

$$\{v_{m,p,n} = (v_{1;m}, v_{2;p}, v_{3;n})\} \in \mathbb{R}^3. \quad (3.31)$$

The discretized form of the integral equation in (3.15)-(3.17) results in a set of equations which reads

$$\hat{E}_{\alpha;v_{m,n}}^{\text{dip}} = \frac{1}{s\hat{\epsilon}} \left[-\gamma^2 I_{\alpha,i} \hat{A}_{i;v_{m,p=0,n}}^{\text{rf}} + D_{v_{\alpha,i'};v_{m,n}}^T \hat{B}_{i';v_{m,n}}^{\text{rf}} \right], \quad (3.32)$$

$$\hat{B}_{i';v_{m,n}}^{\text{rf}} = D_{v_{i',i};v_{m,p,n}}^N \hat{A}_{i;v_{m,p,n}}^{\text{rf}}, \quad (3.33)$$

$$\hat{A}_{1;v_m,p,n}^{\text{rf}} = \text{DFT}_{v_1}^{-1} \left[\sum_{n'=-N+1}^N \text{DFT}_{v_1} \left[\langle \hat{G} \rangle (\vec{v}_{m,p,n} | \vec{v}_{m,n'}) \right] \right. \\ \left. \text{DFT}_{v_1} \left[\hat{J}_{1;v_m,n'}^{\text{rf}} \right] h_{v_3;v_m,n'} \Delta v_3 \right], \quad (3.34)$$

$$\hat{A}_{i;v_m,p,n}^{\text{rf}} = T_{ij;v_m,p,n}^{-1} \text{DFT}_{v_1}^{-1} \left[\sum_{n'=-N+1}^{N-1} \text{DFT}_{v_1} \left[\langle \hat{G} \rangle (\vec{v}_{m,p,n} | \vec{v}_{m,n'}) \right] T_{j3;v_m,n} \right. \\ \left. \text{DFT}_{v_1} \left[\hat{J}_{3;v_m,n'}^{\text{rf}} \right] h_{v_3;v_m,n'} \Delta v_3 \right], \quad \forall i = \{2, 3\}, \quad (3.35)$$

and where we have replaced the continuous spatial Fourier transform $\mathcal{F}[\cdot]$ by its discrete counterpart $\text{DFT}[\cdot]$. Note that by omitting the coordinate transformation matrices in equation (3.34) and the Lamé coefficient $h_{v_1;v_m',n'}$ in equations (3.34) and (3.35), we explicitly use the fact that we choose the \vec{e}_{v_1} -direction of the orthogonal curvilinear coordinate system similar to the \vec{e}_{x_1} -direction of the Cartesian coordinate system. Therefore, we obtain that $v_1 = x_1$, that the Lamé coefficient of the \vec{e}_{v_1} -direction is equal to one, $h_{v_1} = 1$, while the other Lamé coefficients become independent of the parameter v_1 and that the transformation matrices are independent of the parameter v_1 . Finally, we use the knowledge that the components of the electric-surface-current density perpendicular to the edges vanishes at the edges, viz.

$$\hat{J}_{1;v_m,n}^{\text{rf}} = 0, \quad m = -M, M, \quad n = -N, \dots, N, \quad (3.36)$$

$$\hat{J}_{3;v_m,n}^{\text{rf}} = 0, \quad m = -M, \dots, M, \quad n = -N, N. \quad (3.37)$$

The spatial derivatives appearing in equations (3.32) and (3.33) are approximated via the finite difference rules as given by Abramowitz and Stegun (1970), hence

$$\hat{B}_{i';v_m,n}^{\text{rf}} = D_{v_{i'},i';v_m,p,n}^N \hat{A}_{i';v_m,p,n}^{\text{rf}} \\ = \begin{pmatrix} \hat{A}_{1;v_m,0,n}^{\text{rf}} \\ \partial_{v_2} h_{v_3} \hat{A}_{2;v_m,p,n}^{\text{rf}} \\ \hat{A}_{3;v_m,0,n}^{\text{rf}} \end{pmatrix} \\ = \begin{pmatrix} \hat{A}_{1;v_m,0,n}^{\text{rf}} \\ \frac{1}{2\Delta v_2} \left(h_{v_3;v+1,n} \hat{A}_{2;v_m,1,n}^{\text{rf}} - h_{v_3;v-1,n} \hat{A}_{2;v_m,-1,n}^{\text{rf}} \right) \\ \hat{A}_{3;v_m,0,n}^{\text{rf}} \end{pmatrix}, \quad (3.38)$$

$$\begin{aligned}
D_{v_{1i'};v_{m,n}}^T \hat{B}_{i';v_{m,n}}^{\text{rf}} &= \partial_{v_1}^2 \hat{B}_{1;v_{m,n}}^{\text{rf}} + \frac{1}{h_{v_2} h_{v_3}} \partial_{v_1} \hat{B}_{2;v_{m,n}}^{\text{rf}} + \frac{1}{h_{v_2} h_{v_3}} \partial_{v_1} \partial_{v_3} h_{v_2} \hat{B}_{3;v_{m,n}}^{\text{rf}} \\
&= \frac{1}{(\Delta v_1)^2} \left(\hat{B}_{1;v_{m+1,n}}^{\text{rf}} - 2\hat{B}_{1;v_{m,n}}^{\text{rf}} + \hat{B}_{1;v_{m-1,n}}^{\text{rf}} \right) \\
&\quad + \frac{1}{h_{v_2;n-\frac{1}{2}} h_{v_3;n-\frac{1}{2}}} \frac{1}{2\Delta v_1} \left(\hat{B}_{2;v_{m+1,n}}^{\text{rf}} - \hat{B}_{2;v_{m,n}}^{\text{rf}} + \hat{B}_{2;v_{m+1,n-1}}^{\text{rf}} - \hat{B}_{2;v_{m,n-1}}^{\text{rf}} \right) \\
&\quad + \frac{1}{h_{v_2;n-\frac{1}{2}} h_{v_3;n-\frac{1}{2}}} \frac{1}{\Delta v_1 \Delta v_3} \left(h_{v_2;n} \hat{B}_{3;v_{m+1,n}}^{\text{rf}} - h_{v_2;n-1} \hat{B}_{3;v_{m+1,n-1}}^{\text{rf}} \right. \\
&\quad \left. - h_{v_2;n} \hat{B}_{3;v_{m,n}}^{\text{rf}} + h_{v_2;n-1} \hat{B}_{3;v_{m,n-1}}^{\text{rf}} \right), \quad (3.39)
\end{aligned}$$

and

$$\begin{aligned}
D_{v_{3i'};v_{m,n}}^T \hat{B}_{i';v_{m,n}}^{\text{rf}} &= \frac{1}{h_{v_3}} \partial_{v_3} \partial_{v_1} \hat{B}_{1;v_{m,n}}^{\text{rf}} + \frac{1}{h_{v_3}} \partial_{v_3} \frac{1}{h_{v_2} h_{v_3}} \hat{B}_{2;v_{m,n}}^{\text{rf}} + \frac{1}{h_{v_3}} \partial_{v_3} \frac{1}{h_{v_2} h_{v_3}} \partial_{v_3} h_{v_2} \hat{B}_{3;v_{m,n}}^{\text{rf}} \\
&= \frac{1}{h_{v_3;n}} \frac{1}{\Delta v_1 \Delta v_3} \left(\hat{B}_{1;v_{m,n+1}}^{\text{rf}} - \hat{B}_{1;v_{m-1,n+1}}^{\text{rf}} - \hat{B}_{1;v_{m,n}}^{\text{rf}} + \hat{B}_{1;v_{m-1,n}}^{\text{rf}} \right) \\
&\quad + \frac{1}{h_{v_3;n}} \frac{1}{2\Delta v_3} \left(\frac{1}{h_{v_2;n+1} h_{v_3;n+1}} \hat{B}_{2;v_{m,n+1}}^{\text{rf}} - \frac{1}{h_{v_2;n-1} h_{v_3;n-1}} \hat{B}_{2;v_{m,n-1}}^{\text{rf}} \right) \\
&\quad + \frac{1}{h_{v_3;n}} \frac{1}{(\Delta v_3)^2} \left(\frac{1}{h_{v_2;n+\frac{1}{2}} h_{v_3;n+\frac{1}{2}}} \left(h_{v_2;n+1} \hat{B}_{3;v_{m,n+1}}^{\text{rf}} - h_{v_2;n} \hat{B}_{3;v_{m,n}}^{\text{rf}} \right) \right. \\
&\quad \left. - \frac{1}{h_{v_2;n-\frac{1}{2}} h_{v_3;n-\frac{1}{2}}} \left(h_{v_2;n} \hat{B}_{3;v_{m,n}}^{\text{rf}} - h_{v_2;n-1} \hat{B}_{3;v_{m,n-1}}^{\text{rf}} \right) \right), \quad (3.40)
\end{aligned}$$

with Lamé coefficients

$$h_{v_i;n} = h_{v_i}(v_2 = v_2^{\text{rf}}, v_3 = n\Delta v_3), \quad (3.41)$$

$$h_{v_i;\pm 1,n} = h_{v_i}(v_2 = v_2^{\text{rf}} \pm \Delta v_2, v_3 = n\Delta v_3). \quad (3.42)$$

Finally, the Green function $\hat{G}(\vec{v}|\vec{v}')$ is approximated by its weak form $\langle \hat{G} \rangle(\vec{v}_{m,p,n}|\vec{v}_{m',n'})$. Therefore, we integrate the Green function over a sphere in the Cartesian coordinate system with radius $\frac{1}{2}\Delta d$, after which the result is

divided by the volume of the sphere, as done by Zwamborn (1991), viz.

$$\langle \hat{G} \rangle (\vec{v}_{m,p,n} | \vec{v}_{m',n'}) = \begin{cases} \frac{\left[\cosh(\frac{1}{2}\hat{\gamma}\Delta d) - \frac{\sinh(\frac{1}{2}\hat{\gamma}\Delta d)}{\frac{1}{2}\hat{\gamma}\Delta d} \right] \exp(-\hat{\gamma}\rho)}{\frac{1}{3}\pi\rho(\hat{\gamma}\Delta d)^2} & \forall \rho \geq \frac{1}{2}\Delta d, \\ \frac{1 - (1 + \frac{1}{2}\hat{\gamma}\Delta d) \exp(-\frac{1}{2}\hat{\gamma}\Delta d) \frac{\sinh(\hat{\gamma}\rho)}{\hat{\gamma}\rho}}{\frac{1}{6}\pi(\hat{\gamma}\Delta d)^2\Delta d} & \forall \rho < \frac{1}{2}\Delta d, \\ \frac{3 - (3 + \frac{3}{2}\hat{\gamma}\Delta d) \exp(-\frac{1}{2}\hat{\gamma}\Delta d)}{\frac{1}{2}\pi(\hat{\gamma}\Delta d)^2\Delta d} & \forall \rho = 0, \end{cases} \quad (3.43)$$

where Δd satisfies

$$\Delta d = \min (\Delta v_1, h_{v_2;v_{m,p,n}} \Delta v_2, h_{v_3;v_{m,p,n}} \Delta v_3) . \quad (3.44)$$

Hence, we arrive at a linear system of equations replacing our integral equation (3.15)-(3.17). We opt for an iterative conjugate gradient solution method, similar to what Zwamborn and Van den Berg (1991) did with their plate problems.

3.4 Conjugate gradient solution scheme

To underline the conjugate gradient method we introduce an operator notation. Therefore, the discretized integral equation in equations (3.32)-(3.35) is written in operator notation as

$$\mathbf{f} = \mathbf{L} \mathbf{u} , \quad (3.45)$$

with \mathbf{f} the known electric dipole wavefield, $\hat{E}_{\alpha;v_{m,n}}^{\text{dip}}$, and \mathbf{u} the unknown electric-surface-current density, $\hat{\mathbf{j}}_{\alpha;v_{m,n}}^{\text{rf}}$. Needed in the scheme is the adjoint operator of \mathbf{L} , \mathbf{L}^H , which is defined through the inner product, viz.

$$\langle \mathbf{L} \mathbf{u}, \mathbf{r} \rangle_{\mathbb{S}} = \langle \mathbf{u}, \mathbf{L}^H \mathbf{r} \rangle_{\mathbb{S}} , \quad (3.46)$$

and obtained via the L_2 norm of a vector \mathbf{v} , viz.

$$\begin{aligned} \|\mathbf{v}\|_{\mathbb{S}}^2 &= \langle \mathbf{v}, \mathbf{v} \rangle_{\mathbb{S}} \\ &= \sum_{m=-M+1}^{M-1} \sum_{n=-N+1}^N v_{1;v_{m,n}} v_{1;v_{m,n}}^* h_{v_3;v_n} \Delta v_1 \Delta v_3 \\ &\quad + \sum_{m=-M+1}^M \sum_{n=-N+1}^{N-1} v_{3;v_{m,n}} v_{3;v_{m,n}}^* h_{v_3;v_{n-\frac{1}{2}}} \Delta v_1 \Delta v_3 , \end{aligned} \quad (3.47)$$

where the “*” denotes that the complex conjugate is taken. Replacing $\mathcal{L}u$ in the left-hand side of equation (3.46) by its discretized counterpart as stated in equations (3.32)–(3.33), and using equation (3.47) to rewrite it such that the right-hand side of equation (3.46) is obtained, results in an expression for the adjoint operator \mathcal{L}^H applied on r , which reads

$$(\mathcal{L}^H r)_{1;v_{m'},n'} = \sum_{m=-M}^M \sum_{n=-N}^N \langle \hat{G} \rangle^* (v_{m,p,n} | v_{m'},n') R_{1;m,n} \Delta v_1 \Delta v_3, \quad (3.48)$$

$$\begin{aligned} (\mathcal{L}^H r)_{3;v_{m'},n'} = & \sum_{m=-M}^M \sum_{n=-N}^N \left[T_{2,3;v_{n'}} \frac{h_{v_3;p+1,n}}{2\Delta v_2} T_{2,2;v_{p+1,n}}^{-1} \langle \hat{G} \rangle^* (v_{m,p+1,n} | v_{m'},n') \right. \\ & - T_{2,3;v_{n'}} \frac{h_{v_3;p-1,n}}{2\Delta v_2} T_{2,2;v_{p-1,n}}^{-1} \langle \hat{G} \rangle^* (v_{m,p-1,n} | v_{m'},n') \\ & + T_{3,3;v_{n'}} \frac{h_{v_3;p+1,n}}{2\Delta v_2} T_{2,3;v_{p+1,n}}^{-1} \langle \hat{G} \rangle^* (v_{m,p+1,n} | v_{m'},n') \\ & \left. - T_{3,3;v_{n'}} \frac{h_{v_3;p-1,n}}{2\Delta v_2} T_{2,3;v_{p-1,n}}^{-1} \langle \hat{G} \rangle^* (v_{m,p-1,n} | v_{m'},n') \right] R_{2;m,n} \Delta v_1 \Delta v_3 \\ & + \sum_{m=-M}^M \sum_{n=-N}^N T_{2,3;v_{n'}} T_{3,2;v_{n'}}^{-1} \langle \hat{G} \rangle^* (v_{m,p,n} | v_{m'},n') R_{3;m,n} \Delta v_1 \Delta v_3 \\ & + \sum_{m=-M}^M \sum_{n=-N}^N T_{3,3;v_{n'}} T_{3,3;v_{n'}}^{-1} \langle \hat{G} \rangle^* (v_{m,p,n} | v_{m'},n') R_{3;m,n} \Delta v_1 \Delta v_3, \end{aligned} \quad (3.49)$$

where $R_{i;m,n}$ reads

$$\begin{aligned} R_{1;m,n} = & -(\hat{\gamma}^*)^2 \frac{1}{(s\hat{\epsilon})^*} h_{v_3;n-\frac{1}{2}} r_{1;m,n} \\ & + \frac{1}{(s\hat{\epsilon})^*} \frac{h_{v_3;n-\frac{1}{2}}}{(\Delta v_1)^2} (r_{1;m-1,n} - 2r_{1;m,n} + r_{1;m+1,n}) \\ & + \frac{1}{(s\hat{\epsilon})^*} \frac{1}{\Delta v_1 \Delta v_3} (r_{3;m,n-1} - r_{3;m+1,n-1} - r_{3;m,n} + r_{3;m+1,n}), \end{aligned} \quad (3.50)$$

$$\begin{aligned} R_{2;m,n} = & \frac{1}{(s\hat{\epsilon})^*} \frac{1}{2\Delta v_3} \left(\frac{1}{h_{v_2;n-\frac{1}{2}}} r_{1;m-1,n} - \frac{1}{h_{v_2;n-\frac{1}{2}}} r_{1;m,n} \right. \\ & \left. + \frac{1}{h_{v_2;n+\frac{1}{2}}} r_{1;m-1,n+1} - \frac{1}{h_{v_2;n+\frac{1}{2}}} r_{1;m,n+1} \right) \\ & + \frac{1}{(s\hat{\epsilon})^*} \frac{1}{2\Delta v_3} \frac{1}{h_{v_2;n} h_{v_3;n}} (r_{3;m,n-1} - r_{3;m,n+1}), \end{aligned} \quad (3.51)$$

Table 3.1: Conjugate gradient iteration scheme

$$\begin{aligned}
u_0 &= 0, \quad r_0 = f, \\
u_n &= u_{n-1} + \alpha_n w_n, \quad w_n = L^H r_{n-1} + \frac{\|L^H r_{n-1}\|_{\mathbb{S}}^2}{\|L^H r_{n-2}\|_{\mathbb{S}}^2} w_{n-1}, \\
r_n &= r_{n-1} - \alpha_n L w_n, \quad \alpha_n = \frac{\|L^H r_{n-1}\|_{\mathbb{S}}^2}{\|L w_n\|_{\mathbb{S}}^2},
\end{aligned}$$

$$\begin{aligned}
R_{3;m,n} &= -\frac{1}{(s\hat{\varepsilon})^*} (\hat{\gamma}^*)^2 h_{v_3;n} r_{3;m,n} \\
&+ \frac{1}{(s\hat{\varepsilon})^*} \frac{h_{v_2;n}}{\Delta v_1 \Delta v_3} \left(\frac{1}{h_{v_2;n-\frac{1}{2}}} r_{1;m-1,n} - \frac{1}{h_{v_2;n+\frac{1}{2}}} r_{1;m-1,n+1} \right. \\
&\quad \left. - \frac{1}{h_{v_2;n-\frac{1}{2}}} r_{1;m,n} + \frac{1}{h_{v_2;n+\frac{1}{2}}} r_{1;m,n+1} \right) \\
&+ \frac{1}{(s\hat{\varepsilon})^*} \frac{h_{v_2;n}}{(\Delta v_3)^2} \left(\frac{1}{h_{v_2;n-\frac{1}{2}} h_{v_3;n-\frac{1}{2}}} r_{3;m,n-1} - \frac{1}{h_{v_2;n+\frac{1}{2}} h_{v_3;n+\frac{1}{2}}} r_{3;m,n} \right. \\
&\quad \left. - \frac{1}{h_{v_2;n-\frac{1}{2}} h_{v_3;n-\frac{1}{2}}} r_{3;m,n} + \frac{1}{h_{v_2;n+\frac{1}{2}} h_{v_3;n+\frac{1}{2}}} r_{3;m,n+1} \right), \tag{3.52}
\end{aligned}$$

and where $r_{\alpha;m,n}$ satisfies

$$r_{1;m,n} = 0, \quad \forall \quad m \leq -M, \quad m \geq M, \quad n \leq -N, \quad n \geq N+1, \tag{3.53}$$

$$r_{3;m,n} = 0, \quad \forall \quad m \leq -M, \quad m \geq M+1, \quad n \leq -N, \quad n \geq N. \tag{3.54}$$

The scheme minimizes a normalized error ERR, defined as

$$\text{ERR} = \frac{\|r\|_{\mathbb{S}}}{\|f\|_{\mathbb{S}}}, \tag{3.55}$$

where the residual $\|r\|_{\mathbb{S}}$ is obtained from

$$\|r\|_{\mathbb{S}} = \|f - Lj\|_{\mathbb{S}}. \tag{3.56}$$

Once the normalized error ERR is small enough the iterative procedure is terminated. The applied conjugate gradient scheme is shown in table 3.1.

3.5 Numerical results for parabolically curved cylindrical reflector

In the previous sections, a method is presented to compute the radiation pattern for a dipole and a curved reflector. In this section this method is applied to a parabolically curved cylindrical reflector.

The reflector is described in a parabolical cylindrical coordinate system with parameters $v_i = \{v_1, v_2, v_3\}$, see appendix A. The Cartesian coordinate parameters $x_i = \{x_1, x_2, x_3\}$ are a function of these parameters v_i , viz.

$$\{x_1, x_2, x_3\} = \left\{ v_1, \frac{1}{2} (v_2^2 - v_3^2), v_2 v_3 \right\}, \quad (3.57)$$

resulting in the following Lamé's coefficients

$$h_{v_1} = 1, \quad (3.58)$$

and

$$h = h_{v_2} = h_{v_3} = (v_2^2 + v_3^2)^{\frac{1}{2}}. \quad (3.59)$$

In the numerical scheme the position vector $v_{m,p,n}$ satisfies

$$v_{m,p,n} = (m\Delta v_1, v_2^{\text{rf}} + p\Delta v_2, n\Delta v_3), \quad (3.60)$$

and the coordinate transformation matrices read

$$T_{k,l;v_{p,n}} = \begin{pmatrix} 1 & 0 & 0 \\ 0 & 0 & \frac{-n\Delta v_3}{h_{p,n}} \\ 0 & 0 & \frac{v_2^{\text{rf}} + p\Delta v_2}{h_{p,n}} \end{pmatrix}, \quad (3.61)$$

$$T_{j,k;v_{p,n}}^{-1} = \begin{pmatrix} 1 & 0 & 0 \\ 0 & \frac{v_2^{\text{rf}} + p\Delta v_2}{h_{p,n}} & \frac{v_3}{h_{p,n}} \\ 0 & \frac{-n\Delta v_3}{h_{p,n}} & \frac{v_2^{\text{rf}} + p\Delta v_2}{h_{p,n}} \end{pmatrix}. \quad (3.62)$$

We take as central frequency component 100 MHz, since this is in the center of the most interesting frequency range. As background medium we use a non-conducting medium with a relative permittivity similar to water,

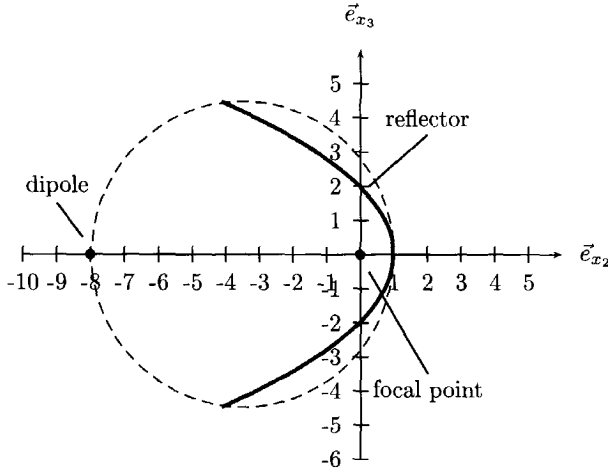


Figure 3.4: A parabolically curved reflector in the Cartesian coordinate system, for the domain $\mathbb{S} = \{\vec{v} \in \mathbb{R}^3 \mid -0.16 \text{ m} < v_1 < 0.16 \text{ m}, v_2 = 0.14 \text{ m}^{\frac{1}{2}}, -0.32 \text{ m}^{\frac{1}{2}} < v_3 < 0.32 \text{ m}^{\frac{1}{2}}\}$. Note that the axis units are cm.

$\epsilon_r = 80$. The complete antenna system must fit in a tool, that has a maximum inner diameter of 0.09 m. Positioning a half wavelength dipole as transmitter at maximum distance from the reflector, the domain \mathbb{L} of the dipole is represented

$$\mathbb{L} = \{\vec{v} \in \mathbb{R}^3 \mid -0.08 < v_1 < 0.08, v_2 = 0, v_3 = 0.4\} , \quad (3.63)$$

see figure 3.4. Since maximum shading and focusing effect is desirable, the reflector is taken as large as possible. Therefore, the length of the reflector is twice the length of the dipole, while v_2 and v_3 are chosen such that the area of the reflector becomes maximum. Consequently, the reflector domain becomes

$$\mathbb{S} = \{\vec{v} \in \mathbb{R}^3 \mid -0.16 < v_1 < 0.16, v_2 = 0.14, -0.32 < v_3 < 0.32\} . \quad (3.64)$$

The domain \mathbb{L} is divided in 20 cells in the \vec{e}_{v_1} -direction, while for the domain \mathbb{S} 26 cells in the \vec{e}_{v_1} -direction and 16 cells in the \vec{e}_{v_3} -direction are used. Decreasing the cell size, does not influence on the results significantly, since we now have approximately 18 elements per wavelength.

For this configuration, the iterative procedure to solve our integral equation terminates, once the converging normalized error satisfies the error criteria, $\text{ERR} \leq 0.01$, see figure 3.5. The computed electric-surface-current density is shown in figure 3.6. From this figure it is observed that the component of the electric-surface-current density normal to an edge vanishes at this edge. The tangential components however tend to large values, in fact theoretically they should grow to infinity, when we decrease the mesh size of the discretization.

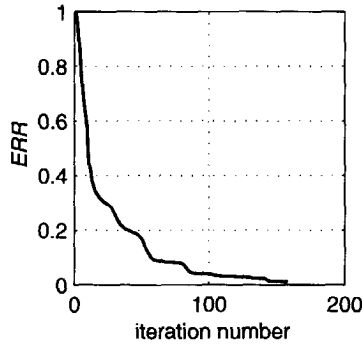


Figure 3.5: The convergent normalized error ERR as a function of the iteration number for the parabolically curved cylindrical reflector.

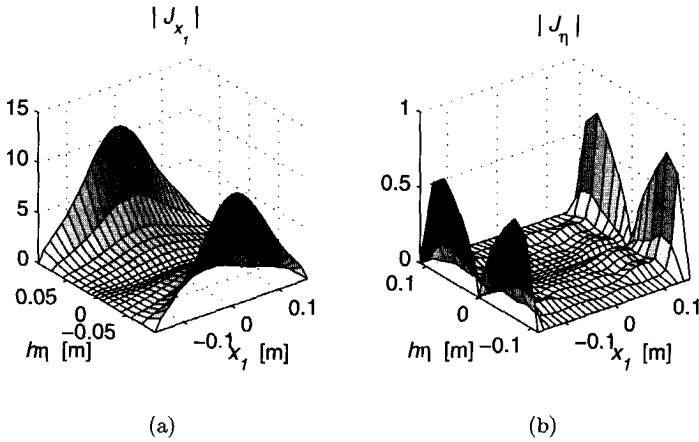


Figure 3.6: The two components of the computed electric-surface-current densities at the parabolically curved cylindrical reflector, a) \hat{J}_{x_1} and b) \hat{J}_{η} , where $x_1 = v_1$, $\zeta = v_2$ and $\eta = v_3$.

The incident electric wavefield in presence of the reflector is computed via the integral representation over the dipole and reflector domain. Their results are shown in the figures 3.7 (a) and (b) for the planes $x_1 = 0$ and $x_3 = 0$, respectively. Clearly visible is the disturbed omni-directional radiation pattern of the electric dipole due to the presence of the reflector. However, the aim is not only to obtain a directional radiation pattern but also to gain penetration in the subsurface by focusing the emitted energy. Therefore, we define a gain

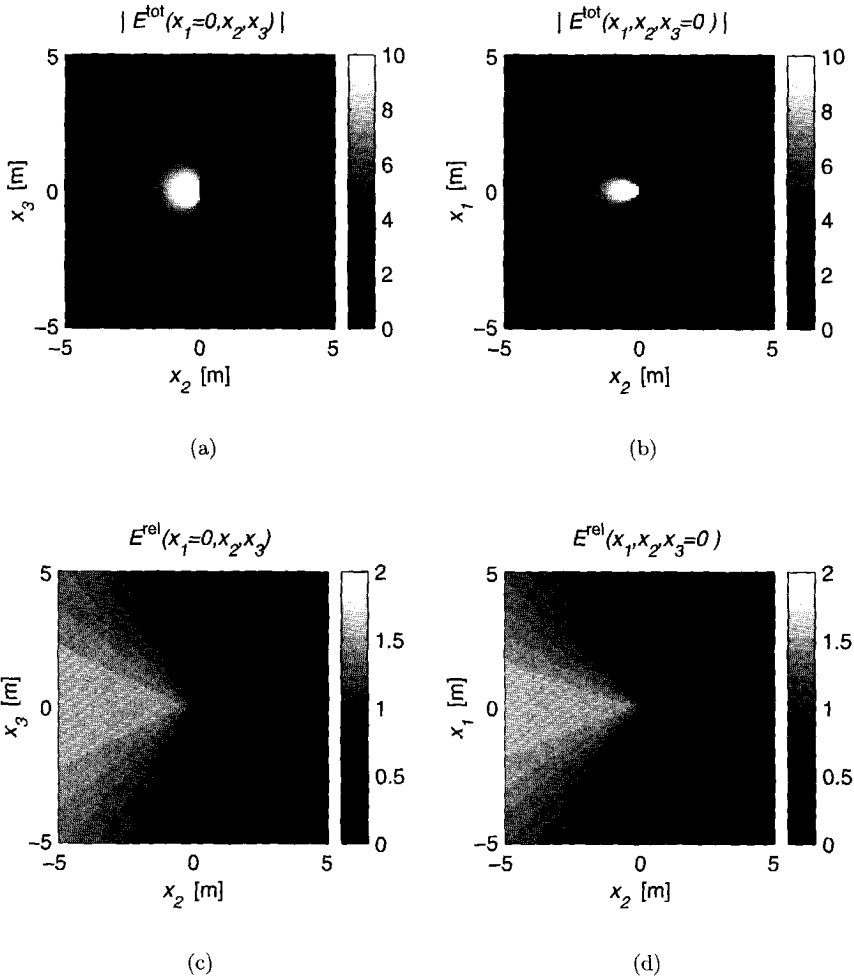


Figure 3.7: The absolute values of the incident electric wavefield for the parabolic reflector, $|\hat{E}_i^{\text{inc}}(\vec{x})|$, in the planes (a) $x_1 = 0$ and (b) $x_3 = 0$, and their normalized values, $\hat{E}^{\text{rel}}(\vec{x}) = |\hat{E}_i^{\text{inc}}(\vec{x})| / |\hat{E}_i^{\text{dip}}(\vec{x})|$, in the planes (c) $x_1 = 0$ and (d) $x_3 = 0$.

factor $\hat{E}^{\text{rel}}(\vec{x})$ which reads

$$\hat{E}^{\text{rel}}(\vec{x}) = \frac{|\hat{E}_{x_i}^{\text{inc}}(\vec{x})|}{|\hat{E}_{x_i}^{\text{dip}}(\vec{x})|}. \quad (3.65)$$

In figures 3.7(c)-(d) these factors for are shown the planes $x_1 = 0$ and $x_3 = 0$.

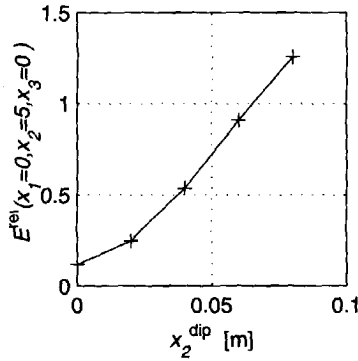


Figure 3.8: The gain factor $\hat{E}^{\text{rel}}(x_1 = 0, x_2 = 5, x_3 = 0)$ as a function of the dipole position $(0, x_2^{\text{dip}}, 0)$ near a parabolic reflector.

It is interesting to investigate the effect of moving the dipole towards the focal point. If ray theory could be applied to our electromagnetic case, an increase of $|\hat{E}^{\text{inc}}(\vec{x})|$ is expected in front of the opening. Therefore, the gain factor $\hat{E}^{\text{rel}}(x_1 = 0, x_2, x_3 = 0)$ is computed for various positions of the dipole, starting in the focal point and moving 0.08 m to the position used previously. The results of these computations are shown in figure 3.8. It is seen that moving the dipole towards the focal point results in a strong decrease of focusing effect.

The results presented here, show that it is indeed possible to “focus” the radiation pattern of an electric dipole with a cylindrical parabolically curved reflector. On the contrary to ray theory, an improvement in focusing effect in the plane $x_1 = 0$ is obtained by moving the dipole out of the focal point and away from the reflector. Therefore, it is interesting to compute the radiation pattern in case a circular curvature is chosen, since this a limiting case for the largest distance between reflector and dipole.

3.6 Numerical results for circularly curved cylindrical reflector

In the previous section we showed how a directional radiation pattern is obtained with an electric dipole and a parabolically curved cylindrical reflector. Furthermore we showed that the best focusing is obtained by positioning the dipole at maximum distance from the reflector. The distance to each point on the reflector is maximum, in case the reflector is curved circularly. Consequently, we compute the radiation pattern for a circularly curved cylindrical

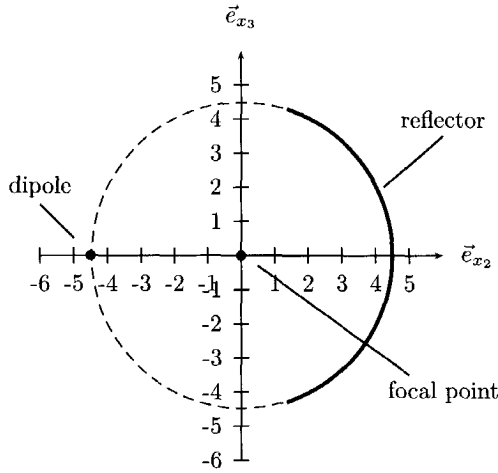


Figure 3.9: Circularly curved reflector in the Cartesian coordinate system with domain $\mathbb{S} = \{\vec{v} \in \mathbb{R}^3 \mid -0.16 \text{ m} < v_1 < 0.16 \text{ m}, v_2 = 0.045 \text{ m}, -1.27 < v_3 < 1.27\}$. Note that the axis units are cm.

reflector.

In a circularly curved coordinate system a point in space is denoted by the parameters v_i , for $i = \{1, 2, 3\}$ and the Cartesian coordinates x_i are a function of these parameters v_i , viz.

$$\{x_1, x_2, x_3\} = \{v_1, v_2 \cos(v_3), v_2 \sin(v_3)\}, \quad (3.66)$$

see figure 3.9. Therefore, the Lamé coefficients are given by

$$h_{v_1} = h_{v_2} = 1, \quad h_{v_3} = v_2. \quad (3.67)$$

In the numerical scheme a position in space is written as $v_{m,n,p}$ which satisfies

$$v_{m,p,n} = (m\Delta v_1, v_2^{\text{ref}} + p\Delta v_2, n\Delta v_3) \quad (3.68)$$

and the coordinate transformation matrices become

$$T_{k,l,v_n} = \begin{pmatrix} 1 & 0 & 0 \\ 0 & 0 & -\sin(n\Delta v_3) \\ 0 & 0 & \cos(n\Delta v_3) \end{pmatrix}, \quad (3.69)$$

$$T_{j,k,v_n}^{-1} = \begin{pmatrix} 1 & 0 & 0 \\ 0 & \cos(n\Delta v_3) & \sin(n\Delta v_3) \\ 0 & -\sin(n\Delta v_3) & \cos(n\Delta v_3) \end{pmatrix}. \quad (3.70)$$

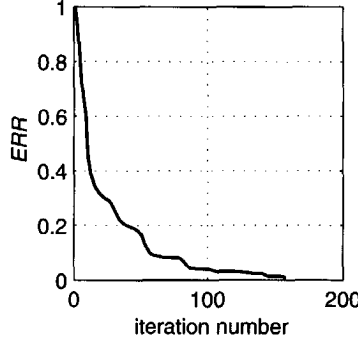


Figure 3.10: The convergent normalized error ERR as a function of the iteration number for the circularly curved cylindrical reflector.

The factorized gradient-divergence operator as stated in equations (3.38)-(3.40) simplifies for the circularly curved reflector into

$$\begin{aligned}\hat{B}_{j';v_m,n}^{\text{rfl}} &= D_{v_{j';v_m,p,n}}^N \hat{A}_{j';v_m,p,n}^{\text{rfl}} \\ &= \begin{pmatrix} \hat{A}_{1;v_m,0,n}^{\text{rfl}} \\ \frac{1}{2\Delta v_2} (v_{2;+1} \hat{A}_{2;v_m,1,n}^{\text{rfl}} - v_{2;-1} \hat{A}_{2;v_m,-1,n}^{\text{rfl}}) \\ \hat{A}_{3;v_m,0,n}^{\text{rfl}} \end{pmatrix}, \quad (3.71)\end{aligned}$$

$$\begin{aligned}D_{v_{1j';v_m,n}}^T \hat{B}_{j';v_m,n}^{\text{rfl}} &= \frac{1}{(\Delta v_1)^2} (\hat{B}_{1;v_{m+1},n}^{\text{rfl}} - 2\hat{B}_{1;v_m,n}^{\text{rfl}} + \hat{B}_{1;v_{m-1},n}^{\text{rfl}}) \\ &\quad + \frac{1}{v_2^{\text{rfl}}} \frac{1}{2\Delta v_1} (\hat{B}_{2;v_{m+1},n}^{\text{rfl}} - \hat{B}_{2;v_m,n}^{\text{rfl}} + \hat{B}_{2;v_{m+1},n-1}^{\text{rfl}} - \hat{B}_{2;v_m,n-1}^{\text{rfl}}) \\ &\quad + \frac{1}{v_2^{\text{rfl}}} \frac{1}{\Delta v_1 \Delta v_3} (\hat{B}_{3;v_{m+1},n}^{\text{rfl}} - \hat{B}_{3;v_{m+1},n-1}^{\text{rfl}} - \hat{B}_{3;v_m,n}^{\text{rfl}} + \hat{B}_{3;v_m,n-1}^{\text{rfl}}), \quad (3.72)\end{aligned}$$

and

$$\begin{aligned}D_{v_{3j';v_m,n}}^T \hat{B}_{j';v_m,n}^{\text{rfl}} &= \frac{1}{v_2^{\text{rfl}}} \frac{1}{\Delta v_1 \Delta v_3} (\hat{B}_{1;v_{m,n+1}}^{\text{rfl}} - \hat{B}_{1;v_{m-1},n+1}^{\text{rfl}} - \hat{B}_{1;v_m,n}^{\text{rfl}} + \hat{B}_{1;v_{m-1},n}^{\text{rfl}}) \\ &\quad + \frac{1}{(v_2^{\text{rfl}})^2} \frac{1}{2\Delta v_3} (\hat{B}_{2;v_{m,n+1}}^{\text{rfl}} - \hat{B}_{2;v_m,n-1}^{\text{rfl}}) \\ &\quad + \frac{1}{(v_2^{\text{rfl}})^2} \frac{1}{(\Delta v_3)^2} (\hat{B}_{3;v_{m,n+1}}^{\text{rfl}} - 2\hat{B}_{3;v_m,n}^{\text{rfl}} + \hat{B}_{3;v_{m,n-1}}^{\text{rfl}}). \quad (3.73)\end{aligned}$$

As stated before, computations are carried out for the 100 MHz frequency component while the system is positioned in a non-conducting medium with relative

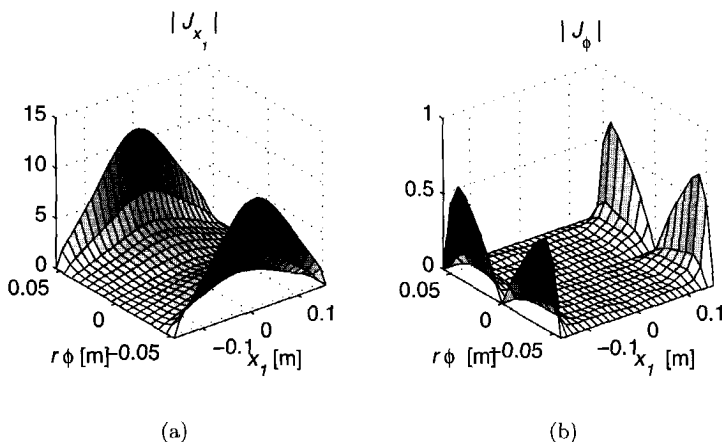


Figure 3.11: The computed electric-surface-current densities at the circularly curved cylindrical reflector, a) \hat{J}_{x_1} and b) \hat{J}_ϕ , where $x_1 = v_1$, $r = v_2$ and $\phi = v_3$.

permittivity $\varepsilon_r = 80$. Positioning a half wavelength electric dipole opposite to the reflector, the dipole domain \mathbb{L} is represented by

$$\mathbb{L} = \{\vec{v} \in \mathbb{R}^3 \mid -0.08 < v_1 < 0.08, v_2 = 0.045, v_3 = \frac{1}{2}\pi\}, \quad (3.74)$$

see figure 3.9. The reflector is taken twice as long in the \vec{e}_{v_1} -direction, to improve its shading effect. The reflector domain \mathbb{S} is given by

$$\mathbb{S} = \{\vec{v} \in \mathbb{R}^3 \mid -0.16 < v_1 < 0.16, v_2 = 0.045, -1.27 < v_3 < 1.27\}. \quad (3.75)$$

The domain \mathbb{L} is divided in 20 cells in the \vec{e}_{v_1} -direction, while for the domain \mathbb{S} 26 cells in the \vec{e}_{v_1} -direction and 16 cells in the \vec{e}_{v_3} -direction are used. For this configuration, the iterative procedure to solve our integral equation is terminated once the converging normalized error satisfies the error criteria, $\text{ERR} \leq 0.01$, see figure 3.10. The obtained electric-surface-current density is shown in figure 3.11. From this figure it is observed that the components of the electric-surface-current density normal to an edge vanish at this edge. The tangential component however tend to large values, in fact theoretically they should grow to infinity when refining the mesh size. From these electric-surface-current densities the incident electric wavefield is obtained via an integral representation over the dipole and reflector domain. These results are shown in figures 3.12 (a) and (b), for the planes $x_1 = 0$ and $x_3 = 0$, respectively. The effect of the reflector in the disturbance of the omni-directional radiation pattern is clearly visible. Another important effect is the increase in penetration by

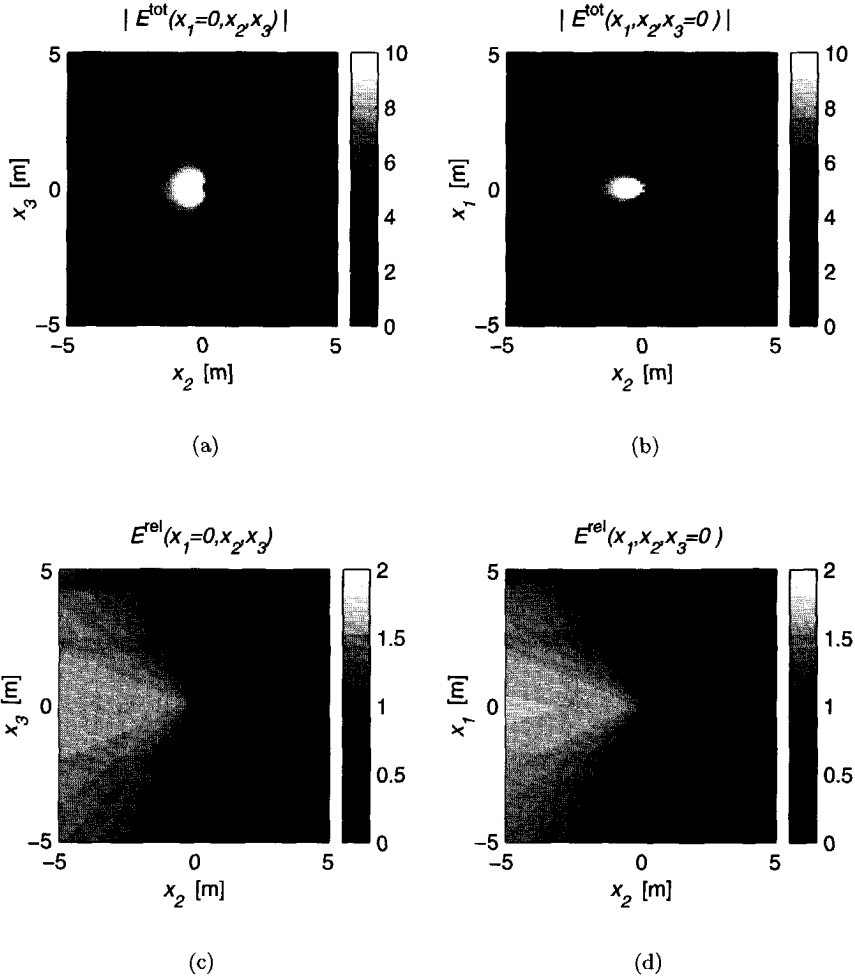


Figure 3.12: The absolute values of the incident electric wavefield for the circular cylindrical reflector, $|\hat{E}_i^{\text{inc}}(\vec{x})|$, in the planes (a) $x_1 = 0$ and (b) $x_3 = 0$ and their normalized values, $\hat{E}_i^{\text{rel}}(\vec{x}) = |\hat{E}_i^{\text{inc}}(\vec{x})| / |\hat{E}_i^{\text{dip}}(\vec{x})|$, in the planes (c) $x_1 = 0$ and (d) $x_3 = 0$.

focusing the energy. Hence, it is interesting to compute the gain factor $\hat{E}^{\text{rel}}(\vec{x})$,

$$\hat{E}^{\text{rel}}(\vec{x}) = \frac{|\hat{E}_i^{\text{inc}}(\vec{x})|}{|\hat{E}_i^{\text{dip}}(\vec{x})|}, \quad (3.76)$$

as shown in figures 3.12 (c) and (d) for the two planes $x_1 = 0$ and $x_3 = 0$.

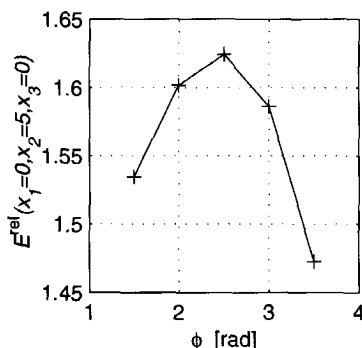


Figure 3.13: The gain factor $\hat{E}^{\text{rel}}(x_1 = 0, x_2 = 5, x_3 = 0)$ as a function of the reflector angle, where $\phi = v_3$.

The effect of the size of the reflector in the angular direction is shown in figure 3.13. For various angular sizes, the gain factor is computed at the position $\vec{x} = (0, 5, 0)$. It is clearly visible that the gain factor reaches its maximum once the reflector is curved over 2.5 rad (143°).

3.7 Experimental verification

Based on the design of the 143° circularly curved cylindrical reflector, a prototype was built¹. The complete tool is shown in figure 3.15. The tool has a length of 4.42 m and a diameter of 0.16 m. At the top and the bottom, wheel-blocks are constructed to centralize the system in a borehole. Below the upper wheel-block, the electronics for measuring the orientation and the depth of the tool are positioned. In addition, this part contains the mechanics to rotate the antenna system inside the tool. In between this part and the top of the lower wheel-block, the rotating antenna system is positioned, including the electronics for creating an electric-current pulse for the transmitter and an A/D-converter for digitizing the signal measured by the receiver. The tool is connected with a pc at the surface, to control the system and to store the data measured.

The radiation pattern of the antenna system was measured under water. An (unknown) electric-voltage pulse was put across the port of the dipole. At a radial distance of 0.3 m in the plane $x_1 = 0$ a receiver was positioned parallel to the rotating transmitting system. As receiving system, the PULSE EKKO 100 system of SENSORS & SOFTWARE with the 200 MHz dipole antenna was

¹The prototype was built in cooperation with the National Aerospace Laboratory (NLR) and TNO Physics and Electronics Laboratory (TNO-FEL), under the supervision of R. van Waard from T&A Survey.

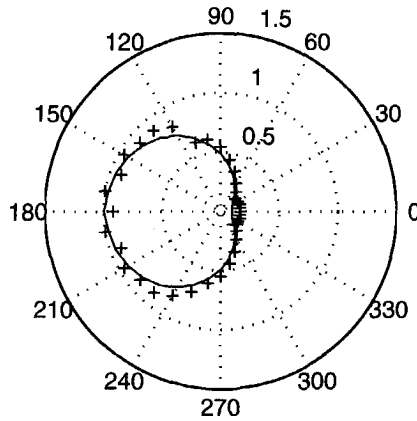


Figure 3.14: The measured (crosses) and the computed (solid line) 100 MHz components of the incident electric wavefield, $|\hat{E}_i^{\text{inc}}(\vec{x})|$, at a radial distance of 0.3 m in the plane $x_1 = 0$.

used. In figure 3.14 the results are shown. Both 100 MHz components of the received signal and the computed radiation pattern are given. The curves are normalized by putting their maximum values to unity. From this figure it can be concluded that both results are in excellent agreement with each other.

3.8 Conclusion

The results obtained in this chapter show that it is possible to build a directional borehole radar system. However, given the spatial limitations such as the maximum diameter of 0.09 m and desired central frequency component of 100 MHz, it is not obvious that a directional radiation pattern with an electric wavefield can be obtained. Especially, when one realizes that the wavelength in air, corresponding to the central frequency, is approximately thirty times larger than the diameter of the borehole (or the antenna system). Nevertheless, we succeeded in designing such a system, by positioning an electric dipole next to a metal reflector. In order to shorten the wavelength, a medium with a high relative permittivity is used (water). In the optimum configuration the reflector is circularly curved over approximately 143° . Parabolically curved reflectors, unlike in optics, give poorer focussing.

Now we have shown it is possible to “focus” the radiation pattern, we need to develop an imaging algorithm which enables us to obtain a three-dimensional image of the surrounding. This is done in the next chapter. As shown in chap-

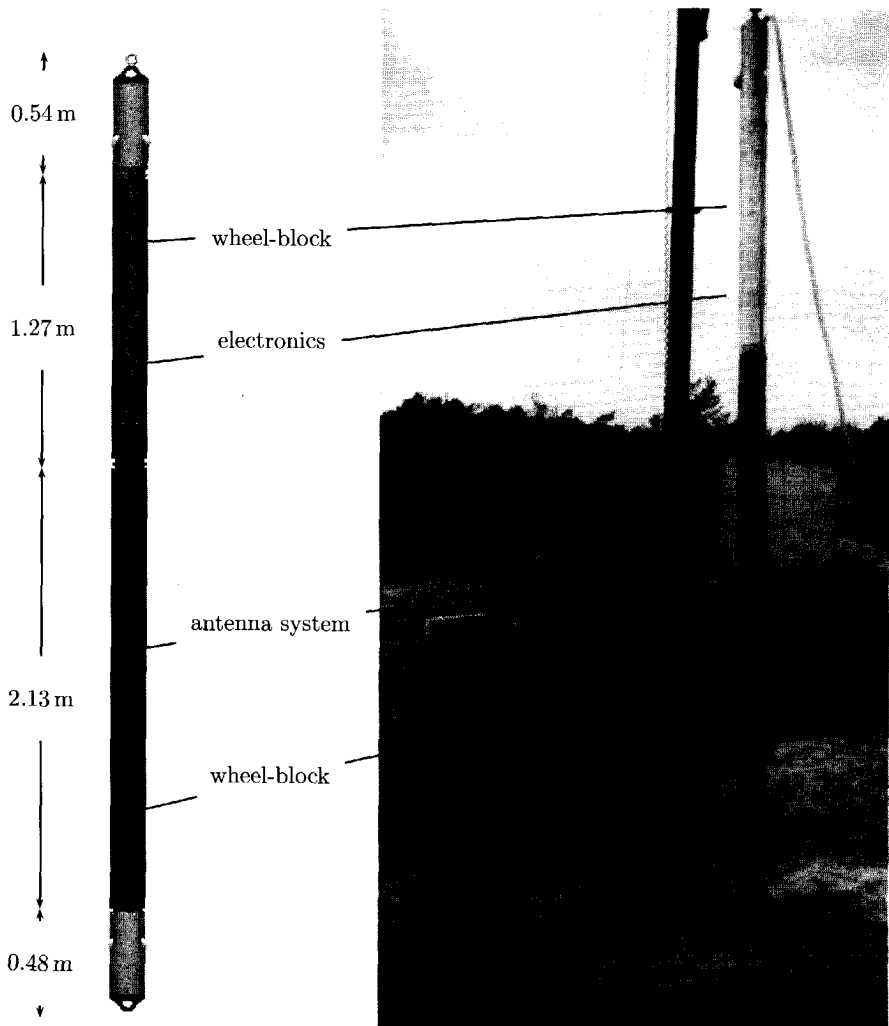


Figure 3.15: The prototype antenna system, on the left the design and on the right in action to detect unexploded ordnance in the subsurface.

ter 2, it is important to have a good knowledge of the properties of the system in order to understand the wavefield scattered at the objects and observed by the antenna system. Especially, since the scattered wavefield depends on the total wavefield which includes the incident wavefield from the antenna system. Hence, we will use the results obtained in this chapter in the next chapter.

Chapter 4

Imaging

In the previous chapter we show the design of the antennas for a borehole radar system which has directional sensitivity properties. The starting point for this design is made in chapter 2. In this chapter, we consider the antenna system as a black box. We show that changes in the subsurface are observed by changes in the measured voltage at the receiver. Next, we develop an inversion algorithm to compute a three-dimensional image of the subsurface using the measured voltage. In this inversion scheme we use the results obtained in the previous chapter. Note that we start with the results obtained in chapter 2. Further note that the formulation of the problem is carried out in a Cartesian reference frame. Once the algorithm is utilized, a change to a circular cylindrical coordinate system is made.

4.1 Change in impedance due to scattering objects

In figure 4.1 the directional borehole radar system is shown. The system is positioned in the Cartesian coordinate system, in which a spatial position is denoted by the vector $\vec{x} = x_i$ for $i = \{1, 2, 3\}$. The tool is embedded in a homogeneous background medium with complex permittivity $\hat{\epsilon}^{bg}$, hence

$$\hat{\epsilon}^{bg} = \epsilon_0 \epsilon_r + \frac{\sigma}{s}, \quad (4.1)$$

where $\epsilon_0 \epsilon_r$ is the permittivity of the medium and σ the conductivity. Furthermore, the medium is nonmagnetic susceptible. The symbol $\hat{\cdot}$ on top of a given

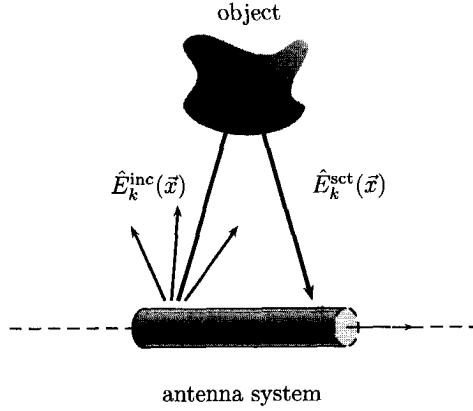


Figure 4.1: The borehole radar system radiates a wavefield $\hat{E}_k^{\text{inc}}(\vec{x})$, which scatters at the object, $\hat{E}_k^{\text{sct}}(\vec{x})$.

quantity or parameter denotes that it is defined in the temporal Laplace domain with Laplace parameter s . Frequency domain results are obtained by taking the limit

$$s \rightarrow -i\omega, \quad (4.2)$$

where $\omega = 2\pi f$, in which f is the temporal frequency.

Since the system is oriented in the \vec{e}_1 -direction, a directional radiation pattern is obtained in the (x_2, x_3) -plane. From chapter 2 we know that the total electric wavefield due to the presence of an object at \mathbb{D}^{sct} reads

$$\hat{E}_k^{\text{tot}}(\vec{x}) = \hat{E}_k^{\text{inc}}(\vec{x}) + \hat{E}_k^{\text{sct}}(\vec{x}), \quad (4.3)$$

where $\hat{E}_k^{\text{inc}}(\vec{x})$ is the incident wavefield from the antenna system into the subsurface, and where $\hat{E}_k^{\text{sct}}(\vec{x})$ denotes the scattered wavefield. The scattered wavefield satisfies, see equation (2.35),

$$\hat{E}_k^{\text{sct}}(\vec{x}) = \int_{\vec{x}' \in \mathbb{D}^{\text{sct}}} s \left(\hat{\varepsilon}^{\text{sct}}(\vec{x}') - \hat{\varepsilon}^{\text{bg}} \right) \hat{\mathcal{G}}_{k,l}^{E,J}(\vec{x}|\vec{x}') \hat{E}_l^{\text{tot}}(\vec{x}') dV(\vec{x}'), \quad (4.4)$$

where $\hat{\mathcal{G}}_{k,l}^{E,J}(\vec{x}|\vec{x}')$ is the electric-field/electric-current Green's tensor, which reads

$$\hat{\mathcal{G}}_{k,l}^{E,J}(\vec{x}|\vec{x}') = \frac{1}{s\hat{\varepsilon}} \left(-\hat{\gamma}^2 I_{k,l} + \partial_k \partial_l \right) \hat{G}(\vec{x}|\vec{x}'), \quad (4.5)$$

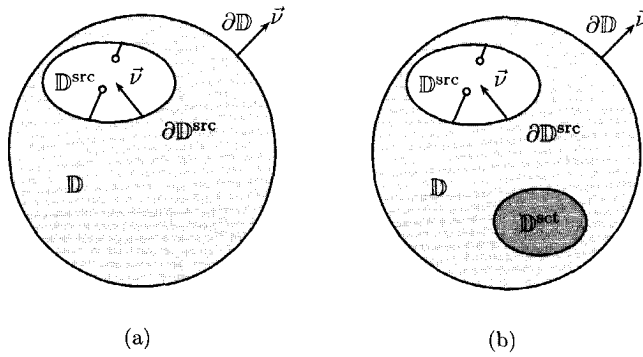


Figure 4.2: Two states of the same spatial domain \mathbb{D} , with an inaccessible volume action antenna source domain $\mathbb{D}^{\text{src}} \subset \mathbb{D}$ containing two ports. The surface of the source domain encloses a receiving and transmitting antenna. In state A (a) the electromagnetic properties are $\hat{\epsilon}^A(\vec{x}) = \hat{\epsilon}^{\text{bg}}$, $\mu^A = \mu_0$ and state B (b) has the same background medium and a scattering domain $\mathbb{D}^{\text{sct}} \subset \mathbb{D}$, with $\hat{\epsilon}^B(\vec{x}) = \hat{\epsilon}^{\text{sct}}(\vec{x})$, $\mu^B = \mu_0$.

where $\hat{\gamma}$ satisfies

$$\hat{\gamma}^2 = s^2 \hat{\epsilon} \mu_0, \quad (4.6)$$

while $I_{l,k}$ is the symmetric unit tensor and $\hat{G}(\vec{x}|\vec{x}')$ the scalar form of the Green function, viz.

$$\hat{G}(\vec{x}|\vec{x}') = \frac{\exp(-\hat{\gamma}|\vec{x} - \vec{x}'|)}{4\pi|\vec{x} - \vec{x}'|}, \quad (4.7)$$

see equations (2.24)-(2.27) and (2.35). By neglecting internal scattering within the scatterer, the Born approximation is applied and we approximate equation (4.4) by

$$\hat{E}_k^{\text{sct}}(\vec{x}) = \int_{\vec{x}' \in \mathbb{D}^{\text{sct}}} s \delta \hat{\epsilon}(\vec{x}') \hat{\mathcal{G}}_{k,l}^{E,J}(\vec{x}|\vec{x}') \hat{E}_l^{\text{inc}}(\vec{x}') dV(\vec{x}'), \quad (4.8)$$

where

$$\delta \hat{\epsilon}(\vec{x}') = \hat{\epsilon}^{\text{sct}}(\vec{x}') - \hat{\epsilon}^{\text{bg}}. \quad (4.9)$$

However, with our system we do not measure the scattered fields themselves, but we measure changes in impedance caused by changes in the medium. By using reciprocity, see section 2.3, an expression is obtained which interrelates the measured impedance with the changes in medium parameters.

Table 4.1: Description of the two states of the spatial domain \mathbb{D}

state A	state B
$\hat{E}_k^A = \hat{E}_k^{\text{inc}}(\vec{x}) \quad \forall \vec{x} \in \mathbb{D}$	$\hat{E}_k^B = \hat{E}_k^{\text{tot}}(\vec{x}) \quad \forall \vec{x} \in \mathbb{D}$
$\hat{H}_j^A = \hat{H}_j^{\text{inc}}(\vec{x}) \quad \forall \vec{x} \in \mathbb{D}$	$\hat{H}_j^B = \hat{H}_j^{\text{tot}}(\vec{x}) \quad \forall \vec{x} \in \mathbb{D}$
$\hat{J}_k^A = 0 \quad \forall \vec{x} \in \mathbb{D}$	$\hat{J}_k^B = 0 \quad \forall \vec{x} \in \mathbb{L}$
$\hat{K}_j^A = 0 \quad \forall \vec{x} \in \mathbb{D}$	$\hat{K}_j^B = 0 \quad \forall \vec{x} \in \mathbb{D}$
$\hat{\epsilon}^A = \begin{cases} \hat{\epsilon}^{\text{bg}} & \forall \vec{x} \in \mathbb{D}' \\ \hat{\epsilon}^{\text{src}}(\vec{x}) & \forall \vec{x} \in \partial\mathbb{D}^{\text{src}} \end{cases}$	$\hat{\epsilon}^B = \begin{cases} \hat{\epsilon}^{\text{bg}} & \forall \vec{x} \in \mathbb{D}' \\ \hat{\epsilon}^{\text{sct}}(\vec{x}) & \forall \vec{x} \in \mathbb{D}^{\text{sct}} \\ \hat{\epsilon}^{\text{src}}(\vec{x}) & \forall \vec{x} \in \partial\mathbb{D}^{\text{src}} \end{cases}$
$\hat{\mu}^A = \mu_0 \quad \forall \vec{x} \in \mathbb{D}$	$\hat{\mu}^B = \mu_0 \quad \forall \vec{x} \in \mathbb{D}$
$\mathbb{D}^{\text{sct}} = \emptyset$	$\mathbb{D}' = \mathbb{D} \setminus \mathbb{D}^{\text{sct}}$

The reciprocity theorem interrelates two separable states A and B , which can occur in the same spatial domain. In both states we have a spatial domain \mathbb{D} , with background medium parameters $\hat{\epsilon}^{\text{bg}}$ and μ_0 , enclosing an inaccessible volume domain \mathbb{D}^{src} in which the antenna system is positioned, see figure 4.2. In state A the electromagnetic wavefields are denoted by $\{\hat{E}_k^{\text{inc}}(\vec{x}), \hat{H}_j^{\text{inc}}(\vec{x})\}$. Those are the wavefields in absence of scattering objects. In state B we have $\{\hat{E}_k^{\text{tot}}(\vec{x}), \hat{H}_j^{\text{tot}}(\vec{x})\}$, where the changes in the wavefields in comparison with state A , are caused by the presence of a scatterer in \mathbb{D}^{sct} with complex permittivity $\hat{\epsilon}^{\text{sct}}(\vec{x})$, see table 4.1. Consequently, the frequency domain reciprocity theorem satisfies

$$\begin{aligned}
& \epsilon_{m,k,p} \int_{\vec{x} \in \partial\mathbb{D}} \nu_m \left(\hat{E}_k^{\text{inc}}(\vec{x}) \hat{H}_p^{\text{tot}}(\vec{x}) - \hat{E}_k^{\text{tot}}(\vec{x}) \hat{H}_p^{\text{inc}}(\vec{x}) \right) dA(\vec{x}) \\
& + \epsilon_{m,k,p} \int_{\vec{x} \in \partial\mathbb{D}^{\text{src}}} \nu_m \left(\hat{E}_k^{\text{inc}}(\vec{x}) \hat{H}_p^{\text{tot}}(\vec{x}) - \hat{E}_k^{\text{tot}}(\vec{x}) \hat{H}_p^{\text{inc}}(\vec{x}) \right) dA(\vec{x}) \\
& = - \int_{\vec{x} \in \mathbb{D}^{\text{sct}}} s \delta\hat{\epsilon}(\vec{x}) \hat{E}_k^{\text{inc}}(\vec{x}) \hat{E}_k^{\text{tot}}(\vec{x}) dV(\vec{x}) . \quad (4.10)
\end{aligned}$$

The first term on the left-hand side of equation (4.10) vanishes when one lets a point on the boundary surface $\partial\mathbb{D}$ tend to infinity, since in both states the media at infinity are homogeneous and source-free. The second surface integral, over the boundary of the inaccessible source domain \mathbb{D}^{src} , is discussed below.

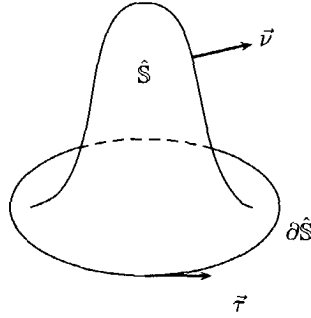


Figure 4.3: The bounded surface $\hat{\mathbb{S}}$ with boundary $\partial\hat{\mathbb{S}}$ and unit vectors $\vec{\tau}$ and $\vec{\nu}$.

The Maxwell equation,

$$\epsilon_{i,j,k} \partial_j \hat{E}_k(\vec{x}) + s\mu_0 \hat{H}_i(\vec{x}) = -\hat{K}_i^{\text{ext}}(\vec{x}) \quad (4.11)$$

on a magnetic-source-current-free boundary is in the low-frequency range approximated by

$$\epsilon_{i,j,k} \partial_j \hat{E}_k(\vec{x}) = 0. \quad (4.12)$$

Consequently, the electric wavefield satisfies

$$\hat{E}_k(\vec{x}) = -\partial_k \hat{\Psi}(\vec{x}), \quad (4.13)$$

with $\hat{\Psi}(\vec{x})$ the electric potential. Applying this result in the second term in the left-hand side of equation (4.10) we obtain for this term

$$\begin{aligned} \epsilon_{m,k,j} \int_{\vec{x} \in \partial\mathbb{D}^{\text{src}}} \nu_m \left(\hat{E}_k^{\text{inc}}(\vec{x}) \hat{H}_j^{\text{tot}}(\vec{x}) - \hat{E}_k^{\text{tot}}(\vec{x}) \hat{H}_j^{\text{inc}}(\vec{x}) \right) dA(\vec{x}) \\ = \epsilon_{m,k,j} \int_{\vec{x} \in \partial\mathbb{D}^{\text{src}}} \nu_m \left[-\partial_k \left(\hat{\Psi}^{\text{inc}}(\vec{x}) \hat{H}_j^{\text{tot}}(\vec{x}) \right) + \hat{\Psi}^{\text{inc}}(\vec{x}) \partial_k \hat{H}_j^{\text{tot}}(\vec{x}) \right. \\ \left. + \partial_k \left(\hat{\Psi}^{\text{tot}}(\vec{x}) \hat{H}_j^{\text{inc}}(\vec{x}) \right) - \hat{\Psi}^{\text{tot}}(\vec{x}) \partial_k \hat{H}_j^{\text{inc}}(\vec{x}) \right] dA(\vec{x}). \quad (4.14) \end{aligned}$$

The first and the fourth term in the right-hand side of equation (4.14) are rewritten using Stokes integral theorem. This theorem states that a continuous differentiable tensor $F_{m_1, m_2, \dots, m_K}(\vec{x})$, defined on a bounded surface $\hat{\mathbb{S}}$, see figure 4.3, satisfies

$$\oint_{\vec{x} \in \partial\hat{\mathbb{S}}} \tau_p F_{m_1, m_2, \dots, m_K}(\vec{x}) dL(\vec{x}) = \int_{\vec{x} \in \hat{\mathbb{S}}} \epsilon_{p,q,r} \nu_q \partial_r F_{m_1, m_2, \dots, m_K}(\vec{x}) dA(\vec{x}), \quad (4.15)$$

where $\vec{\nu}$ is the unit vector normal to the surface $\hat{\mathbb{S}}$. The orientation of $\vec{\nu}$ is in the direction of the displacement of a screw being turned in the direction of $\vec{\tau}$ along $\partial\hat{\mathbb{S}}$. Therefore, the contribution from the first and the fourth term in equation (4.14) equals zero, viz.

$$\epsilon_{m,k,p} \int_{\vec{x} \in \partial\mathbb{D}^{\text{src}}} \nu_m \partial_k \left(\hat{\Psi}^{\text{inc,tot}}(\vec{x}) \hat{H}_p^{\text{tot,inc}}(\vec{x}) \right) dA(\vec{x}) = 0, \quad (4.16)$$

where we assume $\hat{\Psi}^{\text{inc,tot}}(\vec{x}) \hat{H}_p^{\text{tot,inc}}(\vec{x})$ to be continuous differentiable on $\hat{\mathbb{S}}$. Therefore, equation (4.14) is written as

$$\begin{aligned} \epsilon_{m,k,p} \int_{\vec{x} \in \partial\mathbb{D}^{\text{src}}} \nu_m \left(\hat{E}_k^{\text{inc}}(\vec{x}) \hat{H}_p^{\text{tot}}(\vec{x}) - \hat{E}_k^{\text{tot}}(\vec{x}) \hat{H}_p^{\text{inc}}(\vec{x}) \right) dA(\vec{x}) \\ = \int_{\vec{x} \in \partial\mathbb{D}^{\text{src}}} \nu_m \left[\hat{\Psi}^{\text{inc}}(\vec{x}) s \hat{\varepsilon}^{\text{src}}(\vec{x}) \hat{E}_m^{\text{tot}}(\vec{x}) - \hat{\Psi}^{\text{tot}}(\vec{x}) s \hat{\varepsilon}^{\text{src}}(\vec{x}) \hat{E}_m^{\text{inc}}(\vec{x}) \right] dA(\vec{x}), \end{aligned} \quad (4.17)$$

where we used Maxwell equations. Next, we combine the electromagnetic boundary conditions with the constitutive relations in the right-hand side of equation (4.17). By applying the low-frequency approximation, we assume the Maxwell current density $\hat{J}_m(\vec{x}) + s \hat{D}_m(\vec{x})$ to be concentrated in the electric-current density $\hat{J}_m(\vec{x})$ at the conductors that form the ports of the antenna system. Assuming there are a number of ports, $\mathcal{N} = 1, 2, \dots$, we obtain

$$\begin{aligned} \int_{\vec{x} \in \partial\mathbb{D}^{\text{src}}} \nu_m \left[\hat{\Psi}^{\text{inc}}(\vec{x}) s \hat{\varepsilon}^{\text{src}}(\vec{x}) \hat{E}_m^{\text{tot}}(\vec{x}) - \hat{\Psi}^{\text{tot}}(\vec{x}) s \hat{\varepsilon}^{\text{src}}(\vec{x}) \hat{E}_m^{\text{inc}}(\vec{x}) \right] dA(\vec{x}) \\ = \sum_{\mathcal{N}} \int_{\vec{x} \in \mathbb{A}_{\mathcal{N}}} \nu_m \left[\hat{\Psi}^{\text{inc}}(\vec{x}) \hat{J}_m^{\text{tot}}(\vec{x}) - \hat{\Psi}^{\text{tot}}(\vec{x}) \hat{J}_m^{\text{inc}}(\vec{x}) \right] dA(\vec{x}), \end{aligned} \quad (4.18)$$

where $\mathbb{A}_{\mathcal{N}}$ is the surface of the \mathcal{N} -th termination port. Note that it is assumed that terminals themselves are perfectly conducting, and so the electric potential on them will be constant.

In the interior of the source domain we choose a reference point \vec{x}^{ref} where we assign the electric potential $\hat{\Psi}(\vec{x}^{\text{ref}})$ to be zero. In reference with this point, terminal \mathcal{N} has a voltage $\hat{V}_{\mathcal{N}}$ and consequently the right-hand side of equation (4.18) satisfies

$$\begin{aligned} \sum_{\mathcal{N}} \int_{\vec{x} \in \mathbb{A}_{\mathcal{N}}} \nu_m \left[\hat{\Psi}^{\text{inc}}(\vec{x}) \hat{J}_m^{\text{tot}}(\vec{x}) - \hat{\Psi}^{\text{tot}}(\vec{x}) \hat{J}_m^{\text{inc}}(\vec{x}) \right] dA(\vec{x}) \\ = \sum_{\mathcal{N}} \left[\hat{V}_{\mathcal{N}}^{\text{inc}} \hat{I}_{\mathcal{N}}^{\text{tot}} - \hat{V}_{\mathcal{N}}^{\text{tot}} \hat{I}_{\mathcal{N}}^{\text{inc}} \right], \end{aligned} \quad (4.19)$$

where $\hat{I}_{\mathcal{N}}$ is the electric-line-current density at the surface of the port of the conductor with constant voltage $\hat{V}_{\mathcal{N}}$. Combining equation (4.10) with the results of equation (4.19), we obtain

$$\sum_{\mathcal{N}} \left[\hat{V}_{\mathcal{N}}^{\text{inc}} \hat{I}_{\mathcal{N}}^{\text{tot}} - \hat{V}_{\mathcal{N}}^{\text{tot}} \hat{I}_{\mathcal{N}}^{\text{inc}} \right] = - \int_{\vec{x} \in \mathbb{D}^{\text{sct}}} s \delta \hat{\varepsilon}(\vec{x}) \hat{E}_k^{\text{inc}}(\vec{x}) \hat{E}_k^{\text{tot}}(\vec{x}) dV(\vec{x}) . \quad (4.20)$$

For a system containing several antennas, transmitters and receivers, the voltages at the ports, $\hat{V}_{\mathcal{N}}$, can be written as a function of the impedance matrix $\hat{Z}_{\mathcal{N},\mathcal{N}'}$ and the electric-line-current densities $\hat{I}_{\mathcal{N}'}$, viz.

$$\hat{V}_{\mathcal{N}} = \hat{Z}_{\mathcal{N},\mathcal{N}'} \hat{I}_{\mathcal{N}'} . \quad (4.21)$$

Inserting this in equation (4.20) we obtain

$$\delta \hat{Z}_{\mathcal{N},\mathcal{N}'} \hat{I}_{\mathcal{N}'}^{\text{inc}} \hat{I}_{\mathcal{N}}^{\text{tot}} = - \int_{\vec{x} \in \mathbb{D}} s \delta \hat{\varepsilon}(\vec{x}) \hat{E}_k^{\text{inc}}(\vec{x}) \hat{E}_k^{\text{tot}}(\vec{x}) dV(\vec{x}) , \quad (4.22)$$

where

$$\delta \hat{Z}_{\mathcal{N},\mathcal{N}'} = \hat{Z}_{\mathcal{N},\mathcal{N}'}^{\text{inc}} - \hat{Z}_{\mathcal{N}',\mathcal{N}}^{\text{tot}} . \quad (4.23)$$

Next, we can use the property that the electric wavefield is linearly dependent on the electric-line-current density $\hat{I}_{\mathcal{N}}$, hence

$$\hat{E}_k^{\text{inc,tot}}(\vec{x}) = \hat{e}_{k;\mathcal{N}}^{\text{inc,tot}}(\vec{x}) \hat{I}_{\mathcal{N}}^{\text{inc,tot}} , \quad (4.24)$$

where $\hat{e}_{k;\mathcal{N}}^{\text{inc,tot}}(\vec{x})$ is the electric wavefield caused by an electric-unit-current density at the port with label \mathcal{N} . Consequently, we obtain for equation (4.22), after applying the Born approximation in $\hat{e}_{k;\mathcal{N}}^{\text{tot}}(\vec{x})$,

$$\delta \hat{Z}_{\mathcal{N},\mathcal{N}'} = - \int_{\vec{x} \in \mathbb{D}} s \delta \hat{\varepsilon}(\vec{x}) \hat{e}_{k;\mathcal{N}}^{\text{inc}}(\vec{x}) \hat{e}_{k;\mathcal{N}'}^{\text{inc}}(\vec{x}) dV(\vec{x}) . \quad (4.25)$$

Note that an expression for the incident field $\hat{e}_k^{\text{inc}}(\vec{x})$ is obtained in the previous chapter.

4.2 Measuring in bistatic mode

One of the applications of the borehole antenna system is probing the trajectory of a tunnel. Before the complete tunnel is drilled, a small borehole is made to explore the subsurface. Therefore, the system is positioned in the borehole,

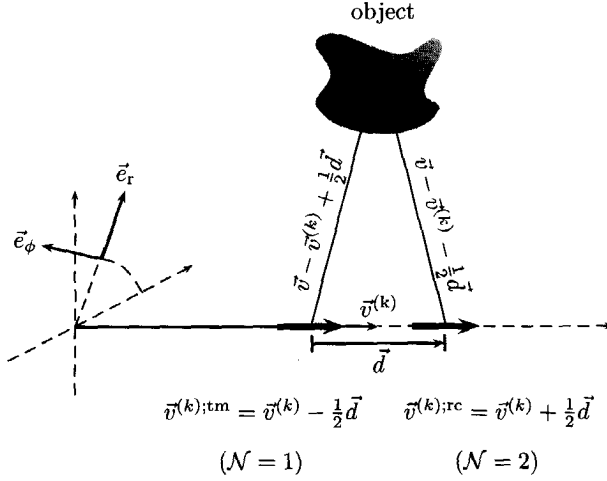


Figure 4.4: The antenna system positioned at $\vec{v}^{(k)}$. The transmitter at $\vec{v}^{(k);tm} = \vec{v}^{(k)} - \frac{1}{2}\vec{d}$ ($\mathcal{N} = 1$) and the receiver at $\vec{v}^{(k);rc} = \vec{v}^{(k)} + \frac{1}{2}\vec{d}$ ($\mathcal{N} = 2$) are separated by the vector \vec{d} .

pointed and moved in the \vec{e}_1 -direction while it rotates around the x_1 -axis. Consequently, it is convenient to use the circular cylindrical coordinate system with unit vectors $\{\vec{e}_1, \vec{e}_r, \vec{e}_\phi\}$, and where a vector \vec{v} is denoted by the parameters $v_i = \{x_1, r, \phi\}$, see appendix A.

The borehole system operates in a bistatic setup, containing one transmitting and one receiving antenna, see figure 4.4. After grounding one port of each antenna, we obtain a system which acts as a two port system ($\mathcal{N} = 1, 2$). Applying equation (4.21) to this setup, we obtain

$$\hat{V}_2 = \hat{Z}_{2,1}\hat{I}_1 + \hat{Z}_{2,2}\hat{I}_2, \quad (4.26)$$

where \hat{V}_2 represent the measured voltage at the receiver, \hat{I}_1 and \hat{I}_2 the electric-source currents at the transmitter and the receiver, $\hat{Z}_{1,2}$ the mutual self-impedance of the transmitter and the receiver, and $\hat{Z}_{2,2}$ the self-impedance of the receiver. Note that we assume the medium to be reciprocal and consequently $\hat{Z}_{1,2} = \hat{Z}_{2,1}$. Since the receiver voltage is measured over an open port, the current through the receiver equals zero, $\hat{I}_2 = 0$. Therefore, the measured voltage at receiver in equation (4.26) reads

$$\hat{V}_2^{rc} = \hat{Z}\hat{I}_1^{tm}, \quad (4.27)$$

since $\hat{V}_2 = \hat{V}_2^{rc}$, $\hat{I}_1 = \hat{I}_1^{tm}$ and $\hat{Z}_{1,2} = \hat{Z}$. Consequently, the expression for the

change in impedance, equation (4.23), will read

$$\delta \hat{Z} = \frac{\delta \hat{V}^{\text{rc}}}{\hat{I}^{\text{tm}}} , \quad (4.28)$$

where we assume that the source current in the transmitter, \hat{I}^{tm} , remains constant, despite changes in medium parameters, while these changes will influence the measured voltage at the receiver, hence

$$\delta \hat{V}^{\text{rc}} = \hat{V}^{\text{rc};\text{inc}} - \hat{V}^{\text{rc};\text{tot}} . \quad (4.29)$$

All measurements take place at positions $\vec{v}^{(k)} = (x_1^{(k)}, 0, \phi^{(k)})$ in the circular cylindrical domain \mathbb{D} . The superscript (k) corresponds to an integer value specifying the measurement. The $x_1^{(k)}$ -component of the position vector points to the center of the system, while the $\phi^{(k)}$ -component specifies the spatial orientation. The transmitter is positioned at \vec{v}^{tm} and separated from an identical antenna as receiver at \vec{v}^{rc} by the vectorial quantity \vec{d} . Therefore, equation (4.25) reads for $\mathcal{N} = 1$ and $\mathcal{N}' = 2$ in the circular cylindrical coordinate system as

$$\delta \hat{V}^{\text{rc}}(\vec{v}^{(k)}) = \hat{I}^{\text{tm}} \int_{\vec{v} \in \mathbb{R}^3} \delta \hat{\varepsilon}(\vec{v}) \hat{S}(\vec{v}|\vec{v}^{(k)}) dV(\vec{v}) , \quad (4.30)$$

where $\hat{S}(\vec{v}|\vec{v}^{(k)})$ reads

$$\hat{S}(\vec{v}|\vec{v}^{(k)}) = -s \hat{e}_{v_k}^{\text{tm}}(\vec{v}|\vec{v}^{(k); \text{tm}}) \hat{e}_{v_k}^{\text{rc}}(\vec{v}|\vec{v}^{(k); \text{rc}}) , \quad (4.31)$$

where

$$\vec{v}^{(k); \text{tm}} = \vec{v}^{(k)} - \frac{1}{2} \vec{d} , \quad (4.32)$$

$$\vec{v}^{(k); \text{rc}} = \vec{v}^{(k)} + \frac{1}{2} \vec{d} , \quad (4.33)$$

and where $\hat{e}_{v_k}^{\text{tm}}(\vec{v}|\vec{v}^{(k); \text{tm}})$ is the electric wavefield at \vec{v} caused by the transmitter at $\vec{v}^{(k); \text{tm}}$, and where $\hat{e}_{v_k}^{\text{rc}}(\vec{v}|\vec{v}^{(k); \text{rc}})$ is the electric wavefield caused by the receiver if it was a transmitter. The sensitivity function $\hat{S}(\vec{v}|\vec{v}^{(k)})$ can be understood as the response of the antenna system to a unit point scatterer at \vec{v} while the system is located at $\vec{v}^{(k)}$.

In view of the angular convolution and periodicity of the sensitivity function $\hat{S}(\vec{v}|\vec{v}^{(k)})$ we use the advantages of the discrete Fourier series. The discrete Fourier series of a scalar function $f(\phi)$ is introduced. The series is defined as

$$f(\phi) = \sum_{n=-\infty}^{\infty} f^{(n)} \exp(in\phi) , \quad (4.34)$$

where

$$f^{(n)} = \frac{1}{2\pi} \int_{\phi=0}^{2\pi} f(\phi) \exp(-in\phi) d\phi . \quad (4.35)$$

Applying equations (4.34) and (4.35) to equation (4.30) leads to the decoupled integral equations in the discrete spatial Fourier domain

$$\delta \hat{V}^{(n)}(x_1^{(k)}) = \hat{I}^{\text{tm}} \int_{x_1=-\infty}^{\infty} \int_{r=0}^{\infty} \delta \hat{\varepsilon}^{(n)}(x_1, r) \hat{S}^{(n)}(x_1, r | x_1^{(k)}) dx_1 r dr , \quad \forall n = -\infty, \dots, \infty , \quad (4.36)$$

for known

$$\hat{S}^{(n)}(x_1, r | x_1^{(k)}) = \frac{1}{2\pi} \int_{\phi=0}^{2\pi} \exp(-in\phi) \hat{S}(\vec{v} | \vec{v}^{(k)}) d\phi , \quad (4.37)$$

$$\delta \hat{V}^{\text{rc};(n)}(x_1^{(k)}) = \frac{1}{2\pi} \int_{\phi=0}^{2\pi} \exp(-in\phi) \delta \hat{V}^{\text{rc}}(\vec{v}) d\phi , \quad (4.38)$$

and \hat{I}^{tm} , and unknown medium parameters $\delta \hat{\varepsilon}^{(n)}(x_1, r)$. Once we have a solution for $\delta \hat{\varepsilon}^{(n)}(x_1, r)$, we retrieve $\delta \hat{\varepsilon}^{(n)}(\vec{v})$ via

$$\delta \hat{\varepsilon}^{(n)}(\vec{v}) = \sum_{n=-\infty}^{\infty} \exp(in\phi) \delta \hat{\varepsilon}^{(n)}(x_1, r) . \quad (4.39)$$

4.3 Discretization of the spatial domain

To be able to model the change in antenna-system impedance caused by a point scatter positioned at \vec{v}^{sct} , equation (4.36) needs to be discretized. Therefore, we define the various quantities on a grid in the circular cylindrical domain \mathbb{D} , with $(2 \times L + 1) \times M \times N$ subdomains $\mathbb{D}_{l,m,n}$, viz.

$$\mathbb{D}_{l,m,n} = \{ \vec{v} \in \mathbb{R}^3 | x_{1;l-1} < x_1 < x_{1;l}; r_{m-1} < r < r_m; \phi_{n-1} < \phi < \phi_n \} , \quad (4.40)$$

see figure 4.5, and where the parameters of a vector $v_{l,m,n}$ are defined on this grid as

$$x_{1;l} = l\Delta x , \quad \forall l = -L, \dots, L , \quad (4.41)$$

$$r_m = m\Delta r , \quad \forall m = 1, \dots, M , \quad (4.42)$$

$$\phi_n = n\Delta\phi , \quad \forall n = -\frac{N}{2} + 1, \dots, \frac{N}{2} , \quad (4.43)$$

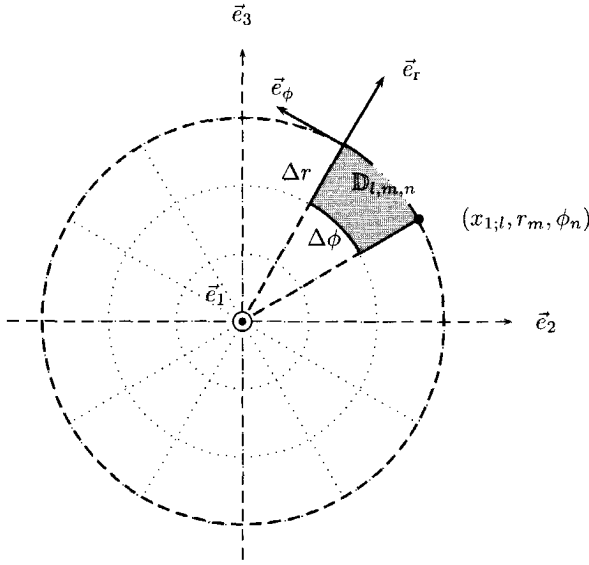


Figure 4.5: Discretization of the spatial domain \mathbb{D} into subdomains $\mathbb{D}_{l,m,n}$, with step sizes Δr and $\Delta\phi$ for the \vec{e}_r and \vec{e}_ϕ -direction, and for fixed value $x_{1;k}$. The unit vector \vec{e}_1 is pointing perpendicular to the plane of the paper.

note that N is even and satisfies $N\Delta\phi = 2\pi$. In this discretized spatial domain, the discrete positions of the antenna system are denoted by the vector $v_{l,n}^{(k)}$, hence

$$x_{1;l}^{(k)} = l\Delta x, \quad \forall l = 1, \dots, L', \quad (4.44)$$

$$r^{(k)} = 0, \quad (4.45)$$

$$\phi_n^{(k)} = n\Delta\phi, \quad \forall n = -\frac{N}{2} + 1, \dots, \frac{N}{2}, \quad (4.46)$$

and where the positions of the transmitter and the receiver are denoted by the vectors $v_{l,n}^{(k);\text{tm}}$ and $v_{l,n}^{(k);\text{rc}}$, which depend on the position of the antenna system $v_{l,n}^{(k)}$, hence

$$x_{1;l}^{(k);\text{tm,rc}} = x_{1;l}^{(k)} + \frac{1}{2}d^{\text{tm,rc}}, \quad \forall l = 1, \dots, L', \quad (4.47)$$

$$r^{(k);\text{tm,rc}} = r^{(k)}, \quad (4.48)$$

$$\phi_n^{(k);\text{tm,rc}} = \phi_n^{(k)}, \quad \forall n = -\frac{N}{2} + 1, \dots, \frac{N}{2}, \quad (4.49)$$

where $d^{\text{tm}} = -d$, while $d^{\text{rc}} = d$. Note that measurements only take place in the positive \tilde{e}_1 -direction, and that the number of angular steps remains constant. Measurements take place for discrete temporal angular frequencies ω_t . We take an equidistant temporal discretization, so that each element of the temporal angular frequency domain Ω becomes

$$\omega_t = t\Delta\omega \quad \forall t = 1, \dots, T, \quad (4.50)$$

hence,

$$\hat{I}_t^{\text{tm}} = \hat{I}^{\text{tm}}(\omega_t). \quad (4.51)$$

After discretization of the spatial domain, the following quantities are defined on the grid as follows,

$$\delta\hat{\varepsilon}_{l,m,n;t} = \delta\varepsilon(v_{l,m,n};\omega_t), \quad (4.52)$$

$$\delta\hat{V}_{l,n;t}^{\text{rc}} = \delta\hat{V}^{\text{rc}}(v_{l,n}^{(k)};\omega_t), \quad (4.53)$$

$$\hat{S}_{l',m',n';l,n;t} = \hat{S}(v_{l',m',n'}|v_{l,n}^{(k)};\omega_t), \quad (4.54)$$

$$\hat{e}_{j;l',m',n';l,n;t}^{\text{tm}} = \begin{pmatrix} \hat{e}_1^{\text{tm}}(v_{l',m',n'}|v_{l,n}^{(k);\text{tm}};\omega_t) \\ \hat{e}_2^{\text{tm}}(v_{l',m',n'}|v_{l,n}^{(k);\text{tm}};\omega_t) \\ \hat{e}_3^{\text{tm}}(v_{l',m',n'}|v_{l,n}^{(k);\text{tm}};\omega_t) \end{pmatrix}, \quad (4.55)$$

$$\hat{e}_{j;l',m',n';l,n;t}^{\text{rc}} = \begin{pmatrix} \hat{e}_1^{\text{rc}}(v_{l',m',n'}|v_{l,n}^{(k);\text{rc}};\omega_t) \\ \hat{e}_2^{\text{rc}}(v_{l',m',n'}|v_{l,n}^{(k);\text{rc}};\omega_t) \\ \hat{e}_3^{\text{rc}}(v_{l',m',n'}|v_{l,n}^{(k);\text{rc}};\omega_t) \end{pmatrix}. \quad (4.56)$$

In the spatial angular Fourier domain, $\delta\hat{\varepsilon}_{l,m;t}^{(n)}$, $\delta\hat{V}_{l;t}^{\text{rc};(n)}$, and $\hat{S}_{l',m';l;t}^{(n)}$ are defined as

$$\delta\hat{\varepsilon}_{l,m;t}^{(n)} = \delta\varepsilon(l\Delta x, m\Delta r; n; \omega_t), \quad (4.57)$$

$$\delta\hat{V}_{l;t}^{\text{rc};(n)} = \delta\hat{V}^{\text{rc}}(l\Delta x; n; \omega_t), \quad (4.58)$$

$$\hat{S}_{l',m';l;t}^{(n)} = \hat{S}(l'\Delta x, m'\Delta r|l\Delta x; n; \omega_t), \quad (4.59)$$

for $n = -\frac{N}{2} + 1, \dots, \frac{N}{2}$.

Using these definitions for the quantities, the decoupled integral equation (4.36) in the discretized spatial angular Fourier domain reads

$$\delta \hat{V}_{l;t}^{\text{rc};(n)} = \hat{I}_t^{\text{tm}} \sum_{l'=-L}^L \sum_{m'=1}^M \delta \hat{\varepsilon}_{l',m';t}^{(n)} \hat{S}_{l',m';l;t}^{(n)} m' \Delta x \Delta r \Delta r, \quad (4.60)$$

for $n = -\frac{N}{2} + 1, \dots, \frac{N}{2}$, where the quantities $\delta \hat{V}_{l;t}^{\text{rc};(n)}$, $\delta \hat{\varepsilon}_{l',m';t}^{(n)}$, and $\hat{S}_{l',m';l;t}^{(n)}$ are obtained via

$$\delta \hat{V}_{l;t}^{\text{rc};(n)} = \frac{\Delta \phi}{2\pi} \sum_{n'=-\frac{N}{2}+1}^{\frac{N}{2}} \exp(-inn' \Delta \phi) \delta \hat{V}_{l,n';t}^{\text{rc}}, \quad (4.61)$$

$$\delta \hat{\varepsilon}_{l',m';t}^{(n)} = \frac{\Delta \phi}{2\pi} \sum_{n'=-\frac{N}{2}+1}^{\frac{N}{2}} \exp(-inn' \Delta \phi) \delta \hat{\varepsilon}_{l',m',n';t}, \quad (4.62)$$

$$\hat{S}_{l',m';l;t}^{(n)} = \frac{\Delta \phi}{2\pi} \sum_{n'=-\frac{N}{2}+1}^{\frac{N}{2}} \exp(-inn' \Delta \phi) \hat{S}_{l',m',n';l,n;t}, \quad (4.63)$$

in which

$$\hat{S}_{l',m',n';l,n;t} = -i t \Delta \omega \hat{e}_{j;l',m',n';l,n;t}^{\text{tm}} \hat{e}_{j;l',m',n';l,n;t}^{\text{rc}}, \quad (4.64)$$

for primed parameters $l' = -L, \dots, L$, $m' = 1, \dots, M$, and $n' = -\frac{N}{2} + 1, \dots, \frac{N}{2}$, while the unprimed parameters run for $l = 1, \dots, L'$, $n = -\frac{N}{2} + 1, \dots, \frac{N}{2}$, and $t = 1, \dots, T$.

After obtaining an estimate for the contrast in the subsurface in the angular Fourier domain, $\delta \hat{\varepsilon}_{l',m';t}^{(n)}$, the contrast in the spatial domain, $\delta \hat{\varepsilon}_{l',m',n';t}$, is arrived at as

$$\delta \hat{\varepsilon}_{l',m',n';t} = \sum_{n=-\frac{N}{2}+1}^{\frac{N}{2}} \exp(inn' \Delta \phi) \delta \hat{\varepsilon}_{l',m';t}^{(n)} \Delta \phi. \quad (4.65)$$

4.4 The effective sensitivity function

The synthetic radiation characteristics of the antenna system present in the sensitivity function $\hat{S}_{l',m',n';l,n;t}$ are obtained from the modeling done in chapter 3. During imaging, the characteristics are needed at several frequencies over the complete spatial domain. In order to reduce the computational time we approximate the sensitivity function by an effective one. Therefore, we compute

only one radiation pattern Γ of the electric wavefield from the antenna system, which is at the central frequency of the emitted signal, and at fixed distance and depth, hence

$$\Gamma(\phi) = \hat{e}_{x_1}((x_1 = 0, r = r_0, \phi) | \vec{v} = 0; \omega = 2\pi f_0) . \quad (4.66)$$

Note that this pattern is obtained using the model obtained in chapter 3. This angular dependent function is multiplied with the omni-directional radiation pattern $\hat{e}_{v_k}^{\text{dip}}(\vec{v} | \vec{v}^{(k)})$ of an electric dipole, in order to obtain an approximation for the directional radiation pattern of the antenna system, hence the sensitivity function from equation (4.31) is approximated as

$$\hat{S}(\vec{v} | \vec{v}^{(k)}) \equiv -s \left(\Gamma(\phi - \phi^{(k)}) \right)^2 \hat{e}_{v_k}^{\text{dip}}(x_1, r | x_1^{(k); \text{tm}}) \hat{e}_{v_k}^{\text{dip}}(x_1, r | x_1^{(k); \text{rc}}) . \quad (4.67)$$

In order to apply the above in a discretized sensitivity function, the radiation pattern $\Gamma(\phi - \phi^{(k)})$ and the electric dipole wavefields are discretized. Therefore, we define these quantities on the same grid as used in the previous section, viz.

$$\Gamma_{n', n} = \Gamma(n' \Delta \phi - n \Delta \phi) , \quad \forall \{n', n\} = -\frac{N}{2} + 1, \dots, \frac{N}{2} , \quad (4.68)$$

$$\hat{e}_{j; l', m'; l; t}^{\text{dip}} = \begin{pmatrix} \hat{e}_1^{\text{dip}}(l' \Delta x, m' \Delta r | l \Delta x_1; \omega_t) \\ \hat{e}_2^{\text{dip}}(l' \Delta x, m' \Delta r | l \Delta x_1; \omega_t) \\ \hat{e}_3^{\text{dip}}(l' \Delta x, m' \Delta r | l \Delta x_1; \omega_t) \end{pmatrix} , \quad (4.69)$$

and where the omni-directional wavefields from the antennas, $\hat{e}_{j; l', m'; l; t}^{\text{dip}}$, satisfies

$$\begin{aligned} \hat{e}_{1; l', m'; l; t}^{\text{dip}} &= \mathcal{G}_{v_{1,1}}^{E,J}(v_{l', m', n'} | v_{l,n}^{(k)}) \\ &= -\frac{\gamma^2}{-i t \Delta \omega \delta \hat{\varepsilon}} \langle \hat{G} \rangle(v_{l', m', n'} | v_{l,n}^{(k)}) \\ &\quad + \frac{-1}{i t \Delta \omega \delta \hat{\varepsilon}} \frac{1}{\Delta x_1^2} \left[\langle \hat{G} \rangle(v_{l'+1, m', n'} | v_{l,n}^{(k)}) \right. \\ &\quad \left. - 2 \langle \hat{G} \rangle(v_{l', m', n'} | v_{l,n}^{(k)}) + \langle \hat{G} \rangle(v_{l'-1, m', n'} | v_{l,n}^{(k)}) \right] , \end{aligned} \quad (4.70)$$

$$\begin{aligned} \hat{e}_{2; l', m'; l; t}^{\text{dip}} &= \mathcal{G}_{v_{2,1}}^{E,J}(v_{l', m', n'} | v_{l,n}^{(k)}) \\ &= \frac{-1}{i t \Delta \omega \delta \hat{\varepsilon}} \frac{1}{4 \Delta x_1 \Delta v_2} \\ &\quad \left[\langle \hat{G} \rangle(v_{l'+1, m'+1, n'} | v_{l,n}^{(k)}) - \langle \hat{G} \rangle(v_{l'-1, m'+1, n'} | v_{l,n}^{(k)}) \right. \\ &\quad \left. - \langle \hat{G} \rangle(v_{l'+1, m'-1, n'} | v_{l,n}^{(k)}) + \langle \hat{G} \rangle(v_{l'-1, m'-1, n'} | v_{l,n}^{(k)}) \right] , \end{aligned} \quad (4.71)$$

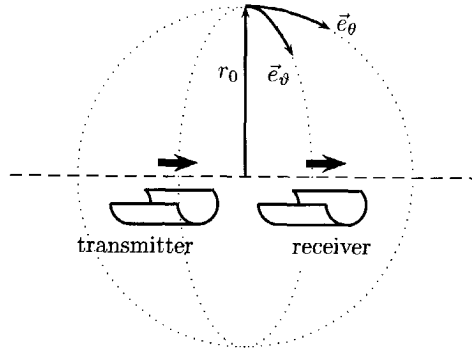


Figure 4.6: The direction of \vec{e}_ϑ and \vec{e}_θ in reference with the tool.

$$\hat{e}_{3;l',m';l;t}^{\text{dip}} = \mathcal{G}_{v_{3,1}}^{E,J}(v_{l',m',n'}|v_{l,n}^{(k)}) = 0, \quad (4.72)$$

for $m = 1$ and $n = n' = 0$, and where $\langle \hat{G} \rangle(v_{l',m',n'}|v_{l,n})$ is the Green function from chapter 3. Finally, the discretized sensitivity satisfies

$$\hat{S}_{l',m',n';l,n;t} = -i t \Delta\omega \Gamma_{n',n}^2 \hat{e}_{j;l',m';l;t}^{\text{dip}} \hat{e}_{j;l',m';l,n;t}^{\text{dip}}. \quad (4.73)$$

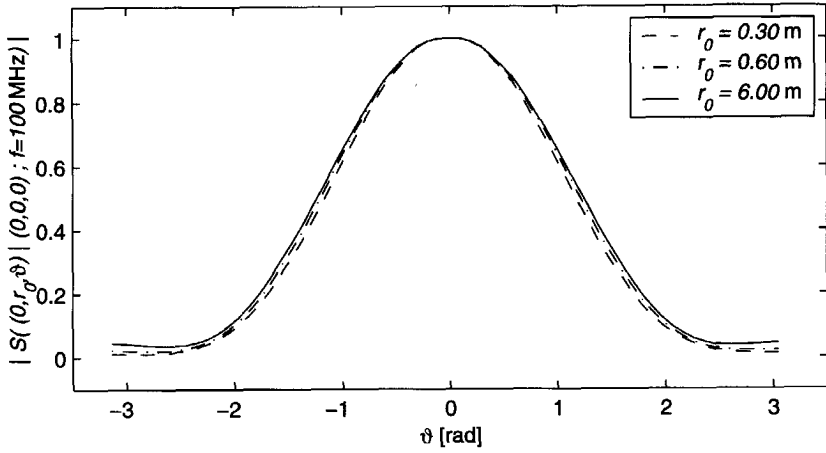
In order to validate the approximation, we need to explore the sensitivity function at several frequencies and radial distances.

4.5 Exploring the effective sensitivity function

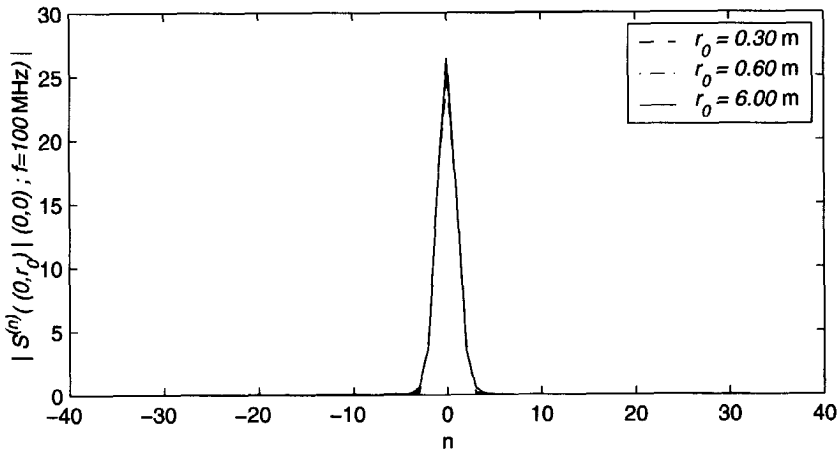
In section 4.4 we made two assumptions:

- the radiation pattern $\Gamma(\phi)$ in the effective sensitivity function of the antenna system can be taken independent of the frequency,
- $\Gamma(\phi)$ is the same over all radial distances.

In this section we compare the effective sensitivity function with the “real” sensitivity function computed at several radial distances and for several frequencies. The latter sensitivity functions are computed along the dotted lines shown in figure 4.6, where r_0 is the radial distance, and where ϑ and θ denote the spatial direction. Note that $\{\vartheta, \theta\} = 0$ and $\{\vartheta, \theta\} = \pm\pi$ corresponds to the same point. Further note that ϑ is defined in the same direction as \vec{e}_ϕ .

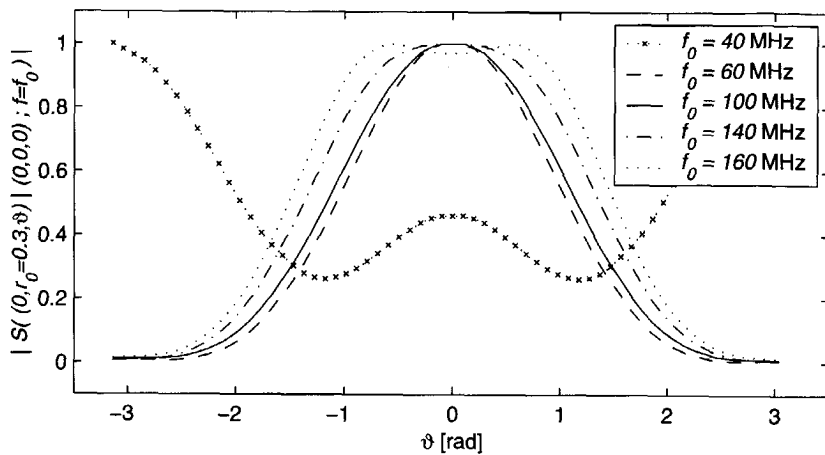


(a)

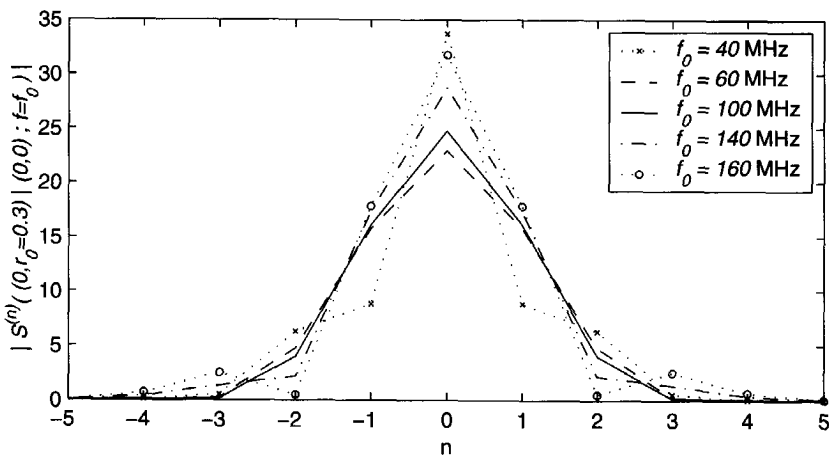


(b)

Figure 4.7: The sensitivity function, computed for the $f_0 = 100$ MHz component, at radial distances $r_0 = \{0.3 \text{ m}, 0.6 \text{ m}, 6.0 \text{ m}\}$ ($r_0 \approx \{0.9\lambda, 1.8\lambda, 17.8\lambda\}$). In (a) $\hat{S}((0, r_0, \vartheta)|(0, 0, 0))$ is shown as function of the angle ϑ , and in (b) $\hat{S}^{(n)}((0, r_0)|(0, 0))$ as a function of $n = -\frac{N}{2} + 1, \dots, \frac{N}{2}$, ($N = 64$).

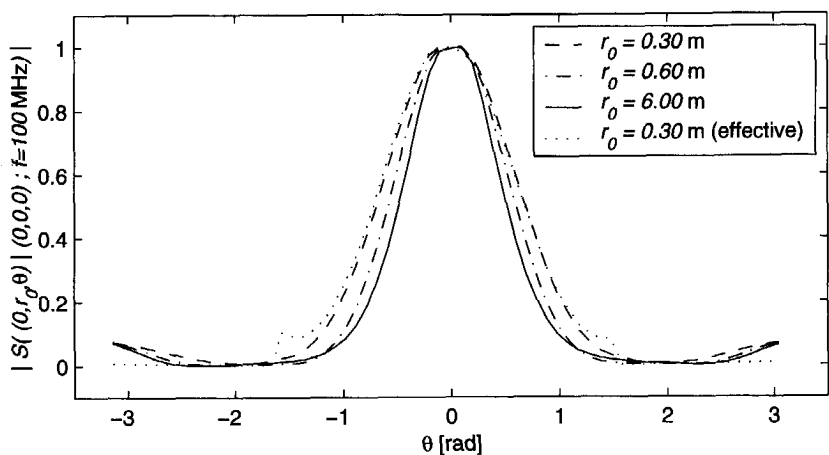


(a)

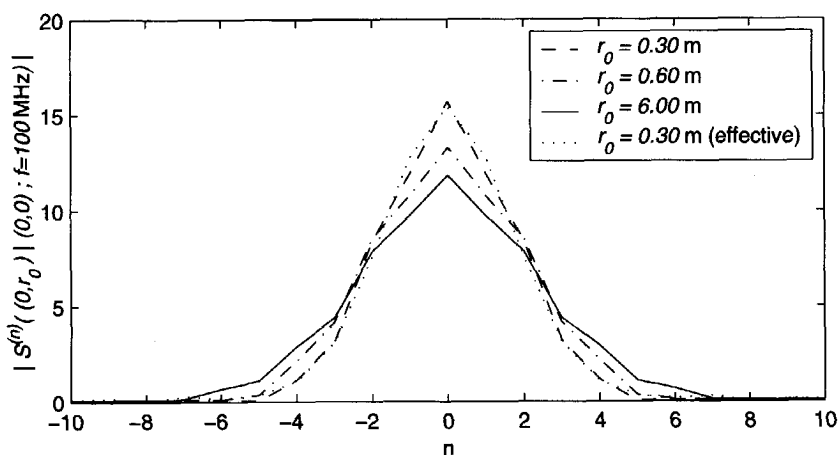


(b)

Figure 4.8: The sensitivity function, computed at a constant radial distance $r_0 = 0.3$ m, for the frequency components $f_0 = \{40, 60, 100, 140, 160\}$ MHz. In (a), $\hat{S}((0, r_0 = 0.3, \vartheta)|(0, 0, 0), \omega)$ is shown as function of the angle ϑ , and in (b), the “relevant” values of $\hat{S}^{(n)}((0, r_0 = 0.3)|(0, 0), \omega)$ are shown in the spatial angular Fourier domain, ($N = 64$).

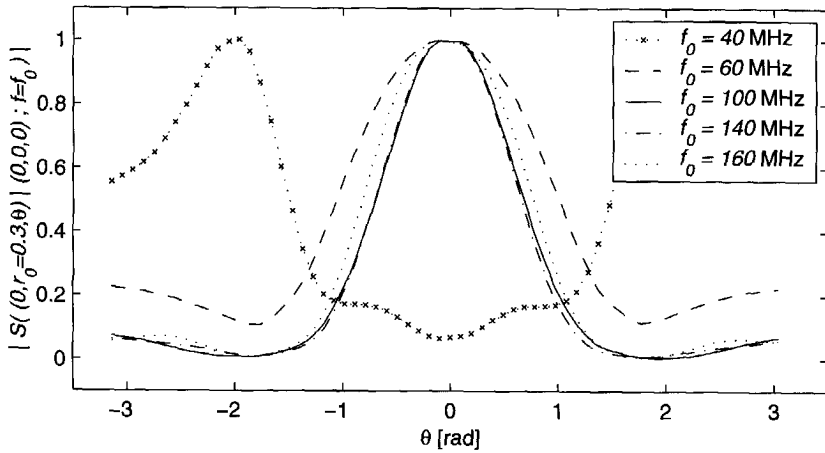


(a)

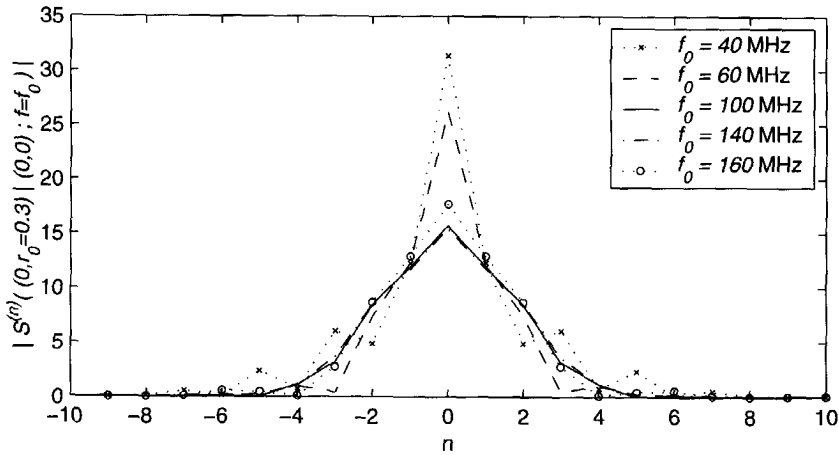


(b)

Figure 4.9: The sensitivity function, computed for the $f_0 = 100$ MHz component, at radial distances $r_0 = \{0.3 \text{ m}, 0.6 \text{ m}, 6.0 \text{ m}\}$ ($r_0 \approx \{0.9\lambda, 1.8\lambda, 17.8\lambda\}$), in the θ -direction. In (a), $\hat{S}((r_0, \vartheta = 0, \theta)|(0, 0, 0))$ is shown as function of the angle ϑ , and in (b), $\hat{S}^{(n)}((0, r_0)|(0, 0))$ is shown as a function of $n = -\frac{N}{2} + 1, \dots, \frac{N}{2}$, ($N = 64$).



(a)



(b)

Figure 4.10: The sensitivity function, computed at a constant radial distance $r_0 = 0.3$ m, for the frequency components $f_0 = \{40, 60, 100, 140, 160\}$ MHz, in the ϑ -direction. In (a), $\hat{S}((r_0 = 0.30, \vartheta = 0, \theta)|(0, 0, 0), \omega)$ is shown as function of the angle ϑ , and in (b), the “relevant” values of $\hat{S}^{(n)}((0, r_0 = 0.30)|(0, 0), \omega)$ are shown in the spatial angular Fourier domain ($N = 64$).

We start with comparing the absolute value of the normalized sensitivity function $\hat{S}(\vec{v}|\vec{v}^{(k)})$ from equation (4.31) for several radial distances. Using the same configuration as in section 3.7, we embed the system in a non-conducting medium with relative permittivity $\epsilon_r = 80$, and set the central frequency at 100 MHz. We compute the function for three radial distances $r_0 = \{0.3 \text{ m}, 0.6 \text{ m}, 6.0 \text{ m}\}$ ($r_0 \approx \{0.9\lambda, 1.8\lambda, 17.8\lambda\}$).

In figure 4.7(a) the sensitivity functions are shown as a function of the angle ϑ in the spatial domain, and in 4.7(b) in the spatial angular Fourier domain as a function of $n = -\frac{N}{2} + 1, \dots, \frac{N}{2}$, for $N = 64$. Note the great similarities between the three radiation patterns, despite the great differences in radial distances. These vary from the near- to the far-field region of the antenna system.

In addition, we verify that $\Gamma(\phi)$ indeed can be taken frequency independent. Using the same configuration, we compute the absolute value of the sensitivity function at a constant radial distance, $r_0 = 0.30 \text{ m}$, while we vary the frequency from $f_0 = 40 \text{ MHz}$ up to $f_0 = 160 \text{ MHz}$. The computed functions (normalized to unity) are shown in figure 4.8(a) as a function of ϑ , and in 4.8(b) in the angular Fourier domain.

Next, we study the patterns in the \vec{e}_θ -direction. In figure 4.9, the 100 MHz component of the sensitivity function at several radial distances are shown for this plane. As a reference, we show the pattern of an effective sensitivity function obtained by multiplying the radiation pattern from an electric dipole with the radiation pattern $\Gamma(\phi)$ obtained from the 100MHz component of the real sensitivity function at a radial distance of 0.30 m in the plane $x = 0$, the dotted line. Note the similarity with the dashed line around $\theta = 0$. In figure 4.10, we show several sensitivity functions at fixed radial distance ($r_0 = 0.3 \text{ m}$) for various frequencies.

From the figures 4.7 and 4.9 it is observed that the radial distance has not a great influence on the radiation pattern. The frequency dependency however, is much larger. Especially in figures 4.8(a) and 4.10(a) it is observed that large variation in the radiation pattern takes place for frequencies below $f_0 = 60 \text{ MHz}$. However, above this frequency, the radiation pattern remains similar. In addition, it is observed from the figures 4.7(b) and 4.8(b) that approximately 9 out the 64 components in the spatial angular Fourier domain have a significant value. In the θ -direction the spectrum is slightly wider (13 out the 64).

Consequently, we can take as effective sensitivity function the radiation pattern belonging to the 100 MHz component of the sensitivity function at a radial distance of 0.3 m in the plane $x_1 = 0$.

4.6 A single step inversion via back-propagation

In order to get an image of the subsurface, we need a solution for the decoupled integral equation (4.36). After we have an estimate for $\delta\hat{\varepsilon}^{(n)}(x_1, r)$, the image is obtained using equation (4.39). The estimate is retrieved from a minimum norm solution of the error functionals $\text{ERR}^{(n)}$. These functionals read

$$\text{ERR}^{(n)} = \sum_{x_1^{(k)} \in \mathbb{D}} \sum_{\omega_t \in \Omega} \left| \delta\hat{V}^{\text{rc};(n)}(x_1^{(k)}) - \hat{I}^{\text{tm}} \int_{x_1=-\infty}^{\infty} \int_{r=0}^{\infty} \delta\varepsilon^{(n)}(x_1, r) \hat{S}^{(n)}(x_1, r|x_1^{(k)}) dx_1 r dr \right|^2 \Delta x_1 \Delta \omega, \quad (4.74)$$

where $\hat{\varepsilon}^{(n)}(x_1, r)$ satisfies

$$\delta\varepsilon^{(n)}(x_1, r) = \alpha^{(n)} \Delta\varepsilon^{(n)}(x_1, r), \quad \forall \omega_t \in \Omega, \quad (4.75)$$

and where \mathbb{D} denotes the spatial circular cylindrical domain and Ω the temporal angular frequency domain. Note that we assume $\delta\varepsilon^{(n)}(x_1, r)$ to be frequency independent. The functional tends towards a minimum when $\alpha^{(n)}$ reads

$$\alpha^{(n)} = \frac{\Re \left[\sum_{x_1^{(k)} \in \mathbb{D}} \sum_{\omega_t \in \Omega} \delta\hat{V}^{\text{rc};(n)}(x_1^{(k)}) \left(\hat{I}^{\text{tm}} \int_{r=0}^{\infty} \int_{x_1=-\infty}^{\infty} \Delta\varepsilon^{(n)}(x_1, r) \hat{S}^{(n)}(x_1, r|x_1^{(k)}) dx_1 r dr \right)^* \right]}{\sum_{x_1^{(k)} \in \mathbb{D}} \sum_{\omega_t \in \Omega} \left| \hat{I}^{\text{tm}} \int_{x_1=-\infty}^{\infty} \int_{r=0}^{\infty} \Delta\varepsilon^{(n)}(x_1, r) \hat{S}^{(n)}(x_1, r|x_1^{(k)}) dx_1 r dr \right|^2}. \quad (4.76)$$

We observe that, apart from a constant, the numerator is maximized by taking as update direction

$$\Delta\varepsilon^{(n)}(x_1, r) = \sum_{x_1^{(k)} \in \mathbb{D}} \sum_{\omega_t \in \Omega} \left(\hat{I}^{\text{tm}} \hat{S}^{(n)}(x_1, r|x_1^{(k)}) \right)^* \delta\hat{V}^{\text{rc};(n)}(x_1^{(k)}). \quad (4.77)$$

Substituting this direction in equation (4.76) we obtain

$$\alpha^{(n)} = \frac{\int_{x_1=-\infty}^{\infty} \int_{r=0}^{\infty} \left| \Delta\varepsilon^{(n)}(x_1, r) \right|^2 dx_1 r dr}{\sum_{x_1^{(k)} \in \mathbb{D}} \sum_{\omega_t \in \Omega} \left| \hat{I}^{\text{tm}} \int_{x_1=-\infty}^{\infty} \int_{r=0}^{\infty} \Delta\varepsilon^{(n)}(x_1, r) \hat{S}^{(n)}(x_1, r|x_1^{(k)}) dx_1 r dr \right|^2}. \quad (4.78)$$

Finally, an image of $\delta\hat{\varepsilon}(\vec{v})$ is obtained using equation (4.39). Note that $\alpha^{(n)}$ is real and only contains angular information.

If we take $\alpha^{(n)} = 1$, for all n , we observe that the measured voltage $\delta\hat{V}^{\text{rc};(n)}(x_1^{(k)})$ is projected from the data domain into the domain of observation, using the kernel function $\left(\hat{I}_t^{\text{tm}}\hat{S}^{(n)}(x_1, r|x_1^{(k)})\right)^*$. Consequently, we refer to this method using the term *standard back-propagation*. In case we use $\alpha^{(n)}$ in our computations, we use the term *minimized back-propagation*.

We will apply this algorithm on both synthetic and measured data. Therefore, we discretize equations (4.75), (4.77) and (4.78), using the results of the sections 4.3 and 4.4, hence

$$\delta\varepsilon_{l,m}^{(n)} = \alpha^{(n)} \Delta\varepsilon_{l,m}^{(n)}, \quad (4.79)$$

$$\Delta\varepsilon_{l,m}^{(n)} = \sum_{l'=1}^{L'} \sum_{t=1}^T \left(\hat{I}_t^{\text{tm}} \hat{S}_{l,m;l',t}^{(n)} \right)^* \delta\hat{V}_{l',t}^{\text{rc};(n)}, \quad (4.80)$$

$$\alpha^{(n)} = \frac{\sum_{l=-L}^L \sum_{m=1}^M \left| \Delta\varepsilon_{l,m}^{(n)} \right|^2 m \Delta x (\Delta r)^2}{\sum_{l'=1}^{L'} \sum_{t=1}^T \left| \sum_{l=-L}^L \sum_{m=1}^M \Delta\varepsilon_{l,m}^{(n)} \hat{I}_t^{\text{tm}} \hat{S}_{l,m;l',t}^{(n)} m \Delta x (\Delta r)^2 \right|^2}, \quad (4.81)$$

Finally, $\delta\varepsilon_{l',m',n'}$ satisfies

$$\delta\varepsilon_{l,m,n} = \sum_{n'=-\frac{N}{2}+1}^{\frac{N}{2}} \exp(inn'\Delta\phi) \delta\varepsilon_{l,m}^{(n')} \Delta\phi, \quad (4.82)$$

where we use the spatial Fourier transform from equation (4.34).

4.7 Synthetic and experimental results back-propagation method

We test the algorithm on both synthetic and measured data, corresponding to the same configuration. Before we show the results, we first discuss the data.

For every antenna position, a single trace is obtained containing 512 measurements, with a time step equal to 1.66 ns. During the imaging, we only use

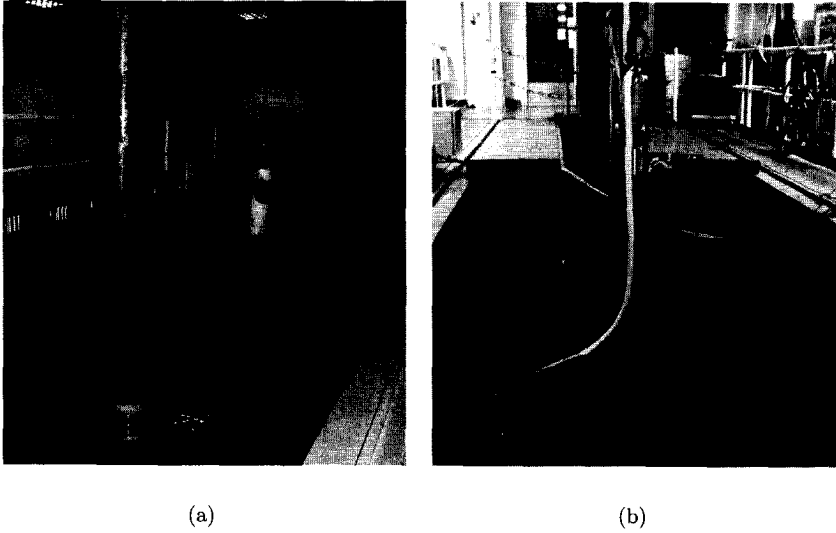


Figure 4.11: The antenna system and the object positioned (a) above the water basin, and (b) under the water table.

the positive frequency components from the range 60–280 MHz. The complete set of discrete antenna positions forms the domain \mathbb{D}^{src} , which satisfies

$$\mathbb{D}^{\text{src}} = \{\vec{v} \in \mathbb{D}^3 | 1.57 \leq x_1 \leq 3.55, r = 0, 0 \leq \phi \leq 2\pi\} , \quad (4.83)$$

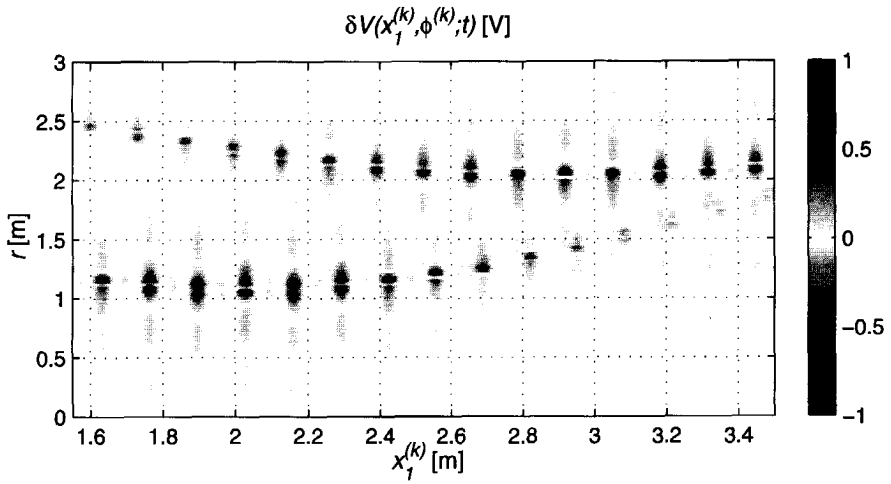
containing of $L' \times N = 15 \times 64$ subdomains in the x_1 and in the ϕ -direction. While, the volume of interest, \mathbb{D} , reads

$$\mathbb{D} = \{\vec{v} \in \mathbb{D}^3 | 0.55 \leq x_1 \leq 3.69, 0 \leq r \leq 4, 0 \leq \phi \leq 2\pi\} , \quad (4.84)$$

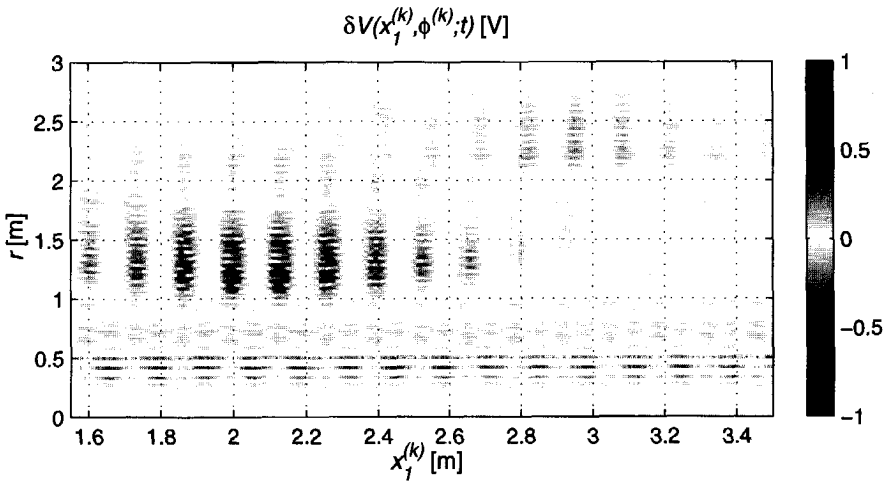
containing $(2L + 1) \times M \times N = 33 \times 100 \times 64$ subdomains in the x_1, r and ϕ -direction, respectively. Although in practice, the system describes a “spiral”, we treat the data as if each 64 measurements in a row are taken at one depth, just like with the synthetic data.

Measurements take place in a deep fresh water basin¹, see figure 4.11, enabling us to control the position of scattering objects and to ensure a homogeneous background medium. The synthetic data and the imaging are based on a background medium, which is non-conductive and has a relative permittivity similar to water (80). We position two objects at $v_i = (2, 1, \pi)$ and $v_i = (3, 2, \frac{3}{2}\pi)$. The first object is a metallic sphere with a diameter of 0.3 m,

¹The water basin is owned by TNO Physics and Electronics Laboratory (TNO-FEL), and designed to test acoustic equipment.



(a)



(b)

Figure 4.12: The (a) synthetic and (b) measured data. The normalized voltage $\delta V(x_1^{(k)}, \phi^{(k)}; t)$ is shown as a function of $x_1^{(k)}$ and the radial distance, where time is transformed to radial distance. Clearly visible are the reflections caused by the two objects.

the second a gastank, having a length of 0.7 m in the axial direction of the antenna system and a diameter of 0.15 m. For the synthetic data we use two point-scatterers, with medium parameters $\sigma = 1$ S/m and $\varepsilon_r = 160$.

Note that we haven't discuss the electric-source current \hat{I}^{tm} yet. For the measured data, it is observed that the maximum amplitude in the power spectrum is in the region near the 100 MHz maximum, however the exact frequency content of the current is unknown. We therefore take the electric current \hat{I}^{tm} equal to one in a finite bandwidth. In practise, the "best" results are obtained when we take $\hat{I}^{\text{tm}} = 1$ for $60 \text{ MHz} < f_0 < 280 \text{ MHz}$ and zero elsewhere.

Synthetic data are generated using equation (4.30). After applying the temporal Fourier transform on the data we obtain the results shown in figure 4.12(a). We clearly observe a change in voltage due to the presence of two objects. The measured data are shown in figure 4.12(b), after correcting for the direct wave by subtracting from each sample in every trace the corresponding sample from the first trace. Further, we tapered the first 30 samples of each trace to avoid high frequency components caused by the correction. Note that we have transformed time to a radial distance, and that we normalize to unity.

The imaging procedure is carried out in the frequency domain, using positive frequencies only. Both back-propagation and minimized back-propagation are applied to the synthetic and the measured data, see figures 4.13-4.16. In these figures the absolute value of the computed contrast are shown in the plane at several x_1 -positions. Exploring the results, we observe great similarities between the results from measured and synthetic data. In both cases we see an increase in angular resolution when we apply minimized back-propagation. However, in addition it results in extra maxima in the angular direction.

Further, we observe a blurring effect in the radial direction in images based on measured data, see figures 4.15 and 4.16. This is caused by the antenna ringing, or the improper choice of the electric-source-current frequency spectrum. Hence, this effect is not present in images from synthetic data where we use the same current density in the forward and inverse problems, see figures 4.13 and 4.14. Furthermore we see that the images of the objects are not positioned at a proper depth in case of the measured data. This is caused by the measuring method: the antenna system follows the path of a "spiral", hence each complete rotation takes place over the complete range of equidistant x_1 -positions, between two gridpoints. The second object is visible over a long range in the x_1 -direction, $2.70 \leq x_1 \leq 3.12$, since this object corresponds to the gastank of length 0.3 m. In addition we observe that the computed contrast of the object at the largest radial distance, has a lower amplitude than the nearby object. Note that this is the case for images from both synthetic and the measured data. Hence, it is interesting to search for an other imaging algorithm where we correct for the radial decay.

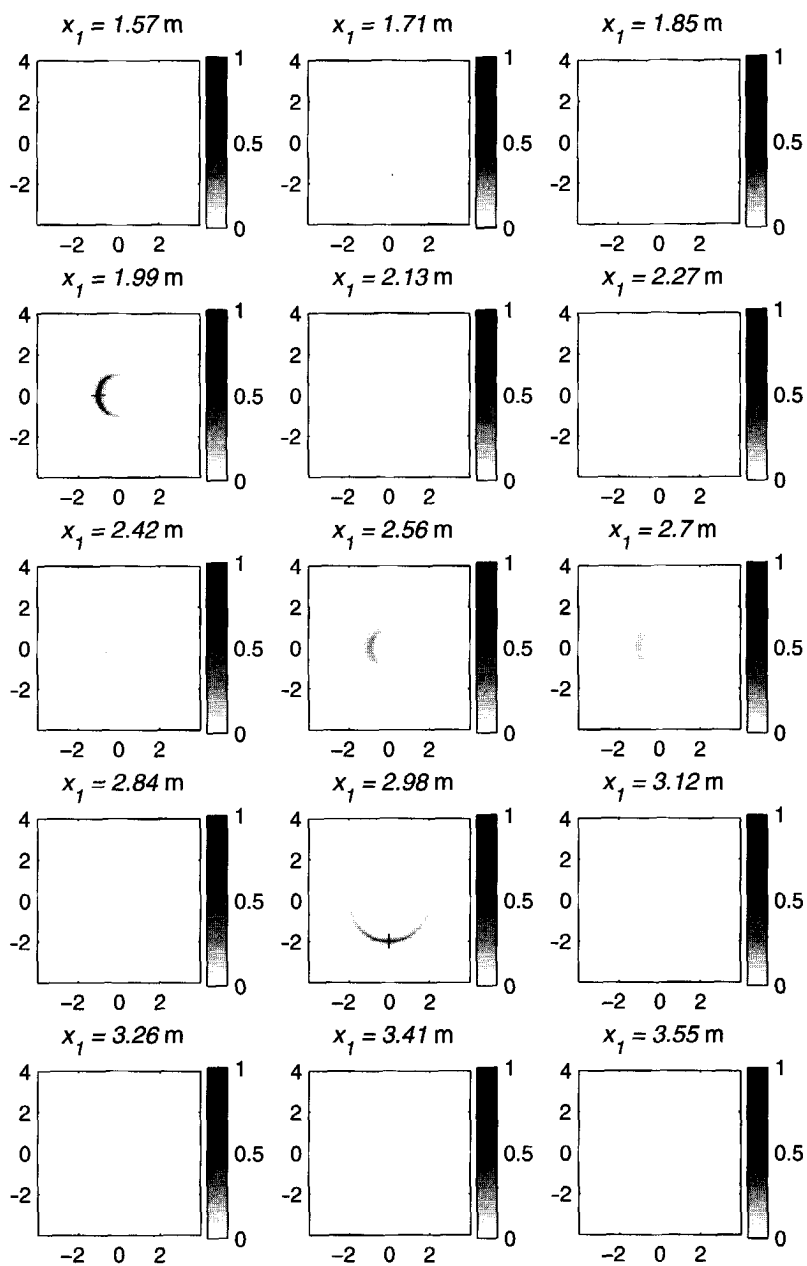


Figure 4.13: The results obtained by applying standard back-propagation on synthetic data. Shown is the normalized absolute value of the computed contrast, $|\delta\epsilon(\vec{x})|$, in the planes at various x_1 -positions. The crosses indicate the positions of the objects.

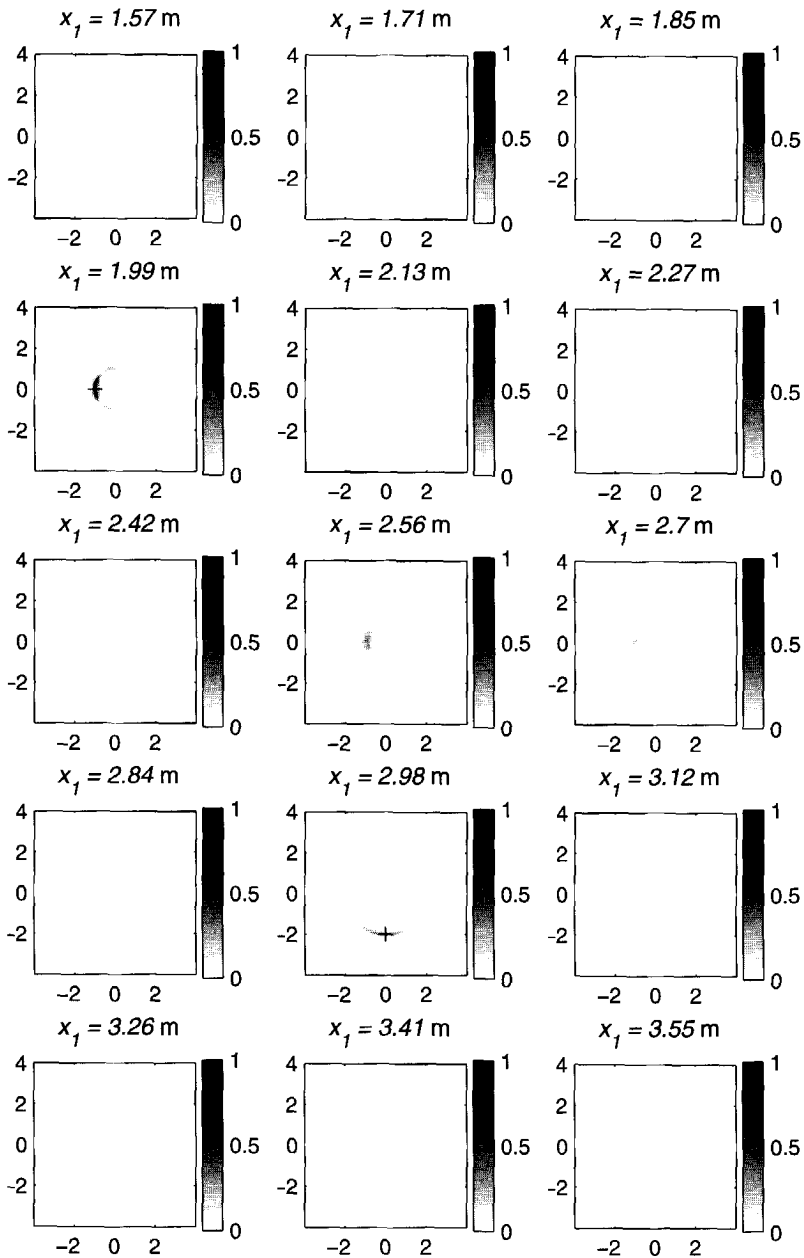


Figure 4.14: The results obtained by applying minimized back-propagation on synthetic data. Shown is the normalized absolute value of the computed contrast, $|\delta\epsilon(\vec{x})|$, in the planes at various x_1 -positions. The crosses indicate the positions of the objects.

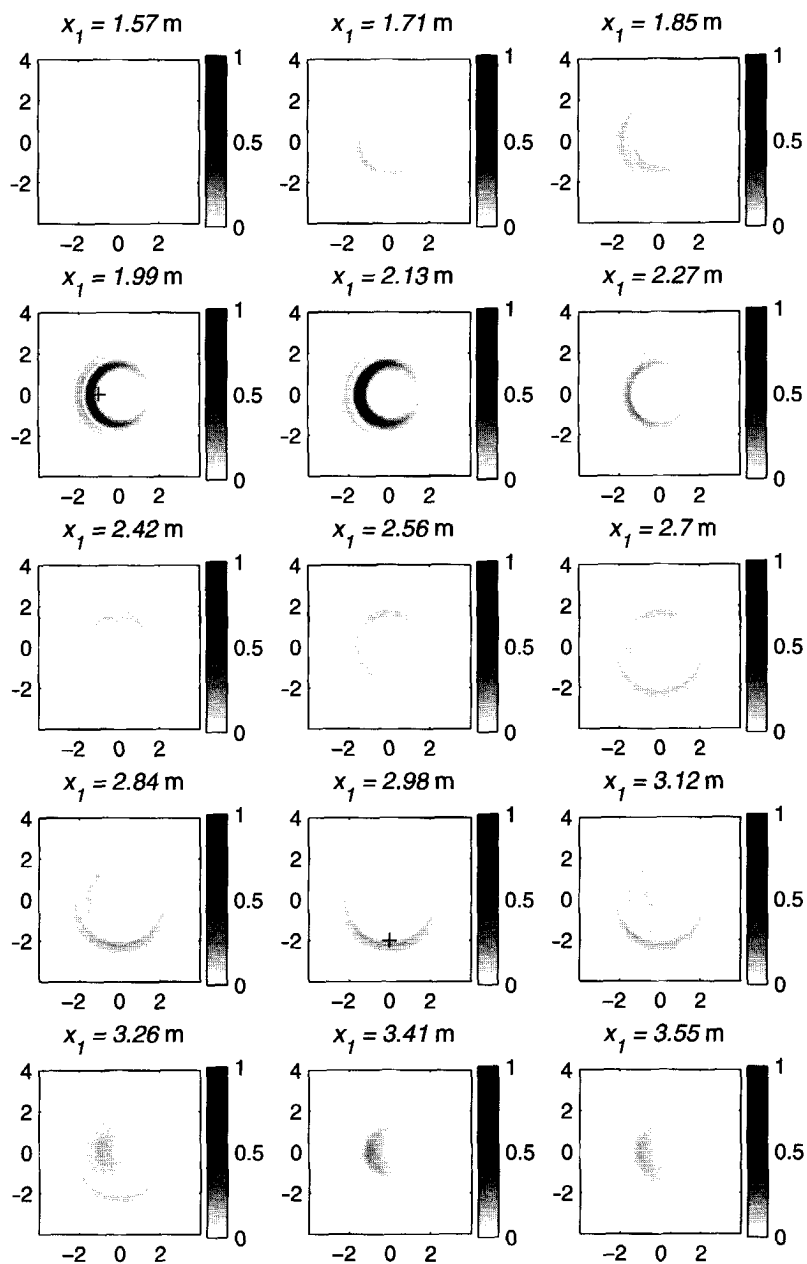


Figure 4.15: The results obtained by applying standard back-propagation on measured data. Shown is the normalized absolute value of the computed contrast, $|\delta\epsilon(\vec{x})|$, in the planes at various x_1 -positions. The crosses indicate the positions of the objects.

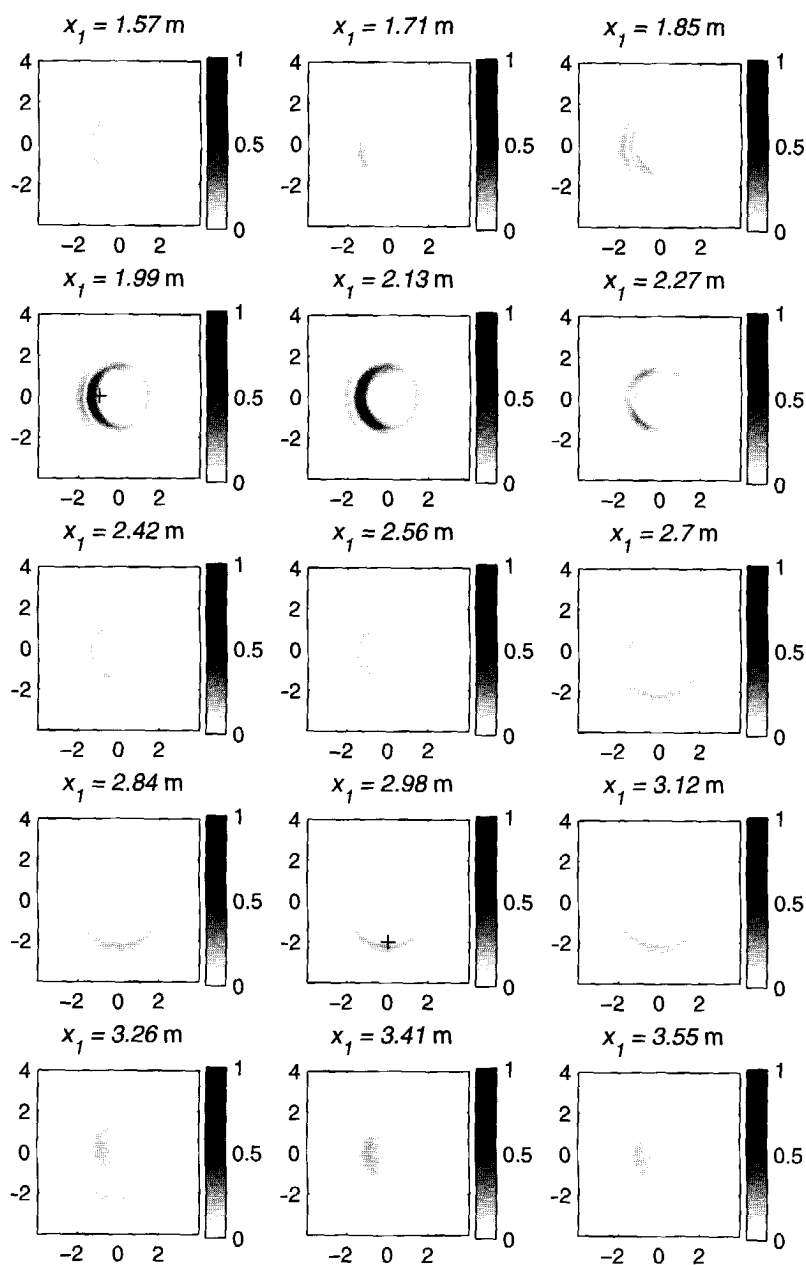


Figure 4.16: The results obtained by applying minimized back-propagation on measured data. Shown is the normalized absolute value of the computed contrast, $|\delta\epsilon(\bar{x})|$, in the planes at various x_1 -positions. The crosses indicate the positions of the objects.

4.8 Conjugate gradient inversion method

The back-propagation from the previous paragraph is a single step inversion algorithm. Since it is the first step of a conjugate gradient (CG) iteration scheme, it is interesting to investigate the effect of applying several iteration steps. Although we know that we deal with an ill-posed problem and that a CG method tends to be sensitive for noise in the data. This sensitivity to noise occurs when we carry many iterations. We expect to gain resolution by applying only a few iteration of CG scheme. Next we develop a CG scheme where we approximate equation (4.60) by

$$\delta \hat{V}^{(n)}(x_1^{(k)}) = \hat{I}^{\text{tm}} \int_{x_1=-\infty}^{\infty} \int_{r=0}^{\infty} \delta \varepsilon^{(n)}(x_1, r) \hat{S}^{(n)}(x_1, r | x_1^{(k)}) dx_1 r dr, \quad \forall n = -\infty, \dots, \infty, \quad (4.85)$$

where we assume the contrast $\delta \varepsilon^{(n)}(x_1, r)$ to be frequency independent.

To discuss our CG scheme in more detail we introduce an operator, a norm and an adjoint operator. We therefore write equation (4.85) as an operator equation, viz.

$$\mathbf{f}^{(n)} = (\mathbf{L}\mathbf{u})^{(n)}, \quad (4.86)$$

where \mathbf{f} is the known (measured) electric potential given by

$$\mathbf{f}_{l;t}^{(n)} = \delta \hat{V}_{l;t}^{\text{rc};(n)}, \quad (4.87)$$

and where the known operator \mathbf{L} is applied on the unknown complex permittivity \mathbf{u} , hence

$$(\mathbf{L}\mathbf{u})_{l;t}^{(n)} = \sum_{l'=-L}^L \sum_{m'=1}^M \hat{I}_t^{\text{tm}} \hat{S}_{l',m';l;t}^{(n)} u_{l',m'}^{(n)} m' \Delta x_1 \Delta r \Delta r, \quad (4.88)$$

in which

$$u_{l',m'}^{(n)} = \delta \varepsilon_{l',m'}^{(n)}. \quad (4.89)$$

The norm on $\mathbb{D}^{\text{src}}, \Omega$ is defined as

$$\begin{aligned} \|\mathbf{r}\|_{\mathbb{D}^{\text{src}}, \Omega}^2 &= \langle \mathbf{r}, \mathbf{r} \rangle_{\mathbb{D}^{\text{src}}, \Omega} \\ &= \sum_{l=1}^{L'} \sum_{n=-\frac{N}{2}+1}^{\frac{N}{2}} \sum_{t=1}^T r_{l;t}^{(n)} \left(r_{l;t}^{(n)} \right)^* \Delta x_1 \Delta \omega, \end{aligned} \quad (4.90)$$

Table 4.2: Conjugate gradient iteration scheme

$$\begin{aligned}
u_0 &= 0, \quad w_0 = 0, \quad r_0 = f, \\
u_n &= u_{n-1} + \alpha_n w_n, & w_n &= L^H r_{n-1} + \frac{\|L^H r_{n-1}\|_{\mathbb{S}}^2}{\|L^H r_{n-2}\|_{\mathbb{S}}^2} w_{n-1}, \\
r_n &= r_{n-1} - \alpha_n L w_n, & \alpha_n &= \frac{\|L^H r_{n-1}\|_{\mathbb{S}}^2}{\|L w_n\|_{\mathbb{S}}^2},
\end{aligned}$$

where r is defined in the space \mathbb{D}^{src} and will be specified later, and where Ω denotes the temporal Fourier domain. The norm of a vector u , defined in the space \mathbb{D} , reads

$$\begin{aligned}
\|u\|_{\mathbb{D}}^2 &= \langle u, u \rangle_{\mathbb{D}} \\
&= \sum_{l'=-L}^L \sum_{m'=1}^M \sum_{n=-\frac{N}{2}+1}^{\frac{N}{2}} u_{l',m'}^{(n)} \left(u_{l',m'}^{(n)} \right)^* m' \Delta x_1 \Delta r \Delta r. \quad (4.91)
\end{aligned}$$

The adjoint of the operator L is defined through the inner product, hence

$$\langle Lu, r \rangle_{\mathbb{D}^{\text{src}}, \Omega} = \langle u, L^H r \rangle_{\mathbb{D}}, \quad (4.92)$$

where the symbol “ H ” is used to denote that the adjoint is taken. Note that the inner product depends on the space in which the operator is defined.

Using the definition of the inner product from equation (4.92) and of the norm from equation (4.90), we obtain the adjoint operator L^H via

$$\begin{aligned}
\langle Lu, r \rangle_{\mathbb{D}^{\text{src}}, \Omega} &= \sum_{l=1}^{L'} \sum_{n=-\frac{N}{2}+1}^{\frac{N}{2}} \sum_{t=1}^T (Lu)_{l;t}^{(n)} \left(r_{l;t}^{(n)} \right)^* \Delta x_1 \Delta \omega \\
&= \sum_{l=1}^{L'} \sum_{n=-\frac{N}{2}+1}^{\frac{N}{2}} \sum_{t=1}^T \left(\sum_{l'=-L}^L \sum_{m'=1}^M \left(\hat{I}_t^{\text{tm}} \hat{S}_{l',m';l;t}^{(n)} \right)^* m' \Delta x_1 \Delta r \Delta r \right)^* \\
&\quad u_{l',m'}^{(n)} \left(r_{l;t}^{(n)} \right)^* \Delta x_1 \Delta \omega \\
&= \sum_{l'=-L}^L \sum_{m'=1}^M \sum_{n=-\frac{N}{2}+1}^{\frac{N}{2}} u_{l',m'}^{(n)} \left((L^H r)_{l',m'}^{(n)} \right)^* m' \Delta x_1 \Delta r \Delta r \\
&= \langle u, L^H r \rangle_{\mathbb{D}},
\end{aligned}$$

where

$$(\mathbf{L}^H \mathbf{r})_{l',m'}^{(n)} = \sum_{l=1}^{L'} \sum_{t=1}^T \left(\hat{f}_t^{\text{tm}} \hat{S}_{l',m';l;t}^{(n)} \right)^* r_{l;t}^{(n)} \Delta x_1 \Delta \omega . \quad (4.93)$$

Finally, we define a normalized error ERR which will be minimized, viz.

$$\text{ERR} = \frac{\|r\|_{\mathbb{D}^{\text{src}},\Omega}^2}{\|f\|_{\mathbb{D}^{\text{src}},\Omega}^2} , \quad (4.94)$$

where r satisfies

$$\|r\|_{\mathbb{D}^{\text{src}},\Omega}^2 = \|f - \mathbf{L}u\|_{\mathbb{D}^{\text{src}},\Omega}^2 . \quad (4.95)$$

We apply the above results in a standard CG scheme as shown in the diagram in table 4.2, and discussed by Kleinman and Van den Berg (1991). Note that we have to terminate the iterative process after a fixed number of iterations, before it starts blowing up the noise.

4.9 Synthetic and experimental results conjugate gradient method

In this section we will show the results obtained with the conjugate gradient method. The same synthetic and measured data sets are used as discussed previously in section 4.7.

In figure 4.17, we show the normalized error functional for both measured and synthetic data. During the first five iteration steps, both functionals decrease similar. After that, the convergence rate of the conjugate gradient method using measured data diminishes significantly. It is observed that in the first five iterations the two curves coincide and start to deviate after ten iterations. The convergence of error using the measured data decreases dramatically after twenty iterations. Then, the ill-posed nature of the problem starts to manifest. Therefore it is wise to limit the number of iterations to at most ten iterations.

In figures 4.18 and 4.19, the computed contrast after ten iterations is shown in the same planes as used in section 4.7. Exploring the results from the synthetic data set, we observe that the computed contrast of both objects are identical. Note that this was not the case with results obtained from back-propagation! Unfortunately, this is not the case with the measured data. In addition, it shows that the first object at $x_1 = 2$ m is positioned in two planes, at $x_1 = 1.99$ m and at $x_1 = 2.13$ m. This is caused by the measuring method:

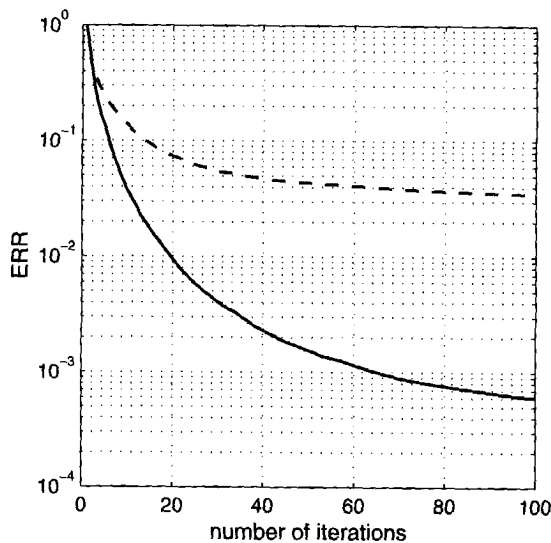


Figure 4.17: The normalized error ERR as a function of the number of iterations. The dashed line are the results using measured data, while the solid line denotes the results using synthetic data.

the antenna system follows the path of a “spiral”, hence each complete rotation takes place over a full range of equidistant x_1 -positions, between two gridpoints. The second object however, is visible over a much longer range in the x_1 -direction, three to five grid points. This is explained by the fact that this object corresponds to the gastank of length 0.3 m.

Finally, we observe in figure 4.19 a blurring effect in the radial direction in the images from the measured data. Firstly, this is caused by the antenna ringing. A second explanation of this blurring effect is the fact that the source current in the inversion is not properly taken. For the measurements, this current is unknown, and consequently we have simply approximated it by a unit current within the actual bandwidth of the frequency domain.

In figure 4.20, we show the results for the plane $x_1 = 1.99$ m after 2, 5, 10, 50 and 100 iterations, respectively. On the left-hand side, results obtained from synthetic data, on the right-hand side from measured data. The results from synthetic data do not show any major changes, such as an increase in resolution. However, for measured data, we observe an increase in the number of maxima visible in the radial direction without gaining any angular resolution. Hence, it is interesting to investigate the maximum resolution, achievable in the angular direction.

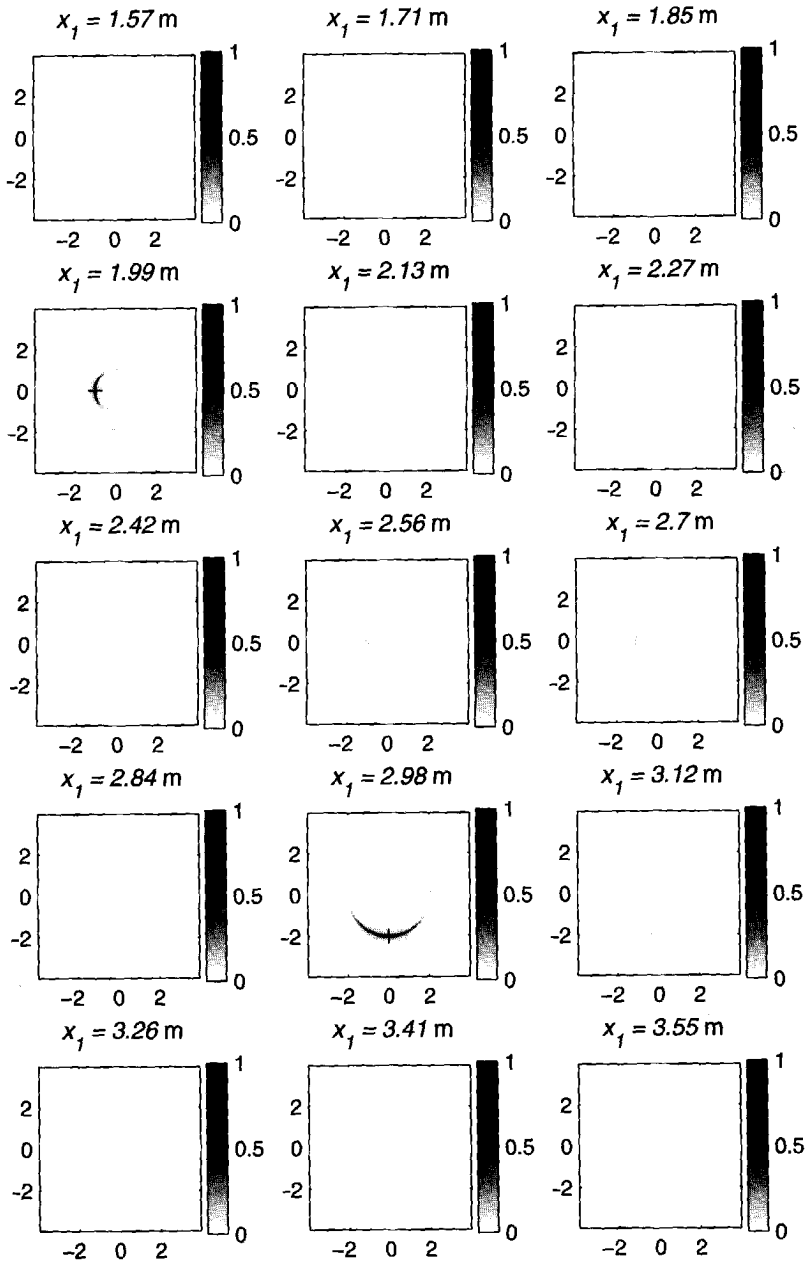


Figure 4.18: The results obtained by applying a conjugate gradient method on synthetic data. Shown is the normalized absolute value of the computed contrast, $|\delta\epsilon(\vec{x})|$, in the planes at various x_1 -positions.

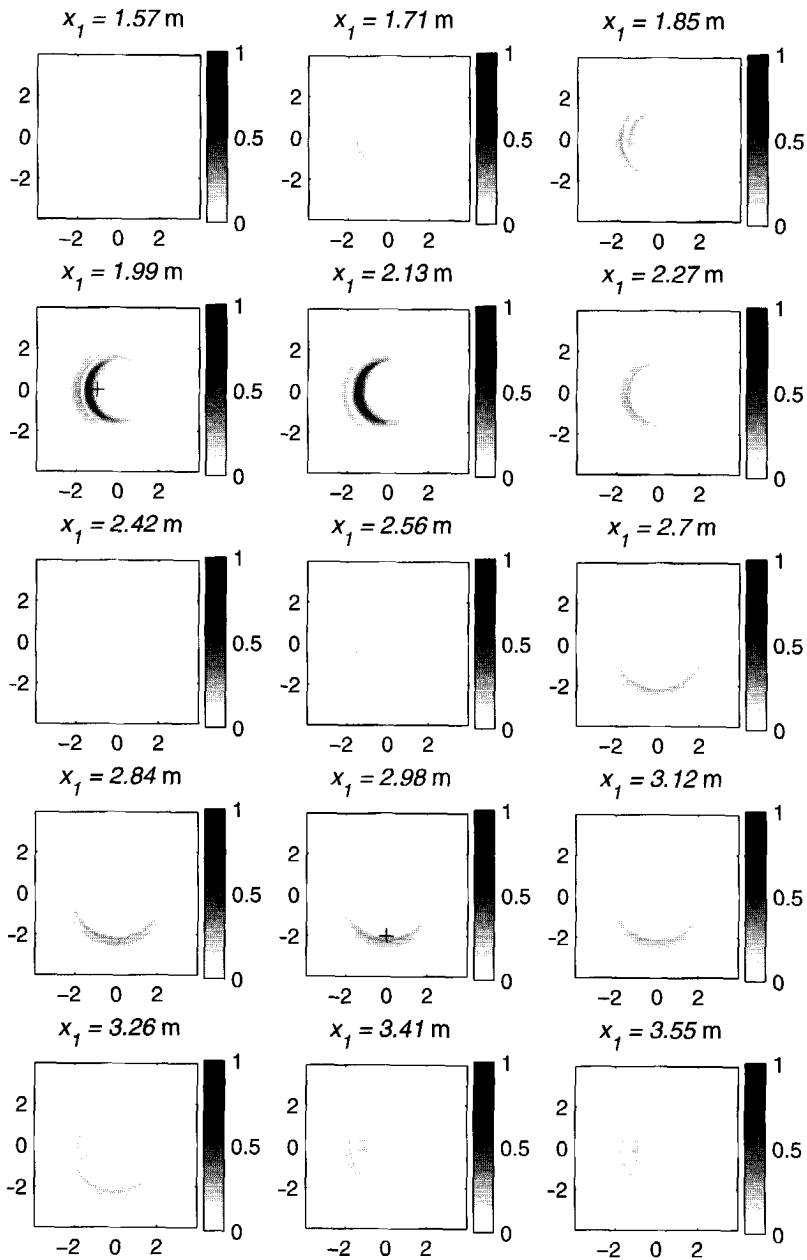


Figure 4.19: The results obtained by applying the conjugate gradient method on measured data. Shown is the normalized absolute value of the computed contrast, $|\delta\epsilon(\vec{x})|$, in the planes at various x_1 -positions.

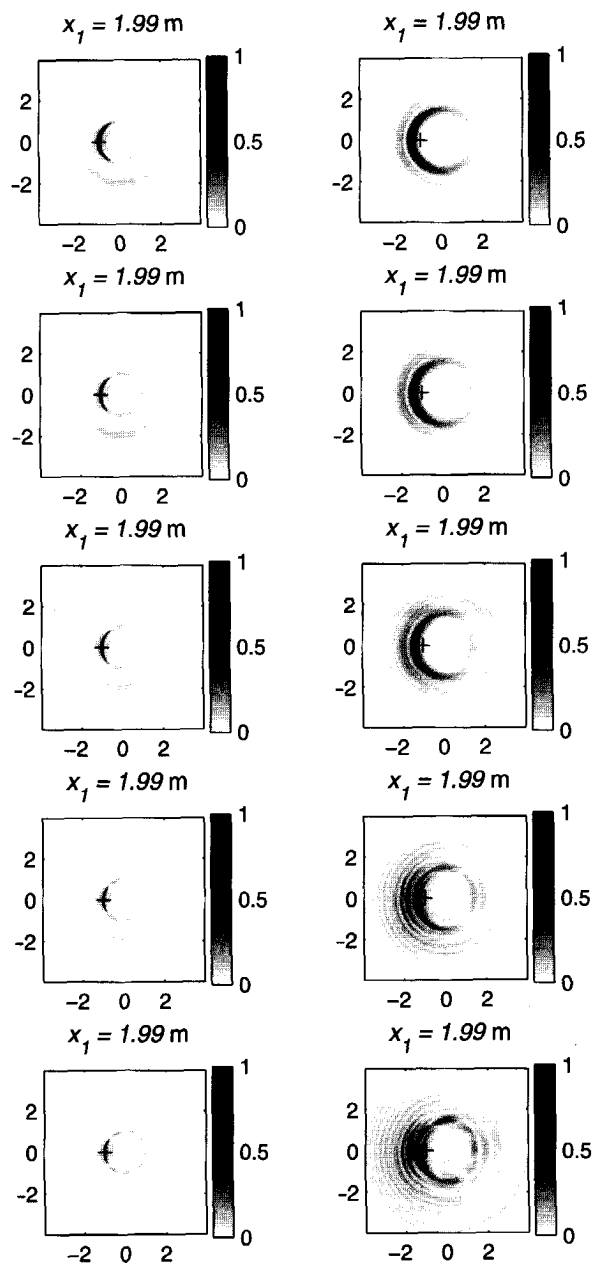


Figure 4.20: The results obtained by applying the conjugate gradient method on both synthetic (left) and measured (right) data, from top to bottom: number of iterations equals 2, 5, 10, 50 and 100.

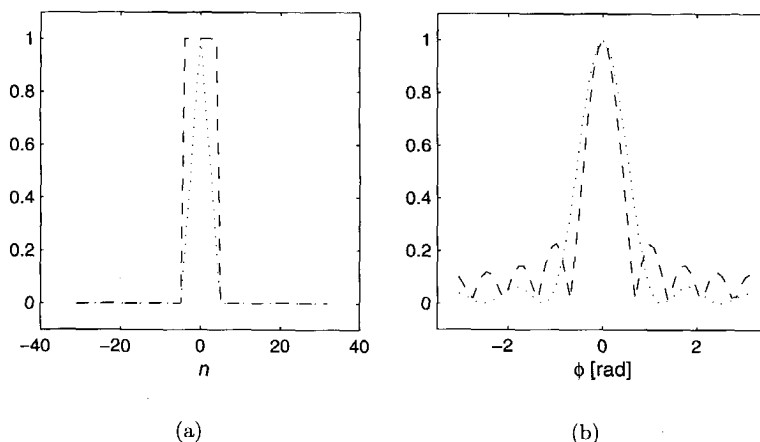


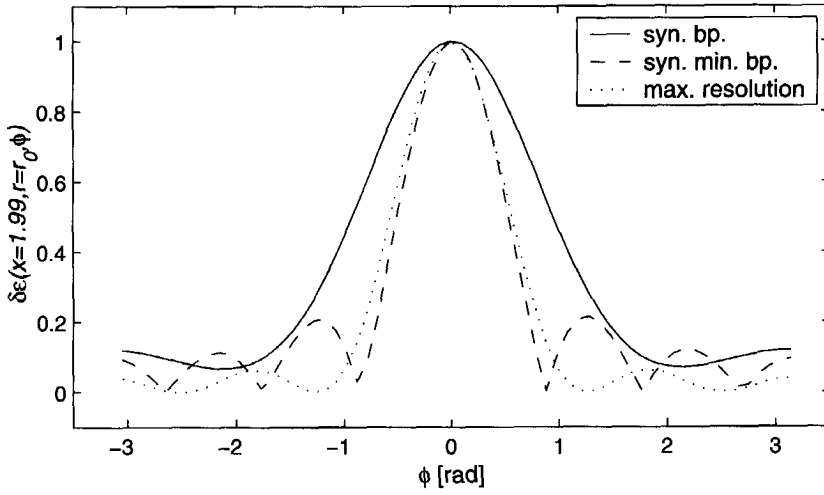
Figure 4.21: A triangular and a box shaped spectrum with its corresponding spatial function.

4.10 Maximum angular resolution

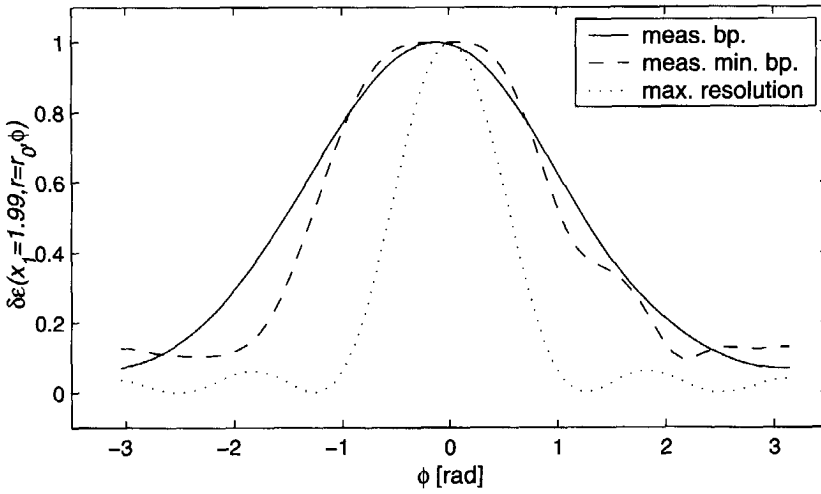
The maximum angular resolution achievable, depends on the number of angular frequency components used in the inversion algorithm. We have shown that the number of significant spatial angular frequency components present in our sensitivity function is nine. To reduce computational time, we only use these nine in our computations. Hence, it is interesting to investigate the consequences of using a limited number of components. Therefore, we compare the results with two angular functions, each defined through nine angular frequency components.

The two angular spatial frequency spectrums are given in figure 4.21(a), where 9 out of 64 angular components are non-zero. One spectrum is triangular shaped, the other one is a rectangular function. Applying a DFT on these spectrums, taking their absolute values, and normalizing them to unity results in the functions shown in figure 4.21(b). The function has either a small main-lobe and large side-lobes, or vice versa.

Next, we compare the obtained angular distributions from the various methods with the above results. In figure 4.22 we show the computed contrast after normalization, obtained with back-propagation, at $x_1 = 1.99$ m, and at the radial distance r_0 where the maximum amplitude of the contrast is positioned. With synthetic data, figure 4.22(a), we clearly observe an increase in angular resolution obtained with minimized back-propagation. The method even approaches the resolution obtained with the triangular shaped frequency distribution. With measured data however, the resolution obtained is not as

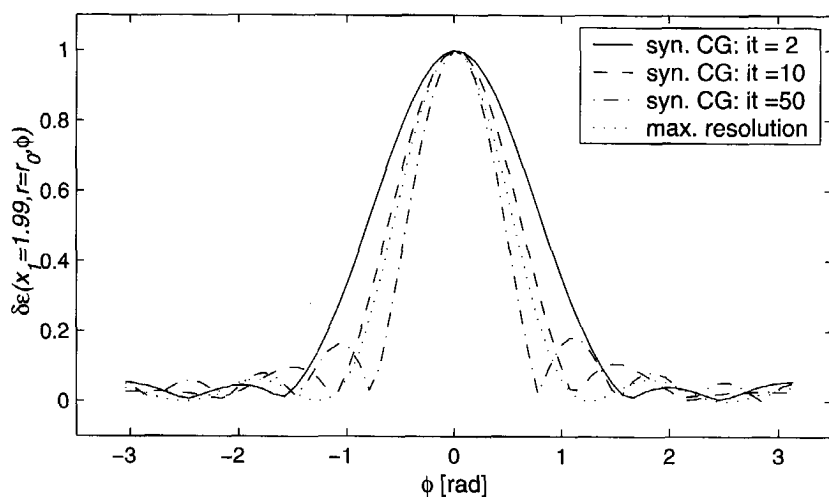


(a)

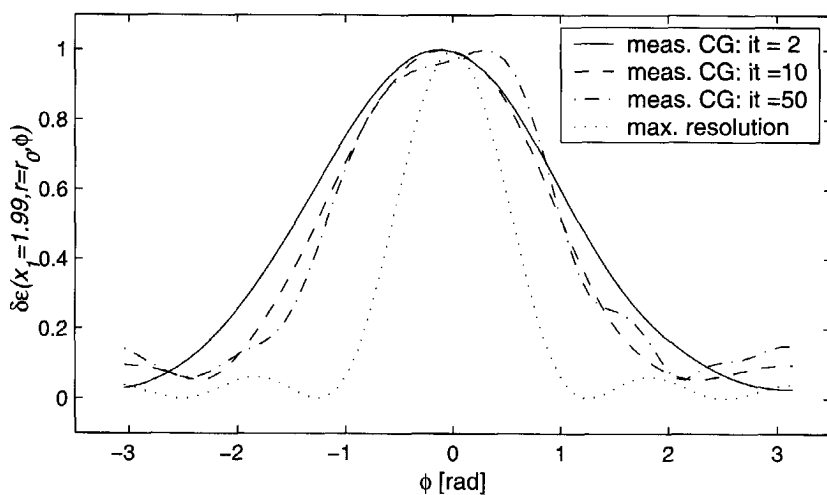


(b)

Figure 4.22: The normalization computed contrast based on standard (solid line) and minimized back-propagation (dashed line). The dotted line denotes the maximal achievable resolution obtained from the triangular shaped frequency spectrum.



(a)



(b)

Figure 4.23: The normalization computed contrast based on conjugate gradient for two (solid line), ten (dashed line) and fifty (dashed-dotted line) iterations, compared with a triangular shaped distribution (dotted line).

good as with the synthetic data and the increase in resolution obtained with minimized back-propagation is only minimal.

Finally, we show the results for the CG method in figure 4.23. With synthetic data, we see that increasing the number of iterations results in a smaller main-lobe. With the measured data however, this process terminates after 10 iterations, and its maximum starts to shift from the center.

4.11 Conclusion

In this chapter we have derived two types of imaging algorithms in order to obtain a three-dimensional image of the subsurface. One type is based on back-propagation, the other one on a conjugate gradient (CG) method. Both types apply a linear inversion on the data using a sensitivity function. The algorithms have been tested on synthetic and measured data.

Exploration of the sensitivity function shows that it can be approximated by an effective one, which combines an angular dependent function with the omni-directional radiation pattern of an electric dipole. Another important property of the (effective) sensitivity function is that it only contains nine significant angular frequency components. Hence, we reduce the computational effort with 85%, by neglecting the remaining components. However, a disadvantage is that the maximum achievable resolution in the angular direction is limited, and that it might result in several side-lobes next to the main-lobe.

Three imaging algorithms are tested, namely standard back-propagation, minimized back-propagation, and a CG inversion method. Both synthetic and measured data have been used. The measured data are obtained in a deep water basin to ensure a homogeneous back-ground medium.

The imaging takes place in the spatial angular and temporal frequency domain, using temporal frequencies in the range 60 – 280 MHz. The back-propagation methods minimizes nine error functionals, one for each angular frequency component, while the CG method minimizes one error functional containing all nine components. It is observed that in case of the CG method, there is hardly any increase in resolution after ten iterations. Good results are obtained, although the quality of the image from the measured data was not as good as from the synthetic data. In the radial direction, this is mainly caused by the improper choice of the electric-source current spectrum in the transmitting dipole antenna. In the angular direction it is explained by the fact that the angular Fourier spectrum is very limited, and thus only 14% of the data are used. Besides, there is a great difference in weighting factors for each component, making it very sensitive for small errors in each weighting factor.

It is expected that the angular resolution can be increased by using an other set of a basis functions, resulting in a wider flat spectrum. Finally, the radiation pattern starts to diverge from the radiation pattern used for the effective one, for temporal frequencies above 160 MHz. Hence, an increase in resolution is expected if for the higher temporal frequencies a different effective sensitivity function is used.

The main advantage of the CG method over (minimized) back-propagation is that the computed contrast is not (less) dependent on the radial distance. Similar results are expected if we combine back-propagation with preconditioning. Although using a preconditioner in an (iterative) solution method incurs some extra cost during the setup (and per iteration), it might improve the convergence speed. A simple, but effective one is the Jacobi or diagonal preconditioner, see e.g. Barrett *et. al.* (1994), where the diagonal of the matrix is used. Hence, we suggest to use $\hat{S}^{(n)}(\vec{v}|\vec{v}') \left(\hat{S}^{(n)}(x_1, r|x'_1) \right)^*$ as preconditioner.

Chapter 5

Conclusions

In this thesis we have shown the successful design of a borehole radar system, which has a directional radiation pattern, sensitive receiving properties, and fits in a single borehole. To ensure enough resolution and penetrating power, the transient generated wavefield has a center frequency of 100 MHz. The maximum diameter of the system does not exceed the 0.09 m. In addition, we have developed various inversion schemes to image the subsurface. Good results are obtained with these schemes, when tested on both synthetic and measured data.

The basis for the design of the system and the imaging algorithms is formed in chapter 2. Here we derived an integral equation using Maxwell equations, the electromagnetic boundary conditions, and the frequency-domain reciprocity theorem. The integral equation describes the interaction between an electric current carrying thin wire as dipole antenna, a perfectly conducting reflector, a scattering object, and the total electric wavefield. The reflector appears in the integral equation as a jump in electric-surface-current density at the reflector domain, where the scattering object is considered as a change in electromagnetic medium parameters. We have assumed that the reflector and the scatterer are decoupled from the dipole, which is equivalent with the Born approximation.

To design the antenna system, in particular the reflector, we simplified the integral equation by omitting the influence of scattering objects on the total electric wavefield. In addition, we formulate the problem in a linear curved coordinate system, since we expected that the reflector should be curved in

the optimum configuration. The integral equation has been solved using a conjugate gradient FFT solution method and the total electric wavefield in space is computed.

The low-frequency content of the wavefield has to be combined with the spatial limitations of the system. We therefore positioned the system in a medium with high permittivity to shorten the wavelength. Based on optical ray theory, we expected that in the ideal configuration the dipole is located in the focal point of a parabolically curved reflector. To validate these expectations we have computed the total electric wavefield for several parabolically curved reflectors, and have shown that the radiation pattern is indeed directional. However, it is observed that the directionality is improved by positioning the dipole to the far opposite of the reflector. Next we have chosen a circularly curved reflector while keeping the position of the dipole at the far opposite of the reflector. This resulted in an increase of directionality. Hence, we conclude that this configuration represented the optimal one.

Based on the optimal configuration, a prototype antenna system has been built. The radiation pattern of this prototype has been measured below the water table. The measured pattern is in excellent agreement with the computed one. In most cases only the borehole is filled with water while the surrounding medium has different electromagnetic properties. This influences the radiation pattern, and might result in a decrease of directionality. This is an interesting subject for future research.

In chapter 3, we have described the antenna configuration as a two port system. We have combined the reciprocity theorem with the integral equation obtained in chapter 2, and have shown that the changes in impedance as observed by the antenna system are the result of a convolution of changes in medium parameters with a sensitivity function. This sensitivity function contains a vectorial description of the radiation characteristics of the antenna system. In addition, it formulates the change in impedance caused by the presence of a unit point-scatterer. This change is observed as a change in voltage at the port of the receiver. The data are measured while the rotating system is pulled through a borehole. To image the subsurface, we need to deconvolve the data for the sensitivity function.

Exploring the sensitivity function revealed us important information. We showed that the radiation pattern is approximately constant over a range of temporal frequencies, $60 \leq f_0 \leq 160$ MHz, and radial distances, from the near-field region up to the far-field region. This enabled us to reduce the computation time and memory by approximating the sensitivity function by an effective one. The effective one is obtained by convolving the omni-directional radiation pattern of an electric dipole, with the pattern of the system at a radial distance of about a wavelength at a temporal frequency of 100 MHz.

Since the system rotates around its axis, we have a convolution in the angular direction. This convolution is computed effectively in the angular Fourier domain. Since only 9 of the 64 angular Fourier components of the sensitivity in the angular Fourier domain have a significant value, a further reduction of computational time is obtained by restricting the computations to these nine Fourier components.

We have developed two types of inversion schemes in the temporal frequency domain. After linearizing the data equation, we either applied a single step back-propagation method or an iterative conjugate gradient (CG) inversion method. The back-propagation method is based on the minimization of a number of error functionals, one for each significant angular Fourier component. If only the update direction is used in the inversion process, we use the term standard back-propagation. If we use in addition the update parameter as well, we refer to it as minimized back-propagation. With the latter method we increased the angular resolution. This minimized back-propagation is similar to the first step in the CG scheme.

All algorithms are tested on synthetic and measured data, and resulted in good three-dimensional characterizations of the subsurface. As expected, the angular resolution obtained with standard back-propagation is increased if the minimized back-propagation method or the CG method is used. With synthetic data, we then achieved the maximum angular resolution possible. This is limited, since the number of significant angular components is limited. We expect to improve the resolution, if we use an other vector space than the angular Laplace domain. In this domain, the spectrum of the sensitivity has to contain more significant components and is preferably flatter.

In the axial and radial directions, all methods give approximately the same resolution. With the CG method, we observed an improvement of the computed amplitudes of the contrasts at larger radial distances.

Based on our results, we propose to combine the minimized back-propagation method with a preconditioner. We expect to improve the amplitude of the computed contrast at larger radial distances. We suggest a simple, but effective preconditioner like the Jacobi or diagonal preconditioner, where the diagonal of the matrix is used.

We conclude that the result of the present research is a new tool which enables us to obtain unique information from out of a borehole. With this information a three-dimensional characterization of the subsurface can be made. This is a completion to current available techniques. The current technique is ideal for the detection of unexploded ordnance, UXO's, and can be applied immediately. Another application is the tunnel industry. There, we can probe the trajectory of a tunnel to be drilled. Finally, the oil- and gas-industry is

worth noting. In order to explore an oil or gas reservoir in an optimal way, it is desirable to have a three-dimensional characterization of the reservoir, or to know its position in reference with a salt dome. It is expected that this tool is capable to detect the bottom and the top of a reservoir.

Appendix A

Orthogonal curvilinear coordinate system

Let us consider the vector $\vec{v} = v_i$ for $i = \{1, 2, 3\}$, containing the set of variables or coordinates of an orthogonal curvilinear coordinate system with unit basis vectors \vec{e}_{v_i} . Examples of orthogonal curvilinear coordinate systems are the circular cylindrical and the parabolical cylindrical coordinate system. Consequently, the vector $\vec{u} = u_{v_i}(\vec{v})$ is defined in the curvilinear coordinate system as a function of the parameters v_j . A vector in the Cartesian coordinate system denoted as $\vec{u} = u_{x_i}(\vec{x})$ is expressed with the parameters x_j , the variables of the Cartesian coordinate system. Therefore, the vector $u_{x_i}(\vec{v})$ is defined in the Cartesian coordinate system where the coordinates x_i are a function f_i of the parameters v_j , viz.

$$x_i = f_i(v_j) . \quad (\text{A.1})$$

Given these functions $f_i(v_j)$, the distance dL between two points \vec{v} and $\vec{v} + d\vec{v}$ satisfy the relation

$$(dL)^2 = h_{v_i}^2 dv_i^2 = (h_{v_1} dv_1)^2 + (h_{v_2} dv_2)^2 + (h_{v_3} dv_3)^2 , \quad (\text{A.2})$$

where h_{v_i} are the Lamé's coefficients. These Lamé coefficients can be understood as scale factors and are defined as

$$\begin{aligned} h_{v_1} &= (\partial_{v_1} x_i \partial_{v_1} x_i)^{\frac{1}{2}} = \left((\partial_{v_1} x_1)^2 + (\partial_{v_1} x_2)^2 + (\partial_{v_1} x_3)^2 \right)^{\frac{1}{2}} , \\ h_{v_2} &= (\partial_{v_2} x_i \partial_{v_2} x_i)^{\frac{1}{2}} = \left((\partial_{v_2} x_1)^2 + (\partial_{v_2} x_2)^2 + (\partial_{v_2} x_3)^2 \right)^{\frac{1}{2}} , \\ h_{v_3} &= (\partial_{v_3} x_i \partial_{v_3} x_i)^{\frac{1}{2}} = \left((\partial_{v_3} x_1)^2 + (\partial_{v_3} x_2)^2 + (\partial_{v_3} x_3)^2 \right)^{\frac{1}{2}} , \end{aligned} \quad (\text{A.3})$$

where we use Einstein's summation convention for repeated indices. Using these scale factors, we can write the vector displacement $d\vec{v}$ as

$$d\vec{v} = h_{v_i} dv_i \vec{e}_{v_i} = h_{v_1} dv_1 \vec{e}_{v_1} + h_{v_2} dv_2 \vec{e}_{v_2} + h_{v_3} dv_3 \vec{e}_{v_3} . \quad (\text{A.4})$$

For an oriented surface $d\vec{\mathcal{A}}$ in the orthogonal curvilinear coordinate system this results in

$$d\vec{\mathcal{A}} = h_{v_2} h_{v_3} dv_2 dv_3 \vec{e}_{v_1} + h_{v_1} h_{v_3} dv_1 dv_3 \vec{e}_{v_2} + h_{v_1} h_{v_2} dv_1 dv_2 \vec{e}_{v_3} , \quad (\text{A.5})$$

and for a volume element dV in

$$dV = h_{v_1} h_{v_2} h_{v_3} dv_1 dv_2 dv_3 . \quad (\text{A.6})$$

The following vector operators can be expressed in terms of the general orthogonal coordinates: the gradient (∇f), the divergence ($\nabla \cdot \vec{B}$), the rotation ($\nabla \times \vec{B}$) and the gradient-divergence ($\nabla \nabla \cdot \vec{B}$), viz.

$$\nabla f = \frac{\vec{e}_{v_i}}{h_{v_i}} \partial_{v_i} f = \frac{\vec{e}_{v_1}}{h_{v_1}} \partial_{v_1} f + \frac{\vec{e}_{v_2}}{h_{v_2}} \partial_{v_2} f + \frac{\vec{e}_{v_3}}{h_{v_3}} \partial_{v_3} f , \quad (\text{A.7})$$

$$\begin{aligned} \nabla \cdot \vec{B} &= \frac{1}{h_{v_1} h_{v_2} h_{v_3}} \partial_{v_1} (h_{v_2} h_{v_3} B_{v_1}) \\ &+ \frac{1}{h_{v_1} h_{v_2} h_{v_3}} \partial_{v_2} (h_{v_1} h_{v_3} B_{v_2}) \\ &+ \frac{1}{h_{v_1} h_{v_2} h_{v_3}} \partial_{v_3} (h_{v_1} h_{v_2} B_{v_3}) , \end{aligned} \quad (\text{A.8})$$

$$\nabla \times \vec{B} = \frac{1}{h_{v_1} h_{v_2} h_{v_3}} \begin{vmatrix} h_{v_1} \vec{e}_{v_1} & h_{v_2} \vec{e}_{v_2} & h_{v_3} \vec{e}_{v_3} \\ \partial_{v_1} & \partial_{v_2} & \partial_{v_3} \\ h_{v_1} B_{v_1} & h_{v_2} B_{v_2} & h_{v_3} B_{v_3} \end{vmatrix} , \quad (\text{A.9})$$

$$\nabla \nabla \cdot \vec{B} = \begin{pmatrix} \frac{1}{h_1} \partial_1 \frac{1}{h'} \partial_1 (h_{2,3} B_{v_1}) & \frac{1}{h_1} \partial_1 \frac{1}{h'} \partial_2 (h_{1,3} B_{v_2}) & \frac{1}{h_1} \partial_1 \frac{1}{h'} \partial_3 (h_{1,2} B_{v_3}) \\ \frac{1}{h_2} \partial_2 \frac{1}{h'} \partial_1 (h_{2,3} B_{v_1}) & \frac{1}{h_2} \partial_2 \frac{1}{h'} \partial_2 (h_{1,3} B_{v_2}) & \frac{1}{h_2} \partial_2 \frac{1}{h'} \partial_3 (h_{1,2} B_{v_3}) \\ \frac{1}{h_3} \partial_3 \frac{1}{h'} \partial_1 (h_{2,3} B_{v_1}) & \frac{1}{h_3} \partial_3 \frac{1}{h'} \partial_2 (h_{1,3} B_{v_2}) & \frac{1}{h_3} \partial_3 \frac{1}{h'} \partial_3 (h_{1,2} B_{v_3}) \end{pmatrix} , \quad (\text{A.10})$$

where $h' = h_{v_1} h_{v_2} h_{v_3}$, where $h_{i,j} = h_{v_i} h_{v_j}$ and where $h_i = h_{v_i}$.

A vector defined in the curvilinear coordinate system and expressed as a function of the curvilinear coordinates, $\vec{u}_{v_i}(\vec{v})$, can be transformed to a vector

in the Cartesian coordinate system, $\vec{u}_{x_i}(\vec{v})$. The correspondence between both vectors is given through the relation

$$u_{x_i}(\vec{v}) = T_{i,j} u_{v_j}(\vec{v}) , \quad (\text{A.11})$$

where T is the coordinate transformation matrix and satisfies

$$T = \begin{pmatrix} \frac{1}{h_{v_1}} \partial_{v_1} x_1 & \frac{1}{h_{v_2}} \partial_{v_2} x_1 & \frac{1}{h_{v_3}} \partial_{v_3} x_1 \\ \frac{1}{h_{v_1}} \partial_{v_1} x_2 & \frac{1}{h_{v_2}} \partial_{v_2} x_2 & \frac{1}{h_{v_3}} \partial_{v_3} x_2 \\ \frac{1}{h_{v_1}} \partial_{v_1} x_3 & \frac{1}{h_{v_2}} \partial_{v_2} x_3 & \frac{1}{h_{v_3}} \partial_{v_3} x_3 \end{pmatrix} . \quad (\text{A.12})$$

For the transformation backwards the inverse of the operator T , T^{-1} , is used, viz.

$$u_{v_j}(\vec{v}) = T_{j,i}^{-1} u_{v_i}(\vec{v}) , \quad (\text{A.13})$$

In those cases where the matrices T and T^{-1} define an orthonormal transformation, the inverse of T is obtained by taking its transpose, hence

$$T_{j,i}^{-1} = (T^t)_{j,i} , \quad (\text{A.14})$$

where the superscript t denotes the transpose of the matrix is taken.

A.1 Cylindrical coordinate system

In a cylindrical coordinate system the relationship between the parameters x_i and v_j is given by the function $f_i(v_j)$, which reads

$$\{x_1, x_2, x_3\} = \{v_1, v_2 \cos v_3, v_2 \sin v_3\} . \quad (\text{A.15})$$

Taking the coordinate v_2 constant, a circular cylindrically curved plane in a Cartesian coordinate system is obtained, see figure A.1.

From equations (A.2)-(A.8), (A.12) and (A.14) the following set of equa-

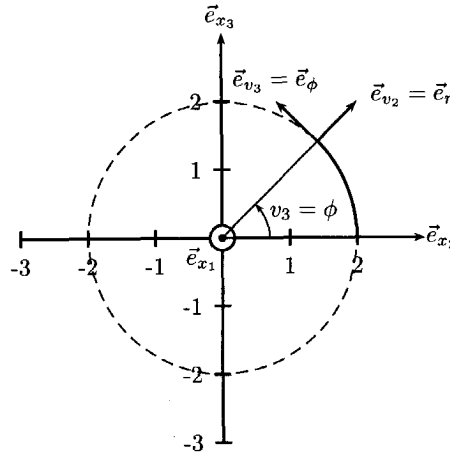


Figure A.1: Cylindrical curved plane for $v_2 = 2$ and $v_3 = [0, \frac{1}{4}\pi]$ in the Cartesian coordinate system with unit basis vectors \vec{e}_{x_i} . The unit vectors \vec{e}_{v_i} form a basis for the cylindrical coordinate system.

tions can be obtained:

$$\{h_{v_1}, h_{v_2}, h_{v_3}\} = \{1, 1, v_2\} , \quad (\text{A.16})$$

$$(dL)^2 = (dv_1)^2 + (dv_2)^2 + r^2(dv_3)^2 , \quad (\text{A.17})$$

$$d\vec{v} = dv_1\vec{e}_{v_1} + dv_2\vec{e}_{v_2} + r dv_3\vec{e}_{v_3} , \quad (\text{A.18})$$

$$d\vec{A} = v_2 dv_2 dv_3 \vec{e}_{v_1} + v_2 dv_1 dv_3 \vec{e}_{v_2} + dv_1 dv_2 \vec{e}_{v_3} , \quad (\text{A.19})$$

$$dV = v_2 dv_1 dv_2 dv_3 , \quad (\text{A.20})$$

$$\nabla f = \partial_{v_1} f \vec{e}_{v_1} + \partial_{v_2} f \vec{e}_{v_2} + \frac{1}{v_2} \partial_{v_3} f \vec{e}_{v_3} , \quad (\text{A.21})$$

$$\nabla \cdot \vec{B} = \partial_{v_1} B_{v_1} + \frac{1}{v_2} \partial_{v_2} (v_2 B_{v_2}) + \frac{1}{v_2} \partial_{v_3} B_{v_3} , \quad (\text{A.22})$$

$$\begin{aligned} \nabla \nabla \cdot \vec{B} = & \left[\partial_{v_1}^2 B_{v_1} + \frac{1}{v_2} \partial_{v_1} \partial_{v_2} (v_2 B_{v_2}) + \frac{1}{v_2} \partial_{v_1} \partial_{v_3} B_{v_3} \right] \vec{e}_{v_1} \\ & + \left[\partial_{v_2} \partial_{v_1} B_{v_1} + \partial_{v_2} \left(\frac{1}{v_2} \partial_{v_2} (v_2 B_{v_2}) \right) + \partial_{v_2} \left(\frac{1}{v_2} \partial_{v_3} B_{v_3} \right) \right] \vec{e}_{v_2} \\ & + \left[\frac{1}{v_2} \partial_{v_3} \partial_{v_1} B_{v_1} + \frac{1}{v_2^2} \partial_{v_3} \partial_{v_2} (v_2 B_{v_2}) + \frac{1}{v_2^2} \partial_{v_3}^2 B_{v_3} \right] \vec{e}_{v_3} , \end{aligned} \quad (\text{A.23})$$

$$T_{i,j} = T_{v_j \rightarrow x_i} = \begin{pmatrix} 1 & 0 & 0 \\ 0 & \cos v_3 & -\sin v_3 \\ 0 & \sin v_3 & \cos v_3 \end{pmatrix} , \quad (\text{A.24})$$

$$T_{j,i}^{-1} = T_{x_i \rightarrow v_j} = \begin{pmatrix} 1 & 0 & 0 \\ 0 & \cos v_3 & \sin v_3 \\ 0 & -\sin v_3 & \cos v_3 \end{pmatrix} . \quad (\text{A.25})$$

In order to increase the readability, we sometimes replace the circular cylindrical coordinate parameters $\{v_1, v_2, v_3\}$ with $\{x_1, r, \phi\}$.

A.2 Parabolical coordinate system

In a parabolic coordinate system the relationship between the parameters x_i and v_j is given by the function $f_i(v_j)$, which reads

$$\{x_1, x_2, x_3\} = \left\{ v_1, \frac{1}{2} (v_2^2 - v_3^2), v_2 v_3 \right\} . \quad (\text{A.26})$$

Parabolic curved planes are obtained by taking v_2 or v_3 constant, see figure A.2.

From equations (A.2)-(A.8), (A.12) and (A.14) the following set of equations can be obtained:

$$(h_{v_1}, h_{v_2}, h_{v_3}) = (1, h, h) , \quad (\text{A.27})$$

$$(dL)^2 = (dv_1)^2 + (h dv_2)^2 + (h dv_3)^2 , \quad (\text{A.28})$$

$$d\vec{v} = dv_1 \vec{e}_{v_1} + h dv_2 \vec{e}_{v_2} + h dv_3 \vec{e}_{v_3} , \quad (\text{A.29})$$

$$d\vec{A} = h^2 dv_2 dv_3 \vec{e}_{v_1} + h dv_1 dv_3 \vec{e}_{v_2} + h dv_1 dv_2 \vec{e}_{v_3} , \quad (\text{A.30})$$

$$dV = h^2 dv_1 dv_2 dv_3 , \quad (\text{A.31})$$

$$\nabla f = \partial_{v_1} f \vec{e}_{v_1} + \frac{1}{h} \partial_{v_2} f \vec{e}_{v_2} + \frac{1}{h} \partial_{v_3} f \vec{e}_{v_3} , \quad (\text{A.32})$$

$$\nabla \cdot \vec{B} = \partial_x B_{v_1} + \frac{1}{h^2} \partial_{v_2} (h B_{v_2}) + \frac{1}{h^2} \partial_{v_3} (h B_{v_3}) , \quad (\text{A.33})$$

$$\begin{aligned} \nabla \nabla \cdot \vec{B} = & \left[\partial_x^2 B_{v_1} + \frac{1}{h^2} \partial_{v_1} \partial_{v_2} (h B_{v_2}) + \frac{1}{h^2} \partial_{v_1} \partial_{v_3} (h B_{v_3}) \right] \vec{e}_{v_1} \\ & + \left[\frac{1}{h} \partial_{v_2} \partial_{v_1} B_{v_1} + \frac{1}{h} \partial_{v_2} \left(\frac{1}{h^2} \partial_{v_2} (h B_{v_2}) \right) + \frac{1}{h} \partial_{v_2} \left(\frac{1}{h^2} \partial_{v_3} (h B_{v_3}) \right) \right] \vec{e}_{v_2} \\ & + \left[\frac{1}{h} \partial_{v_3} \partial_{v_1} B_{v_1} + \frac{1}{h} \partial_{v_3} \left(\frac{1}{h^2} \partial_{v_2} (h B_{v_2}) \right) + \frac{1}{h} \partial_{v_3} \left(\frac{1}{h^2} \partial_{v_3} (h B_{v_3}) \right) \right] \vec{e}_{v_3} , \end{aligned} \quad (\text{A.34})$$

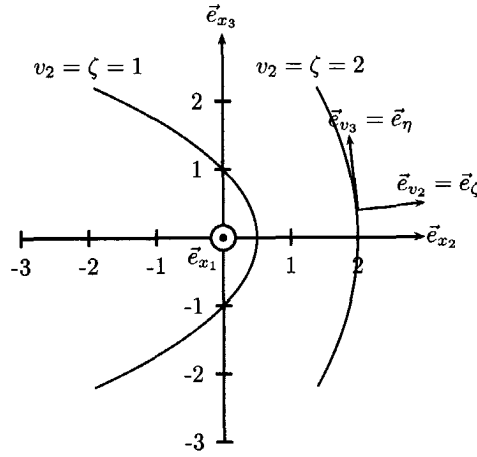


Figure A.2: Parabolic curved planes for $v_2 = \{1, 2\}$ in a Cartesian coordinate system. The unit vectors \vec{e}_{v_i} form a basis for the parabolical system.

$$T_{i,j} = T_{v_j \rightarrow x_i} = \begin{pmatrix} 1 & 0 & 0 \\ 0 & \frac{v_2}{h} & -\frac{v_3}{h} \\ 0 & \frac{v_3}{h} & \frac{v_2}{h} \end{pmatrix}, \quad (\text{A.35})$$

$$T_{j,i}^{-1} = T_{x_i \rightarrow v_j} = \begin{pmatrix} 1 & 0 & 0 \\ 0 & \frac{v_2}{h} & \frac{v_3}{h} \\ 0 & -\frac{v_3}{h} & \frac{v_2}{h} \end{pmatrix}, \quad (\text{A.36})$$

where $h = (v_2^2 + v_3^2)^{\frac{1}{2}}$. In order to increase the readability, we sometimes replace the parabolic cylindrical coordinate parameters $\{v_1, v_2, v_3\}$ with $\{x_1, \zeta, \eta\}$.

Bibliography

- Abramowitz, M., and Stegun, I.A., *Handbook of Mathematical Functions*, 9 ed., Dover Publications, New York, 1970.
- Anderson, B.I., *Modeling the Inversion Methods for the Interpretation of Resistivity Logging Tool Response*, PhD thesis, Delft University, Delft, The Netherlands, 2001.
- Balanis, C.B., *Antenna Theory, Analysis and Design*, 2 ed., John Wiley & Sons, New York, 1997.
- Barrett, R., Berry, M., Chan, T.F., Demmel, J., Donato, J., Dongarra, J., Eijkhout, V., Pozo, R., Romine, C., and Van der Vorst, H., *Templates for the Solution of Linear Systems: Building Blocks for Iterative Methods*, SIAM, Philadelphia, 1994.
- Carsione, J.M., and Schoenberg, M.A., "3-D ground-penetrating radar simulation and plane-wave theory in anisotropic media", *Geophysics* **65** (2000), no. 5, pp. 1527-1541.
- Chignell, R.J., Jackson, P.A., and Madani, K., "Early developments in ground-probing radar at ERA Technology Ltd.", *IEE Proceedings* **135** (1988), Part F, pp. 362-370.
- De Hoop, A.T., *Handbook of Radiation and Scattering of Waves*, Academic Press, London, 1995.
- Dyck, A.V., "Electric borehole methods applied to metallic mineral prospecting", *Geological Survey of Canada Paper* **75** (1975), no. 31, pp. 13-29.
- Dyck, A.V., and Young, R.P., "Physical characterization of rock masses using borehole methods", *Geophysics* **50** (1985), no. 12, pp. 2530-2541.
- Hestenes, M.R., "Iterative methods for solving linear equations", published in

- NAML Report 52-9 (1951), National Bureau of Standards, Los Angeles, CA, reprinted in *Journal of Optimization Theory* 11 (1973), pp. 323-334.
- Hestenes, M.R., and Stiefel, E., "The conjugate-gradient method for solving linear problems", *Journal of Research of the National Bureau of Standards* 49 (1952), pp. 409-435.
- Hülsmeier, C., "Hertzian-wave Projecting and Receiving Apparatus Adapted to Indicate or Give Warning of the Presence of a Metallic Body, Such as a Ship or a Train, in the Line of Projection of Such Waves", British patent 13, 170, September 22, 1904.
- Jones, D.S., *The Theory of Electromagnetism*, vol. 47, Pergamon Press, Oxford, 1964.
- Kleinman, R.E., and Van den Berg, P.M., *Iterative methods for solving integral equations*, Application of Conjugate Gradient Method to Electromagnetic and Signal Analysis (T.K. Sarkar, ed.), PIER 5, Elsevier, New York, 1991, pp. 67-102.
- Maxwell, J.C., *Treatise on Electricity and Magnetism*, Clarendon Press, Oxford, 1873.
- Olhoeft, G.R., "Application of ground penetrating radar", *Proceedings of the Sixth International Conference on Ground Penetrating Radar (GPR 1996)*, Department of Geoscience & Technology, Tohoku University, Sendai, Japan, September 30 - October 3, 1996.
- Salazar-Palma, M., Sarkar, T.K., and Sengupta, D., "A chronology of developments of wireless communications and electronics from 1921-1940", *2001 IEEE Antennas & Propagation Society International Symposium (Boston, MA)*, vol. 1, IEEE Antennas & Propagation Society, USNC/URSI National Radio Science Meeting, July 2001, pp. 6-9.
- Sarkar, T.K., Salazar-Palma, M., and Sengupta, D., "A chronology of developments of wireless communications and electronics from 1831-1920", *2001 IEEE Antennas & Propagation Society International Symposium (Boston, MA)*, vol. 1, IEEE Antennas & Propagation Society, USNC/URSI National Radio Science Meeting, July 2001, pp. 2-5.
- Sengupta, D.L., and Sarkar, T.K., "Maxwell, Hertz, the Maxwellians and the early history of electromagnetic waves", *2001 IEEE Antennas & Propagation Society International Symposium (Boston, MA)*, vol. 1, IEEE Antennas & Propagation Society, USNC/URSI National Radio Science Meeting, July 2001, pp. 14-17.
- Skolnik, M.I., *Introduction to Radar Systems*, international ed., Electrical Engineering Series, McGraw-Hill, 1981.
- Stern, W., "Versuch einer elektrodynamischen Dickenmessung von Gletschereis", *Gerlands Beitrage Zur Geophysik* 23 (1929), pp. 292-333.

- Stiefel, E.S., "Über einige Methoden der Relaxationsrechnung", *Zeitschrift für angewandte Mathematik und Physik (Journal of Applied Mathematics and Physics)* **29** (1951), pp. 157-179.
- Lord Rayleigh (Strutt, J.W.), *Theory of Sound*, Macmillan, London, 2 ed. Dover, 1945.
- Van den Berg, P.M., Scattering and inverse scattering in pure and applied science, *Scattering* (Pike, R., and Sabatier, P., eds.), vol. 2, Academic Press, London, 2002, pp. 142-161.
- Whittaker, E.T., *Vol. 1, The Classical Theories* (1910, revised and enlarged in 1951), *Vol. 2, The Modern Theories 1900-1926* (1953), *A History of the Theories of Aether and Electricity*, Nelson, London, reprinted by Harper Torchbooks, New York, 1960.
- Zwamborn, A.P.M., *Scattering by Objects with Electric Contrast*, PhD thesis, Delft University, Delft, The Netherlands, 1991.
- Zwamborn, A.P.M., and Van den Berg, P.M., "A weak form of the conjugate gradient FFT method for plate problems", *IEEE Transactions on Antennas and Propagation* **39** (1991), 224-228.
- Zwamborn, A.P.M., and Van den Berg, P.M., "A weak form of the conjugate gradient FFT method for two-dimensional TE scattering problems", *IEEE Transactions on Microwave Theory and Techniques* **39** (1991), pp. 953-960.

Samenvatting

Een boorgatradarsysteem met een richtingsafhankelijke gevoeligheid voor visualisatie van de bodem

door Koen Willem Anton van Dongen

Gedurende een periode van vier jaar is een nieuw radarsysteem ontworpen. Vernieuwend aan het systeem is de combinatie van richtingsafhankelijke gevoeligheid met een groot doordringend vermogen. Dit systeem is hierdoor in staat de ondergrond vanuit het boorgat drie-dimensionaal te karakteriseren. Mogelijke toepassingen zijn het opsporen van blindgangers, het meten van de diameter van betonnen kolommen, of de verkenning van het traject van een te boren tunnel. Zowel berekeningen als metingen laten zien dat het systeem in één richting zeer gevoelig is. De algoritmes voor het karakteriseren van de ondergrond zijn getest op synthetische en gemeten data. De resultaten laten zien dat het systeem goed in staat is om objecten in de ondergrond op te sporen.

Elektromagnetische golven weerkaatsen op overgangen tussen materialen met verschillende elektromagnetische eigenschappen. Hierbij geldt dat de mate van verschil bepalend is voor de mate van reflectie. Een systeem dat in staat is elektromagnetische golven uit te zenden, gereflecteerde golven waar te nemen, en de tijdsverschillen tussen zenden en ontvangen te bepalen wordt een radar (radio detection and ranging) genoemd. Omdat het doordringend vermogen van de golven in de ondergrond beperkt is, ontstaan er problemen bij het toepassen

van deze techniek voor het lokaliseren van diep in de aardkorst gelegen scheuren en lagen. Dit wordt opgelost door een gat te boren naar dit gebied en van daaruit metingen te verrichten. Om een drie-dimensionaal beeld van de ondergrond te krijgen moet het radarsysteem een richtingsafhankelijke gevoeligheid hebben. Dit kan worden verkregen door in één richting uit te zenden, door te meten waar een reflectie vandaan komt of door een combinatie van beide. Gedurende de afgelopen decennia zijn verscheidene boorgat-systemen gemaakt waarbij de gevoeligheid richtingsafhankelijk is. Helaas gaat dit vaak ten koste van het doordringend vermogen. Om dit verlies te voorkomen maken wij gebruik van een elektrische dipoolantenne die in één richting is afgeschermd met een cilindrisch gebogen metalen reflector.

Om voldoende doordringend vermogen en resolutie te hebben moeten de frequentie-componenten van het golfveld rondom de centrale frequentie van 100 MHz liggen. De maximale diameter van het antennesysteem mag echter niet groter zijn dan 0.10 m. Hierdoor is de diameter van de beschikbare ruimte voor een met water gevuld boorgat slechts $1/3$ golflengte.

Om de optimale antenneconfiguratie te vinden en om in een later stadium de gemeten data te kunnen interpreteren wordt in dit proefschrift eerst een complete formulering van het probleem gemaakt. Hierbij wordt het totale elektrische veld beschreven dat veroorzaakt wordt door een dipoolantenne, in aanwezigheid van een perfect geleidende metalen reflector en een object. Daarbij wordt gebruik gemaakt van het reciprociteitstheorema. Dit theorema stelt ons in staat om twee verschillende toestanden, waarin een gegeven ruimtelijk domein zich in een gegeven tijdspanne zou kunnen bevinden, met elkaar in relatie te brengen.

Om de vorm van de metalen reflector te bepalen wordt het reflectieprobleem opgelost, waarbij de invloed van het object wordt verwaarloosd. Het resultaat is een integraalvergelijking, die het elektrisch veld beschrijft zoals dat door een elektrische dipoolantenne wordt gevormd in aanwezigheid van een perfect geleidende plaat. De dipoolantenne wordt beschreven door een bekende elektrische lijnstroom. Het veld dat reflecteert op de reflector wordt beschreven door een onbekende stroomverdeling op de plaats van de plaat. Doordat de cilindrische plaat zowel cirkelvormig als parabolisch gebogen kan zijn, wordt de vergelijking uitgedrukt in een coördinatensysteem dat in twee dimensies is gekromd. Met behulp van een geconjugeerde gradiëntenmethode wordt de vergelijking opgelost voor verschillende configuraties. Uit de berekeningen blijkt dat in de optimale configuratie de plaat cirkelvormig is gebogen over 143° . Tevens laten de berekeningen zien dat door de reflector de veldsterkte ruim 1.6 keer zo groot wordt in het punt op vijf meter afstand van de dipool, in het vlak door het midden van, en opgespannen door de dipool. Gebaseerd op dit ontwerp is een prototype gemaakt, waarvan het stralingspatroon is gemeten.

Dit patroon komt goed overeen met de berekeningen.

Om de ondergrond te karakteriseren wordt ditmaal de invloed van het object meegenomen. Opnieuw hebben wij met een integraalvergelijking te maken, waarbij het totale veld wordt bepaald door de aanwezigheid van een object en dus een elektromagnetisch contrast in de ondergrond. Buiten het object is het totale veld gelijk aan de som van het invallend veld van het antennesysteem en het verstrooide veld als gevolg van het contrast. Door de Bornbenadering toe te passen, verwaarlozen wij verstrooiing van het veld binnen het object. Hierna gebruiken wij opnieuw reciprociteit om het antennesysteem als een tweepoort systeem te beschrijven, één voor de zender en één voor de ontvanger. Vervolgens nemen wij aan dat het elektrisch veld lineair afhankelijk is van de stroomdichtheid in een antenne. Dit resulteert in een integraalvergelijking, waarbij een bekende elektrische stroom en een sensitiviteitsfunctie convolueren met het onbekende contrast van een object met de ondergrond, en waarbij het contrast wordt waargenomen door een verandering van de potentiaal gemeten door de ontvanger. We laten zien dat de sensitiviteitsfunctie gelijk is aan het product van het elektrisch veld veroorzaakt door de zender en het veld indien de ontvanger aan het zenden is. De convolutie in de angulaire richting rondom de as van de antenne wordt berekend met behulp van de transformaties van Fourier.

Omdat de sensitiviteitsfunctie een belangrijke rol speelt, is het van belang om het gedrag van deze functie te onderzoeken. Daarvoor worden meerdere stralingspatronen berekend met variërende frequenties en radiale afstanden, in het vlak door het midden van, en opgespannen door de dipool. Door de stralingskarakteristieken te vergelijken, blijkt dat de complexe sensitiviteitsfunctie benaderd kan worden door een effectieve functionaal, waardoor geheugenruimte en rekentijd wordt bespaard. Tevens blijkt dat in het angulaire Fourier-domein slechts 9 van de 64 componenten een significante waarde hebben. Door de berekeningen alleen voor de 9 significante componenten uit te voeren wordt een verdere reductie van rekentijd en geheugenruimte verkregen.

Om van de gemeten data tot een drie-dimensionaal beeld te komen, moet een operator worden gevonden die werkt op de gemeten data. Om deze operator te verkrijgen wordt de norm van een functie gedefinieerd. Deze functie wordt verkregen door het verschil te nemen tussen het waargenomen veld en het berekende veld voor een gegeven contrast. Minimalisatie van deze norm leidt tot een expressie voor de gewenste operator. In de meest eenvoudige situatie bestaat deze operator uit twee delen. Het eerste deel geeft alleen een benadering van het contrast in de ondergrond. Het tweede deel schaalt dit resultaat, waarbij gebruik wordt gemaakt van het antwoord van het eerste deel. Doordat deze minimalisatie plaats vindt voor iedere component in het angulaire Fourier-domein, resulteert het tweede deel ook in een verbetering van de resolutie in de

angulaire richting. Beide algoritmes zijn getest op synthetische en gemeten data en leveren goede resultaten op. Daarnaast is ook een geconjugeerde gradiënten methode toegepast. Een iteratieve methode, waarbij het resultaat na iedere berekening wordt gebruikt om het contrast te verbeteren. Deze methode levert met name in de radiale en in de axiale richting een hogere resolutie op. Verder onderzoek naar de resolutie in de angulaire richting laat zien dat deze maximaal is. Het aantal significante componenten van de sensitiviteitsfunctie in het angulaire Fourier-domein, en daarmee het aantal componenten waarvoor het contrast wordt berekend, is hierbij de beperkende factor.

Geconcludeerd kan worden dat het is gelukt om een nieuw type radarsysteem te ontwikkelen dat een richtingsafhankelijke gevoeligheid bezit. Door de centrale frequentie rond de 100 MHz te kiezen heeft het systeem het juiste evenwicht gevonden tussen doordringend vermogen en resolutie. Het systeem is hierdoor in staat om objecten vanuit een boorgat goed, eenvoudig en snel op te sporen. Dit kan leiden tot een aanzienlijke kostenbesparing bij bijvoorbeeld de opsporing van blindgangers of de bouw van tunnels.

Curriculum Vitae

Koen Willem Anton van Dongen was born at March 25, 1971, in Ilo-ilo, Philippines. After three months he moved to the Netherlands. From 1973 to 1990, he lived in Reeuwijk. At the Sint Antonius College in Gouda he received in 1989 his HAVO-diploma and in 1990 his VWO-diploma.

His study started in 1990 at the poly-technical school in Eindhoven, where he received his first year degree in 1991. Next, he moved to Utrecht to study physics and astronomy at the university. After receiving his first year degrees in physics and astronomy in 1992, he specialized in experimental physics. During his study he went several times abroad, amongst others for a period of three months to CERN (European Organization for Nuclear Research) in Geneva, Switzerland, where he performed computations on the mass of the W-boson. His masters thesis was written at the Department of Sub Atomic Physics, where he cooperated in the design of a cooling system for a silicon track system by doing thermal experiments. The track system was part of a setup to observe "Charge/Parity"-violation at DESY (Deutsches Elektronen-Synchrotron) in Hamburg, Germany.

From 1998 to 2002 he was affiliated with T&A Survey, a geophysical survey company in Amsterdam, the Netherlands. In these four years he developed the radar system described in this thesis. His research resulted in various publications, presentations, a patent and this thesis. In addition, the complete system obtained the Wall Street Journal Europe "Innovation Award" .

Currently, he works as a postdoctoral researcher at the Laboratory of Electromagnetic Research at Delft University of Technology in a project on the location of buried landmines, financed by STW (Stichting voor de Technische Wetenschappen).

